Spatio-temporal modelling of fMRI data

Thordis Linda Thorarinsdottir
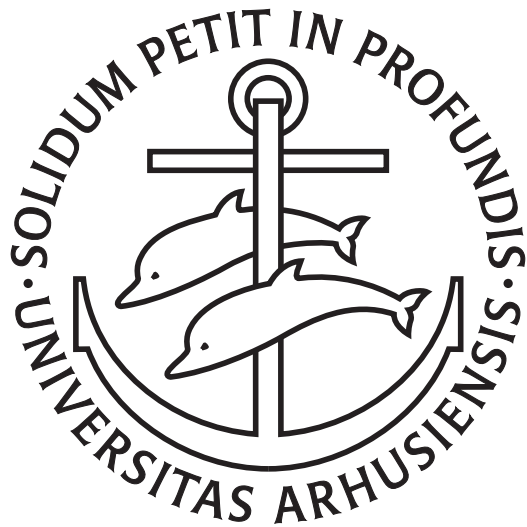
PhD Thesis

Department of Mathematical Sciences
University of Aarhus

August 2006

Preface

The functioning of the human brain is a mystery that has intrigued scientists for centuries. Research within the field has exploded in the last decades with the development of techniques such as functional magnetic resonance imaging which enable non-invasive *in vivo* recording of brain activation. This PhD thesis is a contribution to the research of the functioning of the human brain with focus on the modelling techniques for the mapping of brain functions.

The thesis consists of a review together with four independently written papers and is submitted to the Faculty of Science, University of Aarhus. The review provides an introduction to the field of functional magnetic resonance imaging with emphasis on the mapping of brain functions. The results of the accompanying papers are introduced and connections to related work within the field are discussed. The core of the thesis is the enclosed papers which present new approaches to the modelling of brain activation and an investigation of the clinical potential of brain mapping.

Finally, I would like to extend my deepest gratitude to my family and friends for their support and encouragement. I am especially indebted to Kristjana Ýr Jónsdottir to whom I thank the idea of coming here to Århus. I also wish to thank her for here valuable feedbacks and moral support throughout the studies.

Århus, August 11, 2006.   Þórdís Linda Þórarinsdóttir

Summary

The functioning of the human brain has fascinated scientists for centuries. It is though only in the last decades that systematic investigation of the phenomena has been made possible with the development of techniques which enable non-invasive *in vivo* recording of brain activation. One of these techniques is functional magnetic resonance imaging (fMRI). With fMRI, time series of images showing the changing blood flow in the brain associated with neural activation are acquired.

The analysis of images of this kind has allowed scientists to map a wide variety of brain functions to specific locations in the brain and to investigate the functional connectivity of different brain areas. The objectives of such experiments range from simple motor, visual, or cognitive tasks such as moving the fingers or watching a blinking light to more complex phenomena such as maternal and romantic love (Bartels and Zeki, 2004). The data is, however, a realisation of a complex spatio-temporal process with many sources of variation, both biological and technical. In order to model the activation of interest, it is therefore usually necessary to use highly controlled set of stimuli where the stimuli is repeated several times with resting periods in between. The aim of the analysis is then to find those areas of the brain showing increased or decreased activation during the epochs of stimuli.

One experiment of this type is presented in the thesis. Here, the aim is to investigate the brain activation during repetitive pelvic floor muscle contraction in women. We compare the brain activation in healthy women and in women suffering from stress urinary incontinence before and after physical therapy treatment.

With the success of experiments of this type, there is a growing interest within the neuroscience community to extend the experimental paradigm to more complex and more natural stimuli. Examples of the questions asked here are what happens in the brain during rest, meditation, or the viewing of a motion picture? Data of this type is to date usually analysed using simple correlation analysis or data driven methods such as independent component analysis. This type of analysis will though not reveal the more complicated interaction structure of the activation. For instance, a particular region of the

brain may only be active if a collection of other regions are active. It may also be of interest to investigate whether the duration and extend of activation may depend on the particular region of the brain studied. Activation structure of this type may be investigated using the spatio-temporal point process modelling approach introduced in this thesis. Here, the activation is modelled as a marked spatio-temporal point process where for each point, the location in space defines the centre of the given activation, the location in time defines the starting time of the activation, and the mark describes the duration and spatial extension. Modelling framework of this type allows for simultaneous uncertainty about both the time points and locations of activation and permits great flexibility in both the experimental design and the type of inference questions asked.

Further work presented here is a Bayesian procedure for removing noise from images that can be viewed as noisy realisations of random sets in the plane. This procedure is based on recent advances in configuration theory and assumptions on the mean normal measure of the set are used to obtain prior probabilities of observing the different boundary configurations. Within fMRI data analysis, mixture models of similar type are used to model the spatial pattern of the brain activation once temporal modelling has been used to model the activation in each voxel independently.

The thesis consists of a review and four independently written papers. One paper has already been published and further two have been accepted for publication. The co-authors of the papers are my supervisors Eva B. Vedel Jensen from the Department of Mathematical Sciences, University of Aarhus and Hans Stødkilde-Jørgensen from the MR Research Centre, University of Aarhus.

Contents

Accompanying papers

A Eva B. Vedel Jensen and Thordis L. Thorarinsdottir (2006):
Spatio-temporal model for fMRI data
- with a view to resting state networks.
To appear in *Scandinavian Journal of Statistics*.

B Thordis L. Thorarinsdottir and Eva B. Vedel Jensen (2006):
Modelling resting state networks in the human brain.
Proceedings S^4G: International Conference on Stereology, Spatial Statistics and Stochastic Geometry. R. Lechnerová, I. Saxl, and V. Beneš editors.

C Thordis L. Thorarinsdottir (2006):
Bayesian image restoration, using configurations.
To appear in *Image Analysis & Stereology*.

D Thordis L. Thorarinsdottir and Hans Stødkilde-Jørgensen (2006):
Functional imaging of pelvic floor muscle control.
To appear as Thiele Research Report, Department of Mathematical Sciences, University of Aarhus.

1. Introduction

The technology that allows us to investigate the functioning of the active human brain has developed immensely in the last decades. One of the most popular brain imaging method is functional magnetic resonance imaging (fMRI) which is based on the different magnetic properties of oxygenated and deoxygenated haemoglobin. With the method, images of the changing blood flow in the brain associated with neural activation are acquired. FMRI based on this blood oxygenation level dependent (BOLD) effect has, since first reported by Ogawa *et al.* (1990), been widely adopted by the neuroscience research community for basic studies of brain function. The main advantages of fMRI over other brain imaging methods are its non-invasive nature without involving exposure to ionising radiation, as well as its good spatial resolution of about two to three millimetres. The method has, however, a rather poor temporal resolution of a few seconds. This is though mainly because of the poor temporal resolution of the BOLD effect, not because of the MR technique itself.

The data obtained with fMRI are a realisation of a complex spatio-temporal process with many sources of variation, both biological and technical. Careful mathematical modelling is needed to extract the components related to neural activation of interest from the remaining variation in the data. In order to achieve this, most conventional experiments use a controlled and highly constrained set of stimuli specifically designed to activate only a specific subset of regions at predefined times (Bartels and Zeki, 2005). With the success of experiments of this kind, there has been a growing interest in recent years to investigate the functioning of the brain under more natural conditions, such as during rest (Biswal *et al.*, 1995; De Luca *et al.*, 2006; Fox *et al.*, 2005) or during free viewing of a motion picture (Bartels and Zeki, 2005; Hasson *et al.*, 2004). During such experiments, a complicated network of brain areas is activated and there is uncertainty about both the position and the timing of activation. Most conventional modelling methods have difficulties extracting the activation components of interest from data acquired under such an unconstrained experimental setup. The main contribution of this thesis is a new and more flexible modelling approach based on spatio-temporal point process theory that allows for simultaneous uncertainty in the position and the timing

of brain activation. This modelling approach is presented in Paper A and Paper B.

FMRI has had a huge impact on the understanding of the healthy human brain. It has, however, had much less impact in clinical neuroscience or clinical practise. The clinical potential of brain mapping using MRI is the subject of this years special issue of the Journal of Magnetic Resonance Imaging, see Jezzard and Buxton (2006). The editors of this special issue conclude that one of the challenges here is the lack of well-controlled trials that test fMRI against other more accepted diagnostic and therapeutic measures. Paper C presents an on-going work where this is investigated for stress urinary incontinence in women. Here, we compare the brain activation during pelvic floor exercises in healthy women, incontinent women before physical therapy treatment, and incontinent women after treatment. Further analysis is planned, where the functional imaging data will be compared to MR images of the pelvic floor muscle during relaxation and straining for the same subjects.

In Paper D, we present a Bayesian procedure for removing noise from binary images that can be viewed as noisy realisations of random sets in the plane. The inspiration for this work comes from spatial mixture modelling of fMRI data, more precisely a paper by Hartvig and Jensen (2000). In conventional analysis of fMRI data, the temporal part of the analysis is often performed independently for each voxel. This gives a test statistic for the activation in each voxel. In Hartvig and Jensen (2000), the posterior probability for a voxel being activated is calculated based on a test statistic depending on a small neighbourhood around the voxel. Here, the posterior probability depends on the number of activated voxels in the neighbourhood. We have extended this method, using configuration theory, to take into account the spatial pattern of the activations within the neighbourhood. This seems appropriate if the resolution of the true image is good enough so that the patches of activations are larger than the neighbourhood used for the restoration procedure. Further, we have chosen to present the method in the more general framework of random sets in the plane.

This review is organised as follows. In Chapter 2, we discuss the challenges of modelling neural activation in the brain using fMRI data both due to the quality of the data and the nature of the experiments performed. A review of some of the most common existing methods for fMRI data analysis is given in Chapter 3. Further, the statistical methods used for the analysis in Paper C are discussed in more detail than in the paper. An introduction to the theory of spatio-temporal point processes and to the modelling framework described in Paper A and Paper B is given in Chapter 4. Future work and further extensions of the model are also discussed. Finally, Chapter 5 gives an introduction to the work presented in Paper D.

2. FMRI data and the human brain

During a functional MR scan, the scanner records a time series of an image of an axial slice through the brain of thickness 3-8 mm. The image consists of 64×64 or 128×128 voxels (volume elements) with in-plane resolution 1.5-4 mm. In most studies, a collection of equi-distant slices is combined to form a pseudo 3D image of the brain. The disposition of the slices and the coordinate system used is explained in Figure 2.1. During a whole brain scan, such a volume of images may be obtained within two or three seconds, while only about one hundred milliseconds are needed for a single slice. There is, however, a trade-off between spatial and temporal resolution; images with large voxels can be acquired more quickly than images with small voxels.

Figure 2.1: Scout MR images used to place the slices for the functional scan. Axial section (left), saggital section (middle), and coronal section (right) through approximately the centre of the brain. In xyz-coordinates, the xy-plane is parallel to the ground, the x-axis going front and back, the y-axis passing left and right, and the z-axis going up and down. Note that the orientation of the axial section is radiological, the subject's right is on the left side of the image as if the subject were standing in front of and facing the observer. The images acquired during functional scans are usually axial sections through the whole brain taken at an angle of $100° - 110°$ to the z-axis in order to minimise the number of slices needed to cover the whole brain.

In Paper C we analyse images consisting of 64×64 voxels of size $3.75 \times 3.75 \times 3$ mm with 1 mm gap between the slices, so that approximately 30 slices are needed to cover the whole brain. It takes the scanner three seconds

to obtain one pseudo 3D image and the whole scan lasts three minutes. We have thus roughly 120 thousand voxels in the dataset and for each voxel, we have information from 60 time points. The number of voxels can, however, be reduced somewhat as voxels located outside the brain may be discarded. We are interested in making inference about the populations from which our subjects are drawn and have thus repeated the experiment for several subjects from each population. One of the obstacles facing every analysis approach is hence the excessive amount of data, whereof only a very small part contains effects of interest.

For readers unfamiliar with the anatomy of the human brain, some of the main regions of the brain discussed in the following are outlined in Figure 2.2. For a more detailed information we refer to the classical book *Anatomy of the Human Body*, the 1918 edition of which is available on-line at http://www.bartleby.com/107 (Gray, 1918).
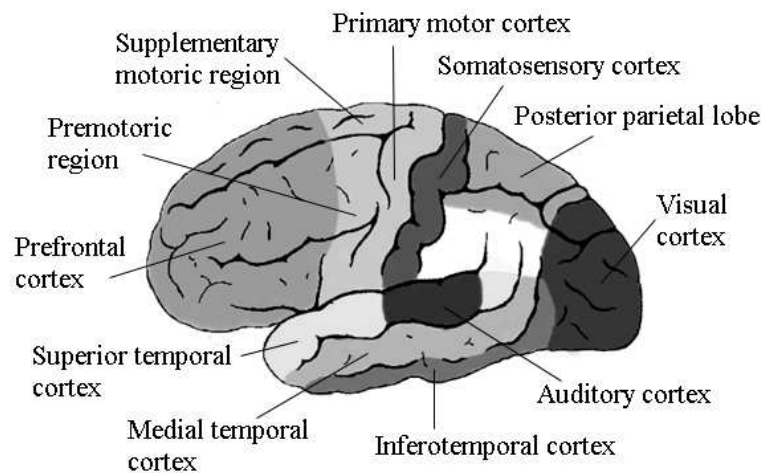
Figure 2.2: Regions of the brain: lateral surface of left hemisphere, viewed from the side. Modified from Gray (1918).

As this thesis focuses on the modelling aspect of fMRI data and the mapping of brain function, we will not discuss the MRI technique and how the signal is retrieved. For this, we refer the reader to Haacke *et al.* (1999). Further, we will not address details of the underlying biological processes and the brain metabolism. However closely related to the interpretation of the data and thus important in this context, these very complicated processes are better left to the experts of neuroscience to discuss, see e.g. Raichle and Mintun (2006) and references therein.

2.1   The haemodynamic response

The MRI signal changes in activated regions of the brain, the BOLD effect, results from changes in oxygenation, blood volume and flow. This effect, also called the haemodynamic response, changes the MRI signal as follows: approximately 2 seconds after neural activity begins, the signal begins to increase and plateaus after about 6 to 10 seconds, remaining elevated while the activity continues. The signal then returns to baseline about 8 to 11 seconds after activity ends. Transient signal changes have also been described, including a decrease below baseline within the first two seconds of activation and the more commonly reported decrease below baseline for 10 to 40 seconds after activity ends (Bandettini and Ungerleider, 2001). Examples of simple models for the haemodynamic response are shown in Figure 2.3, see Paper A for more details. There are though a few disadvantages of using the haemodynamic response as a measure for neural brain activation. One difficulty is that the dynamics, location, and magnitude of the signal can be influenced by the vasculature in each voxel. If a voxel happens to capture large vessel effects, the magnitude of the signal may be larger than usual, the timing a bit more delayed than on average, and the location of the signal up to a centimetre away from the true origin of activation (Bandettini *et al.*, 2005).
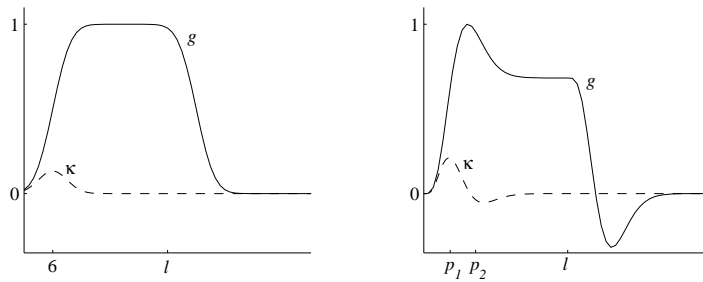
Figure 2.3: Examples of models for the haemodynamic response function. The response starts at time zero and the duration of activation is l time units. Left: Gaussian response function κ (dashed) and the corresponding integrated response function g (solid). Right: Gamma response function κ (dashed) and the corresponding integrated response function g (solid). The parameters p_1 and p_2 must be estimated from data. See Paper A for more details.

The precise connection between the haemodynamic response and the underlying neural activity is also not satisfactorily known. In a first approximation, the haemodynamic responses and neural responses have been shown to have a linear relationship for stimulus presentations of short duration (Logothesis, 2003), but the question remains whether it is the input to neurons

5

as reflected in the local field potentials that primarily drives the changes in the MRI signal or whether it is the output of neurons as manifested by their spiking activity (Raichle and Mintun, 2006). See Logothetis *et al.* (2001) and Logothetis and Wandell (2004) for reports supporting the former theory and Mukame *et al.* (2005) for a report supporting the latter. It would therefore be desirable to possess a technique which could directly detect the neural activity with MR imaging. For a recent review of the work that been performed in this direction, see Bandettini *et al.* (2005).

Another possibility is to combine the MRI technique with an imaging technique that has a much better temporal resolution than fMRI but lacks the good spatial resolution. Possible candidates here are magnetoencephalography (MEG) and electroencephalography (EEG). MEG measures the magnetic field produced by electrical activity in the brain using a few hundred extremely sensitive devices that are situated around the head. EEG, on the other hand, measures the electrical activity in the brain by recording from electrodes situated on the scalp. For a discussion of the different methods used for data comparison, see Horwitz and Poeppel (2002). The pioneering study of Ives *et al.* (1993) showed that it is possible to record EEG signals within the MR scanner and this method has gained popularity even though the time varying magnetic field during the fMRI scanning completely obscures the EEG signal. See e.g. Wan *et al.* (2006) and references therein for methods to remove the MR related artifacts from the EEG signal.

In our work, we have concentrated on the modelling of fMRI data acquired using the BOLD effect even though the method is not flawless. As of today, there is no alternative method that outperforms it in both spatial and temporal resolution and improvements are being made in the methodology to reduce the vasculature related variation. Further, a combination of different methods still requires careful modelling of each method separately.

2.2   Resting state activation

The unprocessed MRI signal is quite noisy. Some of the noise is created by such uninteresting, yet troublesome, sources as scanner electronics, subject movement, respiration, and variations in systematic cardiovascular dynamics (Raichle and Mintun, 2006). See also Triantafyllou *et al.* (2005) for a detailed investigation of the noise for different magnetic field strengths. There is, however, a considerable fraction of the low frequency variation that appears to reflect fluctuating neural activation. Biswal *et al.* (1995) were the first to notice that these spontaneous fluctuations in the signal in one area of the motor cortex were correlated with the fluctuations in other areas within the motor cortex. Their initial observation has since been replicated and extended

to reports of several distinct resting state networks, including visual, auditory, and language processing networks, see Greicius *et al.* (2003), Beckmann *et al.* (2005), De Luca *et al.* (2006), and Fox *et al.* (2005). The networks have been reported to show increased activation during rest (De Luca *et al.*, 2006), as well as decreased activation during attention demanding cognitive tasks (Fox *et al.*, 2005). These findings are, so far, mainly of theoretical interest to enhance our understanding of the functioning of the human brain. There are though reports indicating that resting activation can be used for clinical purposes such as to distinguish Alzheimer's disease in its early stages from healthy ageing, see Greicius *et al.* (2004).

An example of such resting data, earlier analysed in Beckmann *et al.* (2005), is shown in Figure 2.4. The dataset consists of a time series of a single axial slice chosen to intersect the sensory motor cortices bilaterally. In Figure 2.4, the MR signal intensity is shown at 12 equidistant time points during the scan. Even though the subject is not imposed to stimuli, changes in the MR signal over time appear, some of which show covariation in different regions of the brain. This will be made more clear in the following, where we show some analysis results for this dataset, see also Paper A and Paper B where the dataset is analysed using the spatio-temporal point process model introduced in Chapter 4. Note that the images shown here have been preprocessed in order to correct for movement related artifacts and to enhance the signal changes so that they can be observed with the naked eye.
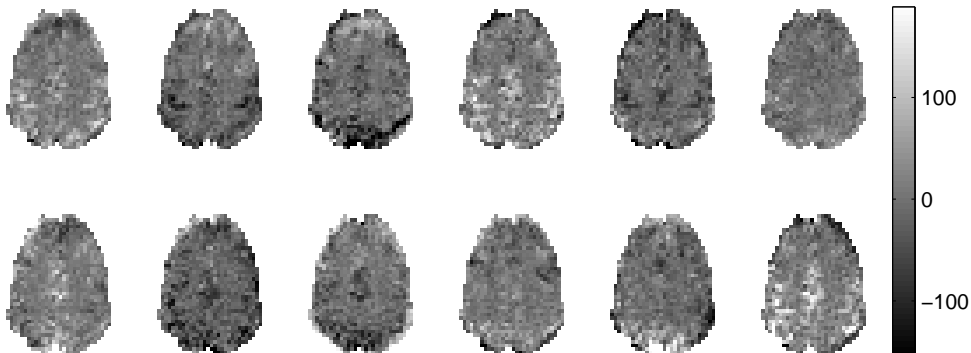
Figure 2.4: Development of the MR signal activity over time in a single slice through the human brain. From left to right and top to bottom: the activity at time $t = 12, 30, 48, \ldots, 210$ seconds.

Estimating the temporal and the spatial characteristics of these low frequency fluctuations in the MR signal represents a formidable challenge to analytical techniques. In most existing studies of the phenomena, the resting state networks are inferred by either simple correlation analysis or the data driven

method of independent component analysis (ICA). For a detailed discussion of the methods, see Section 3.3. In the correlation analysis, the voxel-wise time series are usually correlated against a reference time course from secondary recording such as EEG, or the time series from a seed voxel which is believed to be of functional relevance. Here, a very specific hypothesis about the temporal structure of the activation is tested and a more flexible model would be advantageous. The spatio-temporal point process model presented in Paper A and Paper B is a candidate for such a modelling framework, as it allows for uncertainty about both the time points and locations of activation.

When analysing resting state activations, it is necessary to impose some constrains in order to be able to distinguish between the actual resting state activations and other sources of variation such as respiration related activation which is fundamentally quite similar. It is, however, not quite clear how to define useful and unambiguous constrains that will not eliminate any activation of interest. In this connection, it would be of interest to investigate datasets where the subjects are imposed to natural stimuli involving several distinct networks of brain activation. An example of this are experiments where the subjects watch a movie sequence during the scan (Bartels and Zeki, 2005; Hasson *et al.*, 2004). An fMRI experiment will always be an approximation to a natural condition given the constraints of the experimental setup, but film viewing should provide natural conditions at least for the visual and auditory system. The authors use well known movies (Bartels and Zeki (2005) have chosen the James Bond movie *Tomorrow Never Dies*, while Hasson *et al.* (2004) preferred the cowboy film *The Good, the Bad, and the Ugly*) that are complicated enough in nature so that specific hypotheses about the timing and location of brain activation cannot be posed. It would thus be of interest to put this type of experiments within a modelling framework where the movie, though very complicated in character, could act as the natural constraint that is missing when analysing resting state data.

3. A review of fMRI data analysis

Every year, hundreds of papers covering research on functional magnetic resonance imaging are published (Jezzard and Buxton, 2006). It is thus impossible to give a comprehensive review of the methods used to analyse fMRI data within the scope of this overview. Instead, we will focus on the most popular methods, those used to analyse resting state data, and models that are related to our own work or have been inspirational for us. For a comparison of some of the different methods used to analyse fMRI data, see e.g. Poline *et al.* (2006) where results from the Functional Imaging Analysis Contest held in connection with the 11th Annual Meeting of the Organisation for Human Brain Mapping in Toronto in 2005 are summarised.

As mentioned above, the data from an fMRI experiment constitute a collection of time series

$$Z_{tx}, \quad t = t_1, \ldots, t_m,$$

$x \in \mathcal{X}$. Here, Z_{tx} is the MR signal intensity at time t and voxel x. The time points $t_1, \ldots, t_m$ are usually equidistant and belong to the interval $[0, T]$, where T is the length of the experiment. The set $\mathcal{X}$ is a finite subset of $\mathbb{R}^2$ or $\mathbb{R}^3$ with N elements, or voxels, representing a two dimensional slice or a three dimensional volume of the brain.

Before the data is analysed for activation of interest, it is preprocessed in a variety of ways in order to facilitate or improve the subsequent analysis. It is, for instance, essential to correct for head movement during the scan as one wants to assume that a given anatomical location is represented by the same voxel of every image of the time series, see Oakes *et al.* (2005). When comparing activation across subjects, the data is usually mapped onto a template that already conforms to some standard anatomical space such as Talairach and Tournoux (1988) and an inhomogeneity correction is performed, see e.g. Frackowiak *et al.* (2003, Ch. 33-34) and Jenkinson (2003). Furthermore, the data is often subjected to spatial and/or temporal smoothing with Gaussian kernels, see Friston *et al.* (1995) and Friston *et al.* (2000). The main effect of smoothing is that it increases the signal to noise ratio and decreases inter-subject inhomogeneity. Other preprocessing such as artifact detection and

removal is often included in the modelling phase and will be discussed further in the following.

3.1   Conventional modelling

Here, we consider the problem of finding the brain activations during a controlled set of stimuli where the timing of the activation is known. The most widely used strategy for this type of analysis is to use a two-stage approach. In the first stage, the temporal activation is modelled using a linear model for each voxel independently. The second stage then focuses on identifying those areas of the brain that were activated by the stimuli based on the results from the first stage.

Temporal modelling

Most models used to model the temporal activation profile are regression models of the type

$$Z_{tx} = Y_t \alpha_x + W_t \beta_x + \varepsilon_{tx}, \tag{3.1}$$

where the columns of Y_t model effects of interest, the columns of W_t model effects of no interest that are considered confounds, such as temporal drift, and ε_{tx} denotes the noise.

The general linear model implemented in the SPM5 program (for more information about the program, see http://www.fil.ion.ucl.ac.uk/spm/) is by far the most popular model used in fMRI data analysis. There are two main reasons for its popularity. Its user-friendly graphical interface allows the user to perform all the processing steps needed to go from the raw scanner data to the colourful activation images without much need for statistical expertise. The authors of the program are also very effective in correcting errors and adding extensions. In addition, the method performs quite well on the problem it is intended to solve: to find the brain activations during a controlled set of stimuli where the timing of the activation is known. We have used this program for the data analysis in Paper C, where the data is of this type.

Several different ways of defining and estimating models of the type (3.1) are implemented in SPM5. In Paper C, we have chosen the following classical inference method: the effects of interest, the haemodynamic response, is modelled using the canonical haemodynamic response function shown in Figure 3.1. Here, the user can choose whether to include the time derivative which allows the peak response to vary by plus minus a second and the dispersion derivative which allows the width of the response to vary by a similar amount. Other models for the response include Gamma functions and Fourier basis sets, see Frackowiak *et al.* (2003, Ch. 40). The matrix Y_t also includes

a constant column which models the baseline. The drift is modelled using a
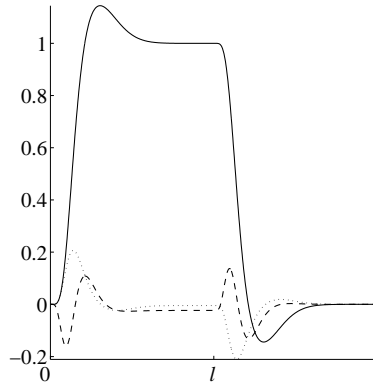
Figure 3.1: The canonical haemodynamic response function model used in SPM5 (solid), together with its time derivative (dotted) and dispersion derivative (dashed). The activation shown starts at time 0 and its duration is l time units.

high-pass filter which is implemented by a discrete cosine transform set with harmonic periods up to a cutoff set by the user. Finally, the noise is modelled using an AR(1)+white noise model

$$\varepsilon_{tx} = \tau_{tx} + \eta_{tx},$$

where

$$\tau_{tx} = \exp(-1)\tau_{t,x-1} + \omega_{tx},$$

$\eta_{tx} \sim N(0, \sigma_{1x}^2)$, and $\omega_{tx} \sim N(0, \sigma_{2x}^2)$. The additional white noise component η_{tx} contributes to the zero-lag autocorrelation, which in turn allows the AR(1) model to capture better the shape of the autocorrelation for longer lags.

The parameters of the model, α_x, β_x, σ_{1x}, and σ_{2x}, are estimated using an iterative restricted maximum likelihood algorithm, see Frackowiak *et al.* (2003, Ch. 39 and 47). In order to increase the speed of the algorithm, the assumption is made that the ratio of σ_{1x} and σ_{2x} is stationary over voxels.

Bayesian methods for the temporal modelling have also become popular in recent years. In Genovese (2000), the author presented a fully Bayesian approach for the temporal modelling of the activation. At the time, this was a fundamentally new approach. The model is given by

$$Z_{tx} = \mu_x(1 + a_t(\gamma_x, \theta_x)) + d_{tx} + \varepsilon_{tx}, \qquad \varepsilon_{tx} \sim N(0, \sigma_x^2),$$

where μ_x is the baseline mean, a_t is the activation profile, and d_{tx} denotes the drift term. The parameter $\gamma_x = (\gamma_{x1}, \ldots, \gamma_{xK})$ specifies the amplitude of the

signal change associated with each of K different stimulation conditions and θ_x is an 8-dimensional parameter describing the shape of the haemodynamic response. More precisely, the activation profile a_t is given by

$$a_t(\gamma, \theta) = \sum_i \gamma_{k_i} b(t - t_i; \theta),$$

where t_i is the starting time and k_i is the type of the stimuli of the i'th stimulation epoch. The function $b(t; \theta)$ describes the haemodynamic response of a single stimulation epoch. It is constructed from cubic splines and its shape follows the description of the haemodynamic response in Section 2.1. The drift term is also modelled by cubic splines, but constrained to be smooth.

As the author uses a fully Bayesian approach, he defines prior distributions for all parameters. The model is over parameterised which is compensated for by including prior information from previous fMRI studies, see Genovese (2000) for details. In the inference, sub models obtained by assuming that only subsets of $\{\gamma_{xk}\}$ are different from zero are considered. The posterior probabilities of the different sub models are estimated using either posterior maximisation or MCMC sampling. Note that unlike many other models, the activation is here defined as a fraction of the baseline level. An alternative to this is to assume an additive model for log-transformed data, as in Hartvig (2002).

Spatial modelling

Once the parameters of the temporal model in (3.1) have been estimated, statistics, typically t or F statistics, are calculated that reflect the components of the response under study. For example, we might calculate the t statistic under the null hypothesis $H_0 : \alpha_x^i = 0$ with alternative hypothesis $H_1 : \alpha_x^i > 0$ for all $x \in \mathcal{X}$, where i is the column of Y_t containing the canonical haemodynamic response function. The values of the statistic can then be plotted spatially as a statistics image. In the fMRI literature, this image is called a statistical parametric map (hence the name of the program SPM5). An example of such an image is shown in Figure 3.2. The aim of the spatial modelling is then to analyse images of this type to reveal the areas of the brain activated by the stimuli in question.

One popular method for the spatial modelling is based on thresholding at a single level. The aim is to choose a significant level for each test such that the family wise error rate, the probability of making one or more type I errors among all the hypotheses, is controlled at some prespecified level. This induces a multiple comparison problem that is further complicated by the correlations that exists between the tests due to the spatial arrangement of the voxels (Marchini and Presanis, 2004). In Worsley *et al.* (1992), the authors model the
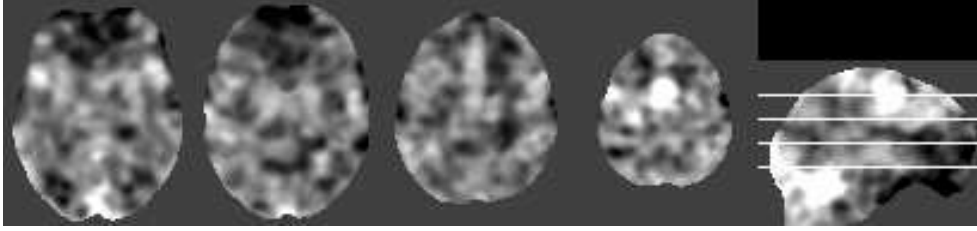
Figure 3.2: An example of a statistical parametric map used in the analysis in Paper C. The location of the four axial slices is shown on the saggital view (right).

statistics image as a good lattice representation of an underlying d-dimensional random field $G(r), r \in \Omega \subseteq \mathbb{R}^d$, for a compact set Ω and $d \in \{2,3\}$. The random field G is assumed to be strictly stationary, continuous, and smooth. The probability that $G(r)$ exceeds a given threshold u is approximated by the expected value of the Euler characteristic χ_u of the field. If u is close to the maximum of random field $G_{\max}$ we get

$$\mathbb{P}(\text{reject } H_0 | H_0 \text{ true}) = \mathbb{P}(G_{\max} > u) \approx \mathbb{P}(\chi_u > 0) \approx \mathbb{E}(\chi_u)$$

and the family wise error rate can be controlled through knowledge of the expected Euler characteristic. It is usually assumed that the random field is Gaussian but results for t, F, and χ^2 fields have also been published, see Worsley (1994).

The assumption that the statistics map is a "good enough" lattice representation of an underlying Gaussian random field is questionable for single subject datasets with standard spatial resolution. This can be improved by spatially smoothing the data with Gaussian bell functions prior to the analysis, see Friston *et al.* (1995) and Worsley and Friston (1995). Spatial smoothing will, however, deteriorate the fine spatial resolution of the data and this way, the data is being fitted to the theory when surely it would be better to fit the theory to the data (Marchini and Presanis, 2004).

Another method to handle the multiple comparison problem is to control the false discovery rate, the expected proportion of false positives among those voxels declared positive. This method was developed by Benjamini and Hochberg (1995) and adopted to the analysis of fMRI data by Genovese *et al.* (2002). The procedure is extremely simple to implement: select a false discovery rate α between 0 and 1. Calculate the uncorrected p-value for each voxel and order them from smallest to largest, $p_1 \leq p_2 \leq \ldots \leq p_N$. Let r be the largest i for which

$$p_i \leq \frac{i}{N} \frac{\alpha}{c(N)},$$

where $c(N)$ is a predetermined constant defined as $c(N) = 1$ or $c(N) = \sum_i 1/i$. Finally, threshold the image of the test statistics at the value corresponding to the p-value p_r. The choice of the constant $c(N)$ depends on the assumptions about the joint distribution of the p-values across voxels. The choice $c(N) = \sum_i 1/i$ applies for any distribution, while $c(N) = 1$ holds when the p-values at the different voxels are independent and under a technical condition that holds when the noise in the data is Gaussian with nonnegative correlation across voxels.

An alternative Bayesian approach is based on using mixture models for levels of activation. This method is discussed in detail in Section 5.2 as it is closely related to the work in Paper D. A more detailed discussion of the different methods for the spatial modelling can be found in Marchini and Presanis (2004) where comparison analysis of the different methods is performed. Both methods described above are implemented in SPM5. We have chosen to use the family wise error rate for our analysis in Thorarinsdottir and Stødkilde-Jørgensen (2006). In the analysis of our data, this method gives a slightly more conservative results than the method based on false discovery rate. As we in general get a very high level of activation in the data, it seems appealing to choose the more conservative method.

3.2 Spatio-temporal models

When conventional analysis of fMRI data as described in the previous section is extended within a Bayesian framework, hierarchical Bayesian approaches can be used to simultaneously incorporate temporal and spatial dependencies between the pixels in the model formulation. Different aspects of classical and Bayesian inference in neuroimaging is discussed in Friston *et al.* (2002b) and Friston *et al.* (2002a). Spatio-temporal Bayesian extensions of models of the type (3.1) are introduced in e.g. Gössl *et al.* (2001) and Woolrich *et al.* (2004).

In Hartvig (2002), the author uses quite a different approach in that he formulates a spatio-temporal stochastic geometry model for fMRI data in a Bayesian framework. This model is closely related to the model introduced in Paper A and Paper B. The fundamental assumption is that space and time are separable, in the sense that the temporal activation profile is the same in each voxel, only the magnitude changes from voxel to voxel. For simplicity, we only describe a two-dimensional model for a single slice of data, see Hartvig (2002) for extensions to three dimensions. The spatial activation pattern is denoted by a marked point process $\Psi = \{[x_i; m_i]\}_{i=1}^n$, with $x_i \in \mathcal{X} \subseteq \mathbb{R}^2$ and $m_i = (a_j, d_j, r_j, \theta)$, where the marks describe respectively the magnitude, area, eccentricity, and angle of the activation centre located in voxel x_i.

The prior distribution of Ψ has density with respect to the unit rate Poisson

process of the form

$$p(\psi) \propto \prod_i \beta(x_i) \Big(\prod_{i<j} \gamma\big([x_i; m_i], [x_j; m_j]\big) \Big) \prod_j \big[p(a_j) p(d_j) p(r_j) \big].$$

Here, $\beta(\cdot)$ is an intensity function where prior knowledge about the location of activation can be incorporated, without such knowledge, $\beta(\cdot)$ is given a constant value. $\gamma(\cdot, \cdot)$ is a pairwise interaction function which discourages activation centres to fall on top of each other. The mark parameters a_i and d_i are given inverted Gamma priors, while the prior for r_i is a Beta distribution.

The magnitude of activation $\{A_x\}_{x \in \mathcal{X}}$ is assumed to be a sum of Gaussian functions

$$A_x(\Psi) = \sum_i h(x; [x_i; m_i]),$$

where

$$h(x; [x_i; m_i]) = a_i \exp\left(-\frac{\pi \log 2}{d_i} \left(\frac{(y^1)^2}{r_i/(1-r_i)} + \frac{(y^2)^2}{(1-r_i)/r_i} \right) \right)$$

and $y = (y^1, y^2) = R(-\theta_i)(x - x_i)$ and $R(\theta)$ is a rotation with angle θ. A linear trend is removed from each time series prior to the analysis so that it can be assumed that non-activated voxels have mean 0. The observed intensity Z_{tx} at voxel x and time t is modelled as

$$Z_{tx} = \big(A_x(\Psi) + \eta_x \big) \varphi_t + \varepsilon_{tx},$$

where $\{\varepsilon_{tx}\} \sim N_{|\mathcal{X}| \times n}(0, \sigma^2 \Gamma \otimes \Lambda)$ and $\eta_x \sim N_{|\mathcal{X}|}(0, \tau^2 I_{|\mathcal{X}|})$. Here, $|\cdot|$ denotes number and $\otimes$ denotes the Kronecker product. The haemodynamic response φ_t at time t is modelled with a general state space model

$$\varphi_t = \lambda_t + \nu_t,$$

where λ_t is a fixed convolution model for the haemodynamic response and $\{\nu_t\}$ is a random walk.

Inference in the model is centred on the posterior distribution of (Ψ, φ). An MCMC algorithm is used to simulate the point process Ψ given the data $\{Z_{tx}\}$ and the temporal response φ. The posterior distribution of φ given the data $\{Z_{tx}\}$ and the point process Ψ is a simple normal distribution which may be simulated directly using Kalman smoother recursion.

3.3   When the time course of activation is unknown

The models discussed in the previous sections can not be used directly when the time course of activation is unknown as is the case for e.g. resting state

data. Instead, authors use correlation analysis or data driven methods, among which independent component analysis (ICA) is the preferred method. Note that the methods described here can also be used to analyse conventional experiments where the time course of the stimuli is known.

Correlation analysis

In Fox *et al.* (2005), the functional connectivity in the resting brain is studied by a simple correlation analysis. A seed region $\mathcal{X}_0 \subset \mathcal{X}$ is selected and the correlation between the average time series for this region

$$\bar{Z}_{t\mathcal{X}_0} = \frac{1}{|\mathcal{X}_0|} \sum_{x \in \mathcal{X}_0} Z_{tx}, \quad t = t_1, \dots, t_m$$

and the time series of any other brain voxel is calculated in order to find regions $\mathcal{X}_1$ interacting with $\mathcal{X}_0$. Here, $|\cdot|$ indicates number. Similarly, in Greicius *et al.* (2003), the average time series is used as explanatory variable in a regression type of analysis of the time variation in other regions of the brain. Software packages such as SPM5 can be used for this kind of analysis. This analysis is attractive because it is simple. It does, however, require an a priori expectation of the network pattern and the detection of new, unknown networks is hardly likely.

Hasson *et al.* (2004) also use correlation analysis to retrieve their results on brain activation during free viewing of a motion picture. The analysis is done in two steps. In the first step, the authors search for inter-subject correlation by comparing the time course of a given voxel in a given subject to the time course of the same voxel in other subjects. In a second step of the analysis, a reverse-correlation approach is used to compare the movie sequence to the time course of voxels showing high inter-subject correlation. The advantage here is that the results from the first step of the analysis can be used to predict in which areas the MR signal fluctuation is related to the stimuli, as the fluctuations in these areas should be correlated between subjects. This can, on the other hand, not be expected for resting state data where the subjects are instructed to "let the mind drift and not think about anything specific or systematic".

Independent component analysis

ICA is an exploratory analysis, closely related to factor analysis and discriminant analysis. It is based on a model of the type

$$Z_{tx} = \mu_x + \sum_{k=1}^{K} A_{tk} B_{kx} + \sigma \varepsilon_{tx}. \tag{3.2}$$

Here, μ_x is the baseline signal at voxel x which can vary by a factor of 2-3 across the brain and the number K of components is unknown. The rows of the matrix $B = \{B_{kx}\}$ represent component maps and the columns of the matrix $A = \{A_{tk}\}$ represent time courses of the respective component maps. Furthermore, some independence assumptions are made regarding the components. In spatial ICA it is assumed that the rows of B are statistically independent process, whereas in temporal ICA the columns of A are assumed independent. Spatial ICA is usually used for fMRI data analysis. A general introduction to ICA is Hyvärinen and Oja (2000), while a good introduction to ICA for fMRI analysis can be found in McKeown *et al.* (2003). This paper also contains a comprehensive list of references with specific guidance to the literature.

An ICA analysis results in estimates of temporal activation profiles $\{A_{\star k}\}$ and spatial activation profiles $\{B_{k\star}\}$ for each k, where the estimated number K of components may be quite large, or usually about 30 for a whole brain analysis. The estimated temporal profiles are shown together with their associated power spectra. Only frequency components of a certain bandwidth are regarded as having neuronal origin. High frequency components may be caused by cardiac or respiratory activities, while very low frequency components are considered to be drift. Software packages performing ICA are available, e.g. the program FSL (available at http://www.fmrib.ox.ac.uk/fsl/) presented in Smith *et al.* (2004). An example of such estimated components are shown in Figure 3.3, where we have performed ICA on the data from Figure 2.4 using FSL. The dataset consists of a time series of images of an axial slice through the sensory motor cortex. The time series has 2000 time points with 120 ms between the images, the scan thus lasted 240 seconds. In Figure 3.3, we only show the first 25 seconds of the temporal activation profiles so that the pattern of the activation can clearly be seen.

It should be noted, however, that if spatial ICA is used to detect functionally connected networks of regions, as is the case for resting state data, it should be complemented by alternative methods such as correlation analysis, especially if the noise model is not accurate enough. This is because the spatial ICA applies the independence criterion only to the spatial activation profiles, which does not exclude the possibility that voxels of different spatial activation profiles might be temporally correlated, even though at a reduced level. An example of this is when both left and right hemisphere are activated simultaneously, but with slightly different temporal responses. This could cause the method to cluster the response into two different spatial maps, see Bartels and Zeki (2005) and Beckmann and Smith (2004).

The original version of ICA had several shortcomings. The assumption of complete independence in time or space is physiologically not very plausible, the unknown number of sources underlying the original signal causes difficul-
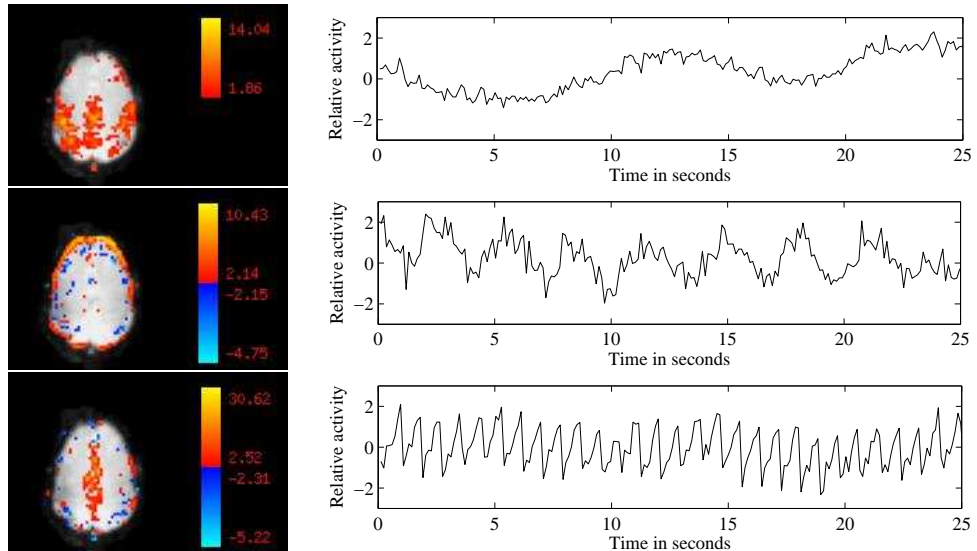
Figure 3.3: Independent component analysis of the data from Figure 2.4 using FSL. Three spatial activation profiles are shown together with the corresponding temporal profile for the first 25 seconds of the scan. Top: Low frequency activation component with significant activation in the motor cortex, middle: physiological artifact component induced by the respiratory circle, and bottom: physiological artifact component induced by the cardiac cycle.

ties, and in its original version, Equation 3.2 had no noise term. Furthermore, the methods do not provide statistical measure for inference at a single-subject or group level (Bartels and Zeki, 2005). Several groups have since improved different aspects of the method. One special variant is called probabilistic independent component analysis (PICA), cf. Beckmann and Smith (2004), which is the method behind the FSL program. Here, the noise in (3.2) is assumed to be Gaussian and in order to avoid over-fitting, estimation of the true dimensionality of the data, i.e., the number of activation and non-Gaussian noise sources is inferred from the covariance matrix with Bayesian methods. Further, mixture models are used to infer on the individual spatial activation profiles $\{B_{k\star}\}$ once they have been transformed into Z-statistic maps. The use of mixture models for inference is motivated by the work of Hartvig and Jensen (2000) which is discussed in Chapter 5.

In Beckmann and Smith (2005), the authors extended their method to allow for analysis of group data. The extended version is called Tensor PICA and is derived from parallel factor analysis. Equation 3.2 now becomes

$$Z_{tx}^i = \mu_x + \sum_{k=1}^{K} C_{ik} A_{tk} B_{kx} + \sigma \varepsilon_{tx},$$

18

where $i = 1, \ldots, I$ is an index over subjects or sessions. The activation profiles are essentially estimated in a similar way as for PICA, where the block structure of the data is used to separate the temporal profiles $\{A_{\star k}\}$ and the session/subject specific profiles $\{C_{\star k}\}$.

There were some early critiques of ICA, see Friston (1998), but it seems now to be generally recognised in the neuroscience community that ICA is a powerful nonparametric tool for analysing data in cases with uncertainty about the position and timing of activation. A number of interesting findings relating to specific resting state networks have been reported using ICA, see Beckmann *et al.* (2005); Greicius and Menon (2004); Greicius *et al.* (2004)). Further, in Bartels and Zeki (2005), the two authors review their approach to map the human cerebral cortex into distinct subdivisions using both traditional visual stimuli and a James Bond movie. They used ICA to identify voxels belonging to distinct functional subdivisions based on their temporal activation profile.

Recently, there has been some criticism of ICA because the results from the analysis refer to a "product brain". A particular type of activity in the brain is decomposed into a spatial activation map showing regions of the brain activated during the experiment and a temporal activation graph showing when the brain is activated during the experiment. Instead of this product decomposition, a more dynamic type of analysis is asked for in order to be able to reveal more complicated interaction phenomenon. For instance, a particular region of the brain may only be active if a collection of other regions are active. An example of this is the visual system which seems to have a very strong hierarchical structure, see Hochstein and Ahissar (2002). It may also be of interest to investigate whether the duration and extend of activation may depend on the particular region of the brain studied. As discussed in the next chapter, this criticism can be met by using a spatio-temporal point process modelling approach.

4. Spatio-temporal point process modelling

A spatio-temporal point process is a random collection of points where each point represents the time and the location of an event. Examples of such events include incidence of disease, sightings or births of species, or the occurrences of fires, earthquakes, tsunamis, or volcanic eruptions (Schoenberg *et al.*, 2002). The points of a point process are generally assumed to be indistinguishable besides their different times and locations. There is though often additional information available to be stored with the information on time and location. The dataset could, for instance, contain information about several different strains of the same disease or members of different species. Such processes are called marked spatio-temporal point processes, i.e. a random collection of points in time and space where each point has associated with it one or more further random variables describing the additional information. The vector of these additional random variables is called a mark.

Much of the theory of spatio-temporal point processes is based on the theory for spatial point processes. See the books by Diggle (2003) and Møller and Waagepetersen (2004) for many examples and theoretical developments of spatial point processes. Several approaches have been developed for the analysis of spatio-temporal point process data, usually motivated by a particular application. See Sahu and Mardia (2005) and Møller and Waagepetersen (2004, Section 2.4) for a comprehensive list of references.

4.1 Theory

A spatio-temporal point process $\Phi = \{[t_i, x_i]\}$ is defined as a locally finite set of points in a region $\mathbb{R} \times \mathcal{X}$ of time-space. The set $\mathcal{X}$ is usually a bounded subset of $\mathbb{R}^2$ or $\mathbb{R}^3$. In this framework, $\Phi(A)$ is the number of points $[t_i, x_i]$ in A, where $A \in \mathcal{B}(\mathbb{R} \times \mathcal{X})$, the Borel $\sigma-$algebra on $\mathbb{R} \times \mathcal{X}$. Usually, we restrict our attention to points on a finite time interval $[T_{0-}, T_{0+}]$. The point process Φ is made into a marked point process by attaching an attribute to each point of the process. We denote the marked point process on $\mathbb{R} \times \mathcal{X}$ by $\Psi = \{[t_i, x_i; m_i]\}$ where the marks are in $\mathcal{M} \subseteq \mathbb{R}^d$. In our model, we consider

functions of the marked point process $\Psi = \{[t_i, x_i; m_i]\}$ of the type

$$\sum_i f_{tx}(t_i, x_i; m_i), \tag{4.1}$$

where $t \in [T_{0-}, T_{0+}]$ for some $T_{0-}, T_{0+} \in \mathbb{R}$ and $x \in \mathcal{X}$.

Poisson point processes

The simplest and the most important random point patterns are the Poisson point processes. They serve as a tractable model class for "no interaction" in point patterns and they also serve as reference processes when summary statistics are studied and when more advanced point process models are defined (Møller and Waagepetersen, 2004). A Poisson process is a point process which satisfies two conditions: the number of events in any bounded set $A \in \mathcal{B}(\mathbb{R} \times \mathcal{X})$ follows a Poisson distribution with mean $\lambda \nu^k(A)$, where ν^k is the k-dimensional Lebesgue measure, and the constant λ is the intensity, or mean number of events per unit area; and the number of events in disjoint bounded Borel sets are independent. It follows that, conditional on the number of events in any bounded Borel set A, the locations of the events form an independent random sample for the uniform distribution on A (Stoyan *et al.*, 1995).

Moment relations

The various distributions of random variables are described by the means of such features as moments, particularly mean and variance, and generating functions. Point process theory has analogous tools for this. Here, numerical means and variances are replaced by moment measures. A more detailed description of the features discussed below can be found in Daley and Vere-Jones (2003) and Stoyan *et al.* (1995).

The intensity measure, or the first order moment measure, of Φ is denoted by Λ and given by

$$\Lambda(A) = \mathbb{E}\Phi(A).$$

Further, if $\Psi(A \times B)$ denotes the number of marked points $[t_i, x_i; m_i]$ with $[t_i, x_i] \in A$ and $m_i \in B$, $A \in \mathcal{B}(\mathbb{R} \times \mathcal{X})$ and $B \in \mathcal{B}(\mathcal{M})$, the intensity measure of the marked point process is defined by

$$\Lambda_m(A \times B) = \mathbb{E}\Psi(A \times B).$$

Since $\Lambda_m(\cdot \times B) << \Lambda$, there exists for each $(u, y) \in \mathbb{R} \times \mathcal{X}$ a probability distribution $P_{u,y}$ on $(\mathcal{M}, \mathcal{B}(\mathcal{M}))$ such that

$$\Lambda_m(A \times B) = \int_A P_{u,y}(B)\Lambda(du, dy),$$

see also Stoyan *et al.* (1995, p. 108). Note that $P_{u,y}$ can be interpreted as the distribution of the mark at (u, y).

The covariance structure of the unmarked point process is determined by the second-order factorial moment measure for Φ. It is defined for $A, A' \in \mathcal{B}(\mathbb{R} \times \mathcal{X})$ by

$$\alpha^{(2)}(A \times A') = \mathbb{E} \sum_{i \neq i'} \mathbb{1}\{[t_i, x_i] \in A, [t_{i'}, x_{i'}] \in A'\}.$$

The first order properties we derive in Paper A are independent of the underlying point process model. In contrast to this, the covariance structure depends on the specific choice of point process model. For a marked point process $\Psi = \{[t_i, x_i; m_i]\}$ with conditionally independent marks, such that given $\Phi = \{[t_i, x_i]\}$, $\{m_i\}$ are independent and $m_i \sim P_{t_i, x_i}$, the covariances can be expressed as follows. Let $A, A' \in \mathcal{B}(\mathbb{R} \times \mathcal{X})$ and $B, B' \in \mathcal{B}(\mathcal{M})$,

$$\text{Cov}(\Psi(A \times B), \Psi(A' \times B'))$$
$$= \int_{A \cap A'} P_{u,y}(B \cap B') \Lambda(du, dy)$$
$$+ \int_A \int_{A'} P_{u,y}(B) P_{u',y'}(B') \left[\alpha^{(2)}(du, dy, du', dy') - \Lambda(du, dy) \Lambda(du', dy') \right].$$

The second-order factorial moment measure $\alpha^{(2)}$ is equal to $\Lambda \times \Lambda$ if Φ is a Poisson point process, cf. Stoyan *et al.* (1995, p. 44). The covariance structure above thus has the following interpretation: if

$$\alpha^{(2)}(du, dy, du', dy') - \Lambda(du, dy) \Lambda(du', dy') > 0,$$

then pairs of activations are more likely to occur jointly at (u, y) and (u', y') than for a Poisson point process with intensity measure Λ.

Campbell-Mecke theorem

The Campbell-Mecke theorem (Mecke, 1967) simplifies calculations involving expectations of functions of point processes. We state the theorem for functions of the type (4.1), which is a slightly simplified form of the general Campbell-Mecke theorem for marked point processes, see Stoyan *et al.* (1995, p. 125). The theorem says that for $\Psi = \{[t_i, x_i; m_i]\}$ and any nonnegative measurable function f

$$\mathbb{E}\left(\sum_i f(t_i, x_i; m_i) \right) = \int_{\mathbb{R} \times \mathcal{X}} \int_{\mathcal{M}} f(u, y; m) P_{u,y}(dm) \Lambda(du, dy). \qquad (4.2)$$

Separability

The process Ψ is called separable if

(i) The intensity measure for the unmarked point process Φ fulfils

$$\Lambda = \Lambda_1 \times \Lambda_2,$$

where Λ_1 is a measure on $(\mathbb{R}, \mathcal{B}(\mathbb{R}))$ and Λ_2 is a measure on $(\mathcal{X}, \mathcal{B}(\mathcal{X}))$.

(ii) For $m = (m^1, m^2) \in \mathcal{M}_1 \times \mathcal{M}_2$, $\mathcal{M}_i \subseteq \mathbb{R}^{d_i}$, say, $i = 1, 2$, the distribution of the mark can be written as

$$P_{u,y} = P_u^1 \times P_y^2,$$

where P_u^1 is a probability measures on $(\mathcal{M}_1, \mathcal{B}(\mathcal{M}_1))$ and P_y^2 is a probability measure on $(\mathcal{M}_2, \mathcal{B}(\mathcal{M}_2))$. We call m^1 the temporal mark and m^2 the spatial mark.

This embodies the notion that the temporal behaviour of the process is independent of the spatial behaviour. Note, however, that the values of the temporal marks can still depend on location and the values for the spatial marks can similarly still depend on time.

When this is applied in Paper A, we further assume that the function of the point process considered is separable. That is, we assume that the function in (4.1) can be written in the form

$$f_{tx}(u, y; m) = g(t - u; m^1) h(x - y; m^2),$$

4.2 Model for fMRI data

In contrast to many point process datasets, we do not observe the points of the process, the starting times and spatial origins of activation, directly. Instead, we observe the activation in the brain, which are quite complicated in nature. A neuronal activation at location y and time u will contribute to the observed MR signal intensity at y at the later time $t > u$ by an amount proportional to

$$g(t - u)$$

where the function g describes the haemodynamic response, see Section 2.1. An activation in voxel y is expected to affect the signal at neighbour voxels in a similar way but with less intensity. An activation at location y and time u will affect the signal at voxel x and time $t > u$ by

$$g(t - u) h(x - y),$$

where $h(z)$ is a decreasing function of $\|z\|$, the norm of z. The resulting model for the contribution to the observed MR signal intensity at voxel x at time t caused by a neuronal activation at voxel y at time u becomes

$$f_{tx}(u, y; m) = g(t - u; m^1)h(x - y; m^2)$$

where $m = (m^1, m^2)$ and m^1 and m^2 are model parameters describing the shape of the temporal and the spatial activation, respectively. An illustration of this basic set up is shown in Figure 4.1.
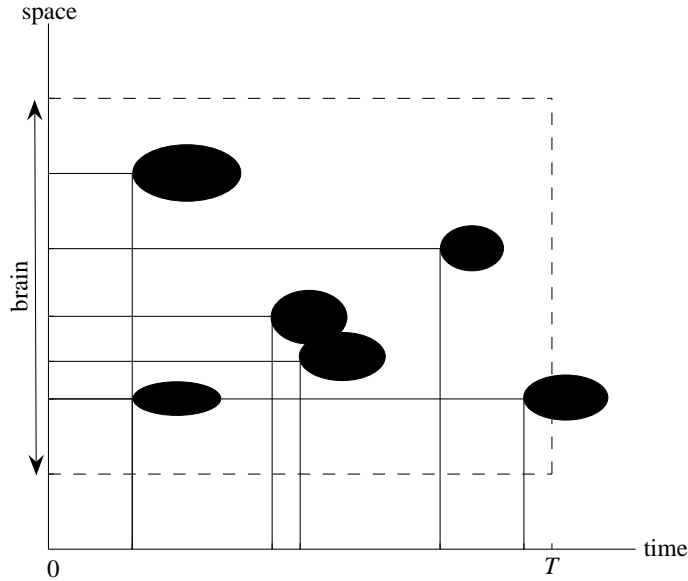
Figure 4.1: Illustration of the spatio-temporal point process model. Each ellipse illustrates the set of $(t, x) \in [0, T] \times \mathcal{X}$, affected by the activation in the leftmost point (t_i, x_i) of the ellipse. The mark m_i determines the shape and size of the ellipse.

The haemodynamic response and its modelling have been intensively studied, see e.g. Buxton *et al.* (2004) and references therein. We adopt a fairly simple but well known model from Friston *et al.* (1995) where the response is modelled as a Gaussian distributed random variable with mean 6 sec (the delay) and variance 9 sec^2. This model is shown in Figure 2.3 (left). The function g takes the form

$$g(u; m^1) = \int_0^{m^1} \kappa(u - v)dv,$$

25

where m^1 is the temporal duration of the activation and

$$\kappa(t) = \frac{1}{\sqrt{2\pi 3}} \exp\left(-\frac{(t-6)^2}{18}\right).$$

The spatial activation function is modelled by a Gaussian bell function

$$h(y; m^2) = \theta_1 \exp\left(-\frac{\|y\|^2}{2\theta_2}\right),$$

where $m^2 = (\theta_1, \theta_2)$.

In resting state fMRI data, the activations occur at random time points that are unknown to the experimenter. It is natural to describe the activations by a marked point process $\Psi = \{[t_i, x_i; m_i]\}$ on $\mathbb{R} \times \mathcal{X}$ with marks $m_i = (m_i^1, m_i^2) \in \mathbb{R}_+^3$. The resulting model for the observed MR signal intensity at time t and voxel x becomes

$$Z_{tx} = \mu_x + \sum_i f_{tx}(t_i, x_i; m_i) + \sigma \varepsilon_{tx}, \tag{4.3}$$

where μ_x is the baseline signal at voxel x and ε_{tx} is an error term with mean 0 and variance 1. The errors are expected to be correlated, see Lund *et al.* (2006) and Woolrich *et al.* (2004). It can be shown that this spatio-temporal model is closed under local smoothing, cf. Paper A.

Since the person being scanned is not subjected to systematic stimuli during the scanning, an activation can start in a given area at any time. It is therefore natural to assume (investigate) that the marked point process Ψ is time stationary in the sense that

$$\Psi_t = \{[t_i + t, x_i; m_i]\}$$

has the same distribution as Ψ for all $t \in \mathbb{R}$. Then, the intensity measure Λ of the unmarked point process is of the form

$$\Lambda = c\nu^1 \times \Lambda_2,$$

where $c > 0$, ν^1 is the Lebesgue measure on $\mathbb{R}$ and Λ_2 is the intensity measure for the spatial point process $\{x_i\}$. Furthermore, time stationarity implies that the mark distribution does not depend on the particular time point considered but it may still depend on the location.

Under the resting state network hypothesis, the spatio-temporal point process Ψ will show long-distance dependencies, see Fox *et al.* (2005) and De Luca *et al.* (2006). Recall that each marked point $[t_i, x_i; m_i]$ may be considered as a centre of activation at location $x_i \in \mathcal{X}$ starting at time t_i and with the

temporal and the spatial shape of the activation described by m_i. If two regions of the brain $\mathcal{X}_0$ and $\mathcal{X}_1$ interact, it is expected that activations occur almost simultaneously in $\mathcal{X}_0$ and $\mathcal{X}_1$. Such interactions may be revealed using a Bayesian analysis as discussed below. The earlier modelling of a "product brain" corresponds to the use of independent spatial and temporal point processes such that

$$\Psi = \{[t_i, x_j; m_i^1, m_j^2]\}, \tag{4.4}$$

where $\Psi_1 = \{[t_i; m_i^1]\}$ and $\Psi_2 = \{[x_j; m_j^2]\}$ are independent. If the intensity measure of Ψ_2 is very concentrated in $\mathcal{X}_0$ and $\mathcal{X}_1$, then activations will appear simultaneously in the two regions. This type of modelling of the dependency may appear somewhat simplistic and a model based on conditional independence may be more natural. Here,

$$\Psi = \{[t_i, x_{ij}; m_i^1, m_{ij}^2]\}, \tag{4.5}$$

where, given $\Psi_1 = \{[t_i; m_i^1]\}$, $\Psi_{2i} = \{[x_{ij}; m_{ij}^2]\}$ are independent and identically distributed with an intensity measure concentrated in $\mathcal{X}_0$ and $\mathcal{X}_1$, say. Examples of point processes fulfilling (4.4) and (4.5) are shown in Figure 4.2.
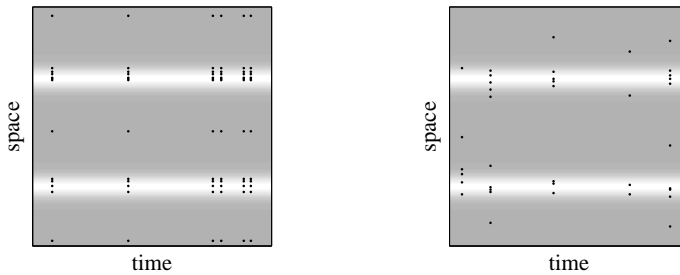
Figure 4.2: An example of a process fulfilling (4.4) with independent spatial and temporal Poisson processes (left) and an example of a process fulfilling (4.5) with conditionally independent Poisson processes (right). The associated intensity functions are shown in grey scale.

Classical inference

Here, we discuss within the framework of a separable model, the estimation of the intensity measure Λ_2 of the spatial point process under the resting state hypothesis. More general results and inference for conventional experiments with repeated stimuli are given in Paper A. We will consider the estimation of Λ_2 under the assumption that Λ_2 is a discrete measure concentrated in $y_j, j = 1, \ldots, N$, with masses $\lambda_2(y_j) = \Lambda_2(\{y_j\})$, $j = 1, \ldots, N$. Here, N may

be chosen as the number of voxels. Further, we assume that the marks are identical for all points in which case

$$\mathbb{E}Z_{tx} = \mu_x + \alpha_t\beta_x,$$

where

$$\alpha_t = c \int_{\mathbb{R}} g(t - u; m^1)du$$

and

$$\beta_x = \int_{\mathcal{X}} h(x - y; m^2)\Lambda_2(dy).$$

The method to be described is related to finding the regression estimate in linear regression. It can only be applied if the baseline intensity μ_x can be regarded as known. This is because the baseline intensity can vary by a factor of 2-3 across the brain, due to variation in the brain tissue as well as variations in the scanner. We can thus not assume that the baseline intensity is constant over voxels which means that we cannot distinguish between the baseline intensity and increased intensity due to activation in the relation

$$\mathbb{E}Z_{tx} = \mu_x + c\alpha_1(m^1)\beta_x,$$

where

$$\alpha_1(m^1) = \int_{\mathbb{R}} g(u; m^1)du.$$

If, however, μ_x can be regarded as known, we can let $\mu_x = 0$. Further, let $\{u_1, \ldots, u_M\}$ be the time points in the data and assume that they are equidistant with $\Delta := |u_k - u_{k-1}|$ for all $k = 2, \ldots, M$. This assumption is usually fulfilled for fMRI data. The spatial intensity function $\{\lambda_2(y_j)\}_{j=1}^N$ may be estimated for each fixed c, m^1, and m^2 by minimising

$$\sum_{i=1}^N \left[\bar{Z}_{\cdot y_i} - c\alpha_1(m^1)\sum_{j=1}^N h(y_i - y_j; m^2)\lambda_2(y_j)\right]^2 \Big/ \mathbb{V}\bar{Z}_{\cdot y_i},$$

where

$$\bar{Z}_{\cdot y_i} = \frac{1}{M}\sum_{k=1}^M Z_{u_k y_i}.$$

$\mathbb{V}\bar{Z}_{\cdot y_i}$ depends on both the data and the underlying point process, its precise form is given in Section 7.1 in Paper A.

This estimation method is simple, but requires that μ_x is known from external sources. If this is not feasible, one may try to get information about the intensity measure Λ_2 of the spatial point process from $\mathrm{Cov}(Z_{tx}, Z_{t',x'})$ instead. The covariances do not depend on the μ_xs. This approach, however,

depends on a specific point process model. As an example, let us consider the model for a non-stimulus experiment with both temporal and spatial processes Poisson. Irrespectively of whether the processes are independent or conditionally independent, (4.4) or (4.5), the mean value of the empirical covariance estimate

$$\hat{\sigma}_{x,x'} = \frac{1}{M-1} \sum_{k=1}^{M} (Z_{u_k x} - \bar{Z}_{\cdot x})(Z_{u_k x'} - \bar{Z}_{\cdot x'}),$$

can be approximated for x, x' with large mutual distance by

$$\mathbb{E}(\hat{\sigma}_{x,x'}) \approx c\gamma(m^1)\beta_x \beta_{x'},$$

where

$$\gamma(m^1) = \alpha_2(0; m^1) - \frac{2}{M(M-1)} \sum_{k=1}^{M-1} (M-k)\alpha_2(k\Delta; m^1),$$

with

$$\alpha_2(t; m^1) = \int_{-\infty}^{\infty} g(v; m^1)g(v+t; m^1)dv.$$

Assume that an activation centre $\mathcal{X}_0 \subset \mathcal{X}$ with N_0 points is known. Then, for x' with large mutual distance from all points $x \in \mathcal{X}_0$,

$$\mathbb{E}\left(\frac{1}{N_0} \sum_{x \in \mathcal{X}_0} \hat{\sigma}_{x,x'}\right) \approx c\gamma(m^1)\bar{\beta}_{\cdot} \sum_{i=1}^{N} h(x' - x_i; m^2)\lambda_2(x_i),$$

where

$$\bar{\beta}_{\cdot} = \frac{1}{N_0} \sum_{x \in \mathcal{X}_0} \beta_x.$$

This expression is linear in λ_2 if we regard $\bar{\beta}_{\cdot}$ as an unknown constant. We can thus use least squares methods to estimate $\lambda_2(x)$ for $x \in \mathcal{X} \setminus \mathcal{X}_0$ up to a constant, as above. Examples of this type of inference are given in Section 8 of Paper A.

Bayesian inference

We will now discuss Bayesian inference of the spatio-temporal point process model (4.3) and its parameters. A related model for repeated stimulus experiments has been developed in Hartvig (2002), see also Gössl *et al.* (2001). As before, μ_x requires a special treatment. When considering Bayesian methods we may simply replace Z_{tx} by $Z_{tx} - \bar{Z}_{\cdot x}$ and f_{tx} by $f_{tx} - \bar{f}_{\cdot x}$. The new data have $\mu_x = 0$ and the same correlation structure as the original data if M is large.

We concentrate on the case where $m_i = m$ and $\sigma_x^2 = \sigma^2$ are known. We then need to specify a prior density of the point process Φ and its parameters. The prior distribution of Φ will be chosen as Poisson with intensity function λ. Note that there is no interaction between points in the prior distribution. Interaction found in the posterior distribution of the point process will therefore be "caused" by the data. We consider the restriction

$$\Phi_0 = \Phi \cap ([T_{0-}, T_{0+}] \times \mathcal{X})$$

of Φ to a time interval $[T_{0-}, T_{0+}]$ containing $[0, T]$. The interval $[T_{0-}, T_{0+}]$ is chosen such that it is very unlikely that a point from $\Phi \backslash \Phi_0$ will affect an MR signal observed in $[0, T]$. The density of Φ_0 with respect to the unit rate Poisson process on $[T_{0-}, T_{0+}] \times \mathcal{X}$ becomes

$$p(\phi_0|c, \pi) = \exp(-\int_{[T_{0-}, T_{0+}] \times \mathcal{X}} [\lambda(t, x) - 1] dt dx) \prod_{[u,y] \in \phi_0} \lambda(u, y)$$

The intensity function of Φ is assumed to be of the following form

$$\lambda(t, x) = \sum_{l=1}^{k} \lambda_l \mathbb{1}\{x \in \mathcal{X}_l\},$$

where the sets $\mathcal{X}_l \subseteq \mathcal{X}$ are disjoint. Their union may be the whole brain $\mathcal{X}$ but need not be. The sets $\mathcal{X}_l$ should be specified by the experimenter while the parameters λ_l are unknown. We can write the intensity function as $\lambda(t, x) = c\lambda_2(x)$ where $c > 0$ and $\int_{\mathcal{X}} \lambda_2(x) dx = 1$. Note that λ_2 is on the following form

$$\lambda_2(x) = \sum_{l=1}^{k} \pi_l \frac{\mathbb{1}\{x \in \mathcal{X}_l\}}{|\mathcal{X}_l|},$$

where $\pi_l > 0$ and $\sum_{l=1}^{k} \pi_l = 1$. Non-informative priors are used for the parameters c and $\pi = (\pi_1, \ldots, \pi_k)$.

Let the data be denoted by

$$z = \{z_{ux} : u = u_1, \ldots, u_M, x \in \mathcal{X}\}.$$

Then, the conditional density of z given c, π, and ϕ_0 is

$$p_{m,\sigma^2}(z|\phi_0) = [2\pi\sigma^2]^{-NT/2} \exp(-\frac{1}{2\sigma^2} \|z - f(\phi_0; m)\|^2), \qquad (4.6)$$

where

$$\|z - f(\phi_0; m)\|^2 = \sum_{u,x} \left(z_{ux} - \sum_{[t_i, x_i] \in \phi_0} f_{ux}(t_i, x_i; m) \right)^2.$$

This is the simplest choice of model, see also Lund *et al.* (2006) and references therein. Note that (4.6) does not depend on c and π.

The posterior density will be of the form

$$p(c, \pi, \sigma^2, \phi_0|z) \propto p(c)p(\pi)p(\sigma^2)p(\phi_0|c, \pi)p(z|\phi_0, \sigma).$$

For the simulation from the posterior density we use a fixed scan Metropolis within Gibbs algorithm where in each scan c, π, and ϕ_0 are updated in turn. For a detailed description of algorithms of this kind, see Robert and Casella (2004). The full conditional for c is a Gamma distribution with restricted range while for $k > 2$ the full conditional of π is a Dirichlet distribution. Finally, we need to simulate from

$$p(\phi_0|c, \pi, z) \propto c^{n(\phi_0)} \prod_{l=1}^{k} \pi_l^{n_l(\phi_0)} \exp\Big(-\frac{1}{2\sigma^2}\|z - f(\phi_0)\|^2\Big).$$

Note that this is in fact a pairwise interaction density. The point process is simulated using a birth, death and move algorithm as described in Chapter 7 of Møller and Waagepetersen (2004).

Results for this type of analysis for simulated data can be found in Paper A and results for the dataset discussed earlier, see Figure 2.4 and 3.3, are given in Paper A and Paper B.

4.3   Extensions

The model and the inference described in the last section refer to the analysis performed in Paper A and Paper B. This can be extended in several ways, some of which are discussed in the following. A more detailed discussion can be found in Paper A. There is, however, a clear trade-off between precision in the modelling and computational complexity. It is thus important to try to find the right balance between the two, especially with models as complex in structure as our model.

Extended Bayesian inference

The Bayesian inference discussed above can be extended to include the remaining parameters, the mark m and the variance σ^2. A typical point will here be written as $[t, x; (\theta_0, \theta_1, \theta_2)] \in \mathbb{R} \times \mathcal{X} \times \mathbb{R}_+^3$, for convenience, so we write here θ_0 instead of m^1 for the temporal duration of the neuronal activation. As before, we write $m^2 = (\theta_1, \theta_2)$. The intensity function of Ψ is now assumed to be of the form

$$\lambda_\Psi(t, x; \theta_0, \theta_1, \theta_2) = \lambda(t, x) \prod_{i=0}^{2} \mathbb{1}\{\theta_i \in [a_i, b_i]\},$$

where a_i, b_i, $i = 0, 1, 2$, are known positive constants. The simulation will run as above but with some extra steps in the algorithm. If we give σ^2 a non-informative prior, its full conditional becomes an inverse Gamma distribution. Updating σ^2 by simulation a new value from that distribution should thus be added to each scan of the Metropolis within Gibbs algorithm. Further, the birth, death, and move algorithm for the simulation of the point process must be changed to account for varying marks. That is, the marks for a new point in a birth step should be drawn from the corresponding distribution and in a move step, new values of the marks should be suggested for the chosen point.

Models for the haemodynamic response

In the present work, we have mainly used the simple model based on a Gaussian density function for the temporal activity, as described in the previous section. One reason for this is that we want to focus on the spatial modelling. This model is also very simple in that it only has one unknown parameter, the duration of the activation. A slightly more complicated and maybe more realistic model is to use the difference of two Gamma functions, see Figure 2.3 (right). Here, one Gamma function is used to capture the main response and the other to capture the late undershoot. That is, the response function is modelled by

$$g(u; m^1) = \int_0^l \kappa(u - v)dv,$$

where l describes the duration of the activation and

$$\kappa(t) = \left[\left(\frac{t}{p_1} \right)^{a_1} \exp\left(-\frac{t - p_1}{b_1} \right) - c \left(\frac{t}{p_2} \right)^{a_2} \exp\left(-\frac{t - p_2}{b_2} \right) \right] \mathbb{1}\{t > 0\}.$$

Here, t is the time in seconds and $p_j = a_j b_j$ is the time to the peak. In our formulation, this means that the mark m^1 is now given by $m^1 = \{a_1, a_2, b_1, b_2, c, l\}$. Different models for the haemodynamic response function are reviewed in Genovese (2000), including a model based on splines which the author uses in his analysis.

The noise in the data

In fMRI experiments, data may have a more complicated noise structure that the one predicted by our model, cf. e.g. Hartvig (2002). An extension of the model will most likely include a drift component d_{tx}

$$Z_{tx} = \mu_x + d_{tx} + \sum_i f_{tx}(t_i, x_i; m_i) + \sigma_x \varepsilon_{tx},$$

cf. Genovese (2000). This component describes the slow drifts in the static magnetic field during the experiment and residual motion not accounted for by prior motion correction. Often, the drift is removed using filtering, before any further analysis of the data, cf. Friston *et al.* (2000), or included in a general linear model, cf. Friston *et al.* (1995). Artifacts of this kind can also be detected in the data using ICA, see Beckmann *et al.* (2000).

We have assumed that the errors $\{\varepsilon_{tx}\}$ are mutually independent. It is here important to consider more general error models. In particular, the noise is often autocorrelated in time, as emphasised in Worsley (2000). A more general model for the errors is the multivariate Gaussian model,

$$\varepsilon \sim N_{|\mathcal{X}| \times T}(0, \Sigma). \tag{4.7}$$

For a standard whole brain analysis, the covariance model Σ will be very large, e.g. $|\mathcal{X}| \times T = 10000 \times 100 = 10^6$. It is therefore necessary to make some simplifications of the model to make it computationally feasible. In Woolrich *et al.* (2004), this type of noise models is investigated in Bayesian settings. The authors propose the use of a space-time simultaneously specified autoregressive model,

$$\varepsilon_{tx} = \sum_{y \in \mathcal{N}_x} \beta_{xy} \varepsilon_{(t-1)y} + \sum_{s=1}^{3} \alpha_{sx} \varepsilon_{(t-s)x} + \eta_{tx},$$

where $\mathcal{N}_x$ is a neighbourhood of the voxel x, β_{xy} is the spatial autocorrelation between voxel x and y at a time lag of one with $\beta_{xy} = \beta_{yx}$, α_{sx} is the temporal autocorrelation between time point t and $t - s$ at voxel x, and $\{\eta_{tx}\}$ are independent noise variables with distribution

$$\eta_{tx} \sim N(0, \sigma_{\eta}^2).$$

Multiple point processes

In accordance with the emerging belief of the existence of more than one resting state network, it is natural to consider a point process model of the type $\Psi = \bigcup_{k=1}^{K} \Psi_k$ where $\Psi_k, k = 1, \ldots, K$, are independent and refer to activities in the K networks. If

$$\Psi_k = (\Psi_{k1}, \Psi_{k2})$$

where $\Psi_{k1} = \{[t_{ki}; m_{ki}^1]\}$ and $\Psi_{k2} = \{[x_{kj}; m_{kj}^2]\}$ are independent, then we obtain the following model equation

$$Z_{tx} = \mu_x + \sum_{k=1}^{K} A_{tk} B_{kx} + \sigma \varepsilon_{tx}, \tag{4.8}$$

where
$$A_{tk} = \sum_i g(t - t_{ki}; m^1_{ki}) \text{ and } B_{kx} = \sum_j h(x - x_{kj}; m^2_{kj}).$$

Note that (4.8) is actually an ICA model. The model may be analysed by first performing an ICA analysis and then analysing the estimated components, using point process theory.

34

5. Reconstruction of binary images

We now turn the discussion to the subject of noise removal for binary images. In fMRI analysis, mixture models of the type discussed below are used to identify the activated voxels from the statistical parametric map. This method is an alternative to the methods used in SPM, where the activated voxels are identified using the properties of some null distribution, see Section 3.1. We have chosen to discuss the matter within the general framework of noisy binary images of random sets in the plane.

Let Ξ be a stationary random set in $\mathbb{R}^2$ with values in the extended convex ring. The extended convex ring is the family of all closed subsets $H \in \mathbb{R}^2$ such that for all compact convex sets $K \in \mathbb{R}^2$, $H \cap K$ is a finite union of compact convex sets. A digitisation (or discretisation) of Ξ is the intersection of Ξ with a scaled lattice. For a fixed scaling factor $t > 0$, we consider $\Xi \cap t\mathbb{L}$, where

$$\mathbb{L} := \mathbb{Z}^2 = \{(i,j) : i,j \in \mathbb{Z}\}$$

is the usual lattice of points with integer coordinates. The lattice square

$$\mathbb{L}_n := \left\{(i,j) : i,j = -\frac{n-1}{2}, \ldots, \frac{n-1}{2}\right\}$$

consists of n^2 points ($n \geq 3, n$ odd). Here, we follow the notation in Hartvig and Jensen (2000) and place the lattice square around a centre pixel. This should not cause any conflicts in the notation, as we only consider lattice squares with odd number of points.

Further, let $X \subset t\mathbb{Z}^2$ for some $t > 0$. A binary image on a finite set X is a function $f : X \to \{0,1\}$. Here, f is given by $f(x) = \mathbb{1}\{x \in \Xi\}$ and f is thus a random function due to the randomness of the set Ξ. A certain pattern of the values of f on a $n \times n$ grid is called a configuration. It is denoted by C_t^n, where $t > 0$ is the resolution of the grid, as in the definition of a lattice above. The elements of the configuration are numbered to match the numbering of the elements in the lattice square $\mathbb{L}_n$. For $n = 3$ we have

$$C_t^3 = \begin{bmatrix} c_{-1,1} & c_{0,1} & c_{1,1} \\ c_{-1,0} & c_{0,0} & c_{1,0} \\ c_{-1,-1} & c_{0,-1} & c_{1,-1} \end{bmatrix}_t,$$

35

and similarly for other allowed values of n. We will omit the index n if the size of the configuration is clear from the context. Some examples of 3×3 configurations are

$$\begin{bmatrix} \bullet & \circ & \circ \\ \bullet & \circ & \circ \\ \bullet & \bullet & \circ \end{bmatrix}_t \quad \begin{bmatrix} \bullet & \circ & \circ \\ \bullet & \circ & \bullet \\ \bullet & \bullet & \circ \end{bmatrix}_t \quad \begin{bmatrix} \circ & \bullet & \bullet \\ \bullet & \circ & \circ \\ \bullet & \bullet & \circ \end{bmatrix}_t$$

where $\bullet$ means that $f(x) = 1$ or equivalently $\xi \cap \{x\} \neq \emptyset$, while $\circ$ means that $f(x) = 0$ or equivalently $\xi \cap \{x\} = \emptyset$. Here, ξ is the realisation of the random set Ξ observed in the image f.

The noisy binary image is denoted by $F : X \to \{0,1\}$ for a finite set $X \subset t\mathbb{Z}^2$ and $t > 0$. Note that the randomness in F is two-fold. First, the noise free image is random due to the randomness of the set Ξ. Second, a random noise is added to the image.

5.1 Restoration with configurations

In Paper D, we propose a Bayesian restoration model where the prior is based on results from configuration theory, see Jensen and Kiderlen (2003) and Kiderlen and Jensen (2003). The authors relate the probability of observing a given configuration in the image to the so-called mean normal measure of the set Ξ. The mean normal measure can be used for detecting and quantifying anisotropy of Ξ, its normalised version can be interpreted as the distribution of the outer normal at a "typical" boundary point of Ξ. If we assume the set Ξ to be isotropic, this relation is, under some regularity conditions for the structure of Ξ, given by

$$\lim_{t \to 0^+} \frac{1}{t} \mathbb{P}\big(\Xi \cap t(\mathbb{L}_n + x) = C_t\big)$$
$$= k \int_0^{2\pi} \min\big\{\langle a, (\cos\theta, \sin\theta)\rangle^+, \langle b, (\cos\theta, \sin\theta)\rangle^+\big\} d\theta, \qquad (5.1)$$

where $k > 0$ is a constant and the vectors $a, b \in \mathbb{R}^2$ depend on the configuration C_t. The vectors a and b can be calculated explicitly for each configuration. They are non-zero only if there exists a line passing through at least two points of the configuration, separating the black and the white points, and only hitting points of one colour. Configurations of this type are called informative configurations.

We assume that the resolution of the image is good enough, so that Equation 5.1 can be used to estimate the marginal probability of each informative configuration up to a constant of proportionality. In the case $n = 3$ we get,

for $x \in X$,

$$
\mathbb{P}\big(\Xi \cap (t\mathbb{L}_3 + x) = C_t\big) =
\begin{cases}
p_0, & C_t = \begin{bmatrix} \circ\,\circ\,\circ \\ \circ\,\circ\,\circ \\ \circ\,\circ\,\circ \end{bmatrix}_t \\[4pt]
p_1, & C_t = \begin{bmatrix} \bullet\,\bullet\,\bullet \\ \bullet\,\bullet\,\bullet \\ \bullet\,\bullet\,\bullet \end{bmatrix}_t \\[4pt]
p_2, & C_t \in R\left(\begin{bmatrix} \bullet\,\circ\,\circ \\ \bullet\,\circ\,\circ \\ \bullet\,\circ\,\circ \end{bmatrix}_t , \begin{bmatrix} \bullet\,\bullet\,\circ \\ \bullet\,\bullet\,\circ \\ \bullet\,\bullet\,\circ \end{bmatrix}_t \right) \\[4pt]
p_3, & C_t \in R\left(\begin{bmatrix} \circ\,\circ\,\circ \\ \bullet\,\bullet\,\bullet \\ \bullet\,\bullet\,\bullet \end{bmatrix}_t , \begin{bmatrix} \circ\,\circ\,\circ \\ \bullet\,\bullet\,\bullet \\ \bullet\,\bullet\,\bullet \end{bmatrix}_t \right) \\[4pt]
p_4, & C_t \in R\left(\begin{bmatrix} \bullet\,\bullet\,\circ \\ \bullet\,\bullet\,\bullet \\ \bullet\,\bullet\,\bullet \end{bmatrix}_t , \begin{bmatrix} \circ\,\circ\,\circ \\ \circ\,\circ\,\circ \\ \bullet\,\circ\,\circ \end{bmatrix}_t \right) \\[4pt]
p_5, & C_t \in R\left(\begin{bmatrix} \bullet\,\circ\,\circ \\ \bullet\,\circ\,\circ \\ \bullet\,\bullet\,\circ \end{bmatrix}_t , \begin{bmatrix} \bullet\,\bullet\,\circ \\ \bullet\,\circ\,\circ \\ \bullet\,\bullet\,\circ \end{bmatrix}_t , \begin{bmatrix} \bullet\,\bullet\,\circ \\ \bullet\,\bullet\,\bullet \\ \bullet\,\circ\,\circ \end{bmatrix}_t , \begin{bmatrix} \circ\,\circ\,\circ \\ \circ\,\circ\,\circ \\ \bullet\,\circ\,\circ \end{bmatrix}_t \right) \\[4pt]
0, & \text{otherwise,}
\end{cases}
$$

$$(5.2)$$

where $R(\cdot)$ is the set of all possible rotations and reflections. The probabilities $p_2, \ldots, p_5$ are determined from (5.1) up to a multiplicative constant c, which is given by

$$
c = \frac{1 - p_0 - p_1}{16}.
$$

Here, the parameters p_0 and p_1 must be estimated from the data. The prior for $n = 5$ is given in a similar way, see Paper D.

This prior will favour informative boundary configurations, such as

$$
\begin{bmatrix} \bullet\,\circ\,\circ \\ \bullet\,\circ\,\circ \\ \bullet\,\bullet\,\circ \end{bmatrix}_t \qquad \begin{bmatrix} \circ\,\circ\,\circ \\ \bullet\,\bullet\,\circ \\ \bullet\,\bullet\,\bullet \end{bmatrix}_t \qquad \begin{bmatrix} \circ\,\circ\,\circ \\ \circ\,\circ\,\circ \\ \bullet\,\bullet\,\bullet \end{bmatrix}_t
$$

while discourage non-informative configurations such as

$$
\begin{bmatrix} \bullet\,\circ\,\circ \\ \circ\,\circ\,\bullet \\ \bullet\,\bullet\,\circ \end{bmatrix}_t \qquad \begin{bmatrix} \circ\,\bullet\,\bullet \\ \bullet\,\circ\,\bullet \\ \bullet\,\bullet\,\circ \end{bmatrix}_t \qquad \begin{bmatrix} \circ\,\bullet\,\circ \\ \circ\,\circ\,\circ \\ \bullet\,\bullet\,\bullet \end{bmatrix}_t
$$

which are more likely to be incorrect or noisy if the set Ξ is fairly regular and the resolution of the image is good.

For the restoration procedure, we assume that the values $F(x_i)$ and $F(x_j)$ of the noisy image at x_i and x_j are conditionally independent given Ξ for all $x_i, x_j \in X$, and that the conditional distribution of $F(x)$ given Ξ only depends on $\Xi \cap \{x\}$ for all $x \in X$. By Bayes rule we thus get, for $x \in X$ and a given configuration C_t,

$$
\mathbb{P}\big(\Xi \cap (t\mathbb{L}_n + x) = C_t | F(t\mathbb{L}_n + x)\big)
$$

$$
\propto \mathbb{P}\big(\Xi \cap (t\mathbb{L}_n + x) = C_t\big) \prod_{k=1}^{n^2} p\big(F(y_k) | \Xi \cap \{y_k\} = \{c_k\}\big),
$$

where $\{y_k\}_{k=1}^{n^2} = t\mathbb{L}_n + x$ and $\{c_k\}_{k=1}^{n^2} = C_t$.

By summing over the neighbouring states, we obtain the probability of Ξ hitting a single point $x \in X$,

$$\mathbb{P}\big(\Xi \cap \{x\} \neq \emptyset | F(t\mathbb{L}_n + x)\big)$$

$$\propto \sum_{\{C_t : c_{00} = \bullet\}} \mathbb{P}\big(\Xi \cap (t\mathbb{L}_n + x) = C_t\big) \prod_{k=1}^{n^2} p\big(F(y_k)|\Xi \cap \{y_k\} = \{c_k\}\big)$$

$$=: S_1(x).$$

The probability of Ξ not hitting a single point $x \in X$ is obtained in a similar way. It is given by

$$\mathbb{P}\big(\Xi \cap \{x\} = \emptyset | F(t\mathbb{L}_n + x)\big)$$

$$\propto \sum_{\{C_t : c_{00} = \circ\}} \mathbb{P}\big(\Xi \cap (t\mathbb{L}_n + x) = C_t\big) \prod_{k=1}^{n^2} p\big(F(y_k)|\Xi \cap \{y_k\} = \{c_k\}\big)$$

$$=: S_2(x).$$

As the probabilities above sum to one, we only need to compare $S_1(x)$ and $S_2(x)$ for determining the restored value of the image for a pixel x. The restored value is 1 if $S_1(x) > S_2(x)$ and 0 otherwise.

We consider the alt and pepper model for the noise. That is, a black point is replaced by a white point with probability q, and vice versa. More precisely,

$$p\big(F(x)|\Xi \cap \{x\}\big) = q^{F(x)}(1-q)^{1-F(x)}\mathbb{1}\big\{\Xi \cap \{x\} = \emptyset\big\}$$
$$+ (1-q)^{F(x)}q^{1-F(x)}\mathbb{1}\big\{\Xi \cap \{x\} \neq \emptyset\big\},$$

for some $0 \leq q \leq 1$. The parameter q will be estimated from the data.

The three unknown parameters p_0, p_1, and q are estimated by first maximising the contrast function of a single voxel,

$$\gamma_m(p_0, p_1, q) = \sum_{x \in X} \log p\big(F(x); p_0, p_1, q\big),$$

where $p\big(F(x); p_0, p_1, q\big)$ is the marginal density of the point x. That information is subsequently used to maximise the contrast function of a whole neighbourhood,

$$\gamma(p_0, p_1, q) = \sum_{x \in X} \log p\big(F(t\mathbb{L}_n + x); p_0, p_1, q\big),$$

where $p\big(F(t\mathbb{L}_n + x); p_0, p_1, q\big)$ is the marginal density of an $n \times n$ neighbourhood, on a grid of values. In this way, we get a global estimation of the

parameters which is related to maximum likelihood estimation. If done precisely, this will give unbiased estimators that are consistent and asymptotically normal under mild regularity conditions on the spatial correlation of the process (Hartvig, 2000). The approximation of using only a grid of values is performed in order to reduce the computation time and seems to work quite well, see Paper D.

5.2 Mixture models

In Hartvig and Jensen (2000), the authors proposed three different prior models for a similar type of reconstruction method as is described in the previous section. These models also reflect the idea, that pixels of one colour tend to cluster, rather than appear as single isolated pixels. They, however, do not take the actual spatial pattern of the neighbourhood into account.

Let $s(C_t) := \sum_{k=1}^{n^2} \mathbb{1}\{c_k = \bullet\}$. The prior for the simplest model is, for $x \in X$, given by

$$\mathbb{P}\big(\Xi \cap (t\mathbb{L}_n + x) = C_t\big) = \begin{cases} p_0, & \text{if } s(C_t) = 0, \\ p_1, & \text{if } s(C_t) > 0. \end{cases} \tag{5.3}$$

Since all configurations with at least one $\bullet$ have the same probability, this is in a way an uninformative prior, which neither favours isolated black pixels, nor large groups of black pixels. An extension of this model is

$$\mathbb{P}\big(\Xi \cap (t\mathbb{L}_n + x) = C_t\big) = \begin{cases} p_0, & \text{if } s(C_t) = 0, \\ \alpha\beta^{s(C_t)-1}, & \text{if } s(C_t) > 0. \end{cases} \tag{5.4}$$

The third prior model is more symmetric with respect to black and white pixels and more similar to our prior model in (5.2). It is given by

$$\mathbb{P}\big(\Xi \cap (t\mathbb{L}_n + x) = C_t\big) = \begin{cases} p_0, & \text{if } s(C_t) = 0, \\ \alpha_1\beta_1^{s(C_t)-1} + \alpha_2\beta_2^{s(C_t)-n^2}, & \text{if } 1 \leq s(C_t) \leq n^2, \\ p_1, & \text{if } s(C_t) = n^2. \end{cases} \tag{5.5}$$

In a previous work, Everitt and Bullmore (1999), considered the same basis model as above, but without using any spatial information. Their approach is equivalent to the prior model in (5.4) with the restriction that $\alpha = \beta/(\beta+1)^{n^2}$. This corresponds to assuming that all the pixels are spatially independent. Spatial information seems, however, to be very important for obtaining a good estimate of the underlying noise-free image and Hartvig and Jensen (2000) showed that their method outperforms the method of Everitt and Bullmore (1999) substantially when the objective is to identify activated voxels from a statistical parametric map in fMRI data analysis.

5.3 Markov random field models

In Besag (1986), the author presented an iterative method for image reconstruction where the local characteristics of the underlying true image are represented by a non-degenerate Markov random field. The author calls his method iterated conditional modes (ICM). The prior models here are of the type

$$p\big(\{f(x)\}_{x\in X}\big) \propto \exp\Big(\sum_{x_i\in X} G_i\big(f(x_i)\big) + \sum_{x_i,x_j\in X} G_{ij}\big(f(x_i), f(x_j)\big)\Big), \quad (5.6)$$

for some functions G_i and G_{ij}. To ensure the Markov property, one assumes that $G_{ij} \equiv 0$ unless x_i and x_j are neighbours. As the name of the method indicates, the estimation under the model is performed iteratively where the possible parameters of the model and the reconstructed point pattern are updated in turn. This method is very flexible, as the functions G_i and G_{ij} can be chosen arbitrarily, and has a natural extension to multicolour settings. It can, however, be computationally quite intensive and depends on a smoothing parameter that cannot be directly estimated from the data.

An extension of this method is the maximum a posteriori (MAP) method proposed in Greig *et al.* (1989). The authors concentrate on a special case of (5.6) and define their prior model by

$$p\big(\{f(x)\}_{x\in X}\big) \propto \exp\Big(\frac{1}{2} \sum_{x_i,x_j\in X} \beta_{ij}\mathbb{1}\big\{f(x_i) = f(x_j)\big\}\Big),$$

where $\beta_{ii} = 0$ and $\beta_{ij} = \beta_{ji} \geq 0$ with $\beta_{ij} > 0$ only if x_i and x_j are neighbours. In the actual analysis, this is simplified somewhat to

$$p\big(\{f(x)\}_{x\in X}\big) \propto \exp(\beta\nu), \quad (5.7)$$

where $\beta > 0$ is a parameter in the model and ν is the number of neighbour pairs with the same colour. The MAP estimate is the estimate for $\{f(x)\}_{x\in X}$ providing a maximal value of the posterior density. The authors show that finding the estimate is equivalent to finding the minimum cut in a network, a problem for which there exists an efficient algorithm. The multicolour setting can though not be directly dealt with by this method and there is still the problem of the smoothness parameter β which cannot be directly estimated from data.

5.4 Comparison of methods

For comparison of the models described above, we have used our model to reconstruct noisy versions of the image of an "A" from Greig *et al.* (1989).
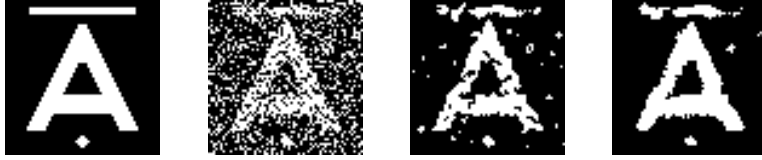
Figure 5.1: The 64×64 binary image of an "A" by Greig *et al.* (1989) (a), the same image corrupted with salt and pepper noise with parameter $q = 0.25$ (b), the estimated true image using the model described in Section 5.1 with $n = 3$ (c), and the estimate using the same model, but with $n = 5$ (d).

The true image and an example of a noisy version are shown in Figure 5.1 (a) and (b), respectively, and the corresponding reconstructed images are shown in Figure 5.1 (c) for $n = 3$ and in Figure 5.1 (d) for $n = 5$. The same image has been used as an example in Greig *et al.* (1989), where it was reconstructed using the prior from (5.7) for both ICM and MAP for several values of the smoothing parameter β, and in Hartvig and Jensen (2000).

Table 5.1: Estimated classification errors for the models described above based on five independent reconstructions of noisy versions of the image in Figure 5.1 (a). The results are given in percentage, standard errors are given in parentheses. The models are denoted by the equation number where they are defined in the text above. All results except for the model defined in (5.2) are reproduced from Hartvig and Jensen (2000) and Greig *et al.* (1989).

Model	Class. error
(5.2), 3×3	7.7 (0.4)
(5.2), 5×5	4.7 (0.3)
(5.3), 3×3	10.0 (0.3)
(5.3), 5×5	9.4 (0.2)
(5.4), 3×3	7.6 (0.3)
(5.4), 5×5	5.9 (0.8)
(5.5), 3×3	7.6 (0.3)
(5.5), 5×5	6.1 (0.3)
ICM	6.3 (0.4)
MAP	5.2 (0.2)

We have reproduced the results from Greig *et al.* (1989) and Hartvig and Jensen (2000) in Table 5.1, which also shows the results from the reconstruction with our model. For ICM and MAP, we only show the classification error for the value of β which gave the best results. The classification error has in

all cases been calculated from five independent simulations of the degraded image with the noise parameter $q = 0.25$. The table shows that our model performs better or equally good as the other methods for $n = 5$ and the results for $n = 3$ are comparable to the results from Hartvig and Jensen (2000) for $n = 3$, even though the "random" set here is far from being isotropic which is assumed in the prior in (5.2).

Bibliography

Bandettini, P., Petridou, N., and Bodurka, J. (2005). Direct detection of neuronal activity with MRI: fantasy, possibility, or reality? *Journal of Applied Magnetic Resonance*, **29**(1), 65–88.

Bandettini, P. A. and Ungerleider, L. G. (2001). From neuron to BOLD: new connections. *Nature Neuroscience*, **4**(9), 864–866.

Bartels, A. and Zeki, S. (2004). The neural correlates of maternal and romantic love. *NeuroImage*, **21**, 1155Ũ–1166.

Bartels, A. and Zeki, S. (2005). The chronoarchitecture of the cerebral cortex. *Philosophical Transactions of the Royal Society of London, B*, **360**(1456), 733–750.

Beckmann, C. and Smith, S. (2004). Probabilistic independent component analysis for functional magnetic resonance imaging. *IEEE Transactions on Medical Imaging*, **23**(2), 137–152.

Beckmann, C. F. and Smith, S. M. (2005). Tensorial extensions of independent component analysis for multisubject fMRI analysis. *NeuroImage*, **25**, 294–311.

Beckmann, C. F., Noble, J. A., and Smith, S. M. (2000). Artefact detection in FMRI data using independent component analysis. In P. T. Fox and J. L. Lancaster, editors, *Sixth International Conference on Functional Mapping of the Human Brain, NeuroImage*, volume 11, page S614. Academic Press.

Beckmann, C. F., DeLuca, M., Devlin, J. T., and Smith, S. M. (2005). Investigations into resting-state connectivity using independent component analysis. *Philosophical Transactions of the Royal Society B*, **360**, 1001–1013.

Benjamini, Y. and Hochberg, Y. (1995). Controlling false discovery rates - A practical and powerful approach to multiple testing. *Journal of the Royal Statistical Society, Series B*, **57**, 289–300.

Besag, J. (1986). On the statistical analysis of dirty pictures. *Journal of the Royal Statistical Society, Series B*, **48**(3), 259–302.

Biswal, B., Yetkin, F. Z., Haughton, V. M., and Hyde, J. S. (1995). Functional connectivity in the motor cortex of resting human brain using echo-planar MRI. *Magnetic Resonance in Medicine*, **34**(4), 537–541.

Buxton, R., Uludağ, K., Dubowitz, D., and Liu, T. (2004). Modelling the hemodynamic response to brain activation. *NeuroImage*, **23**, 220–233.

Daley, D. and Vere-Jones, D. (2003). *An Introduction to the Theory of Point Processes*, volume I: Elementary Theory and Methods. Springer, 2nd edition.

De Luca, M., Beckmann, C., De Stefano, N., Matthews, P., and Smith, S. (2006). fMRI resting state networks define distinct modes of long-distance interactions in the human brain. *NeuroImage*, **29**(4), 1359–1367.

Diggle, P. J. (2003). *Statistical Analysis of Spatial Point Patterns*. Hodder Arnold, 2nd edition.

Everitt, B. S. and Bullmore, E. T. (1999). Mixture model mapping of brain activation in functional magnetic resoncance imaging. *Human Brain Mapping*, **7**, 1–14.

Fox, M. D., Snyder, A. Z., Vincent, J. L., Corbetta, M., Van Essen, D. C., and Raichle, M. E. (2005). The human brain is intrinsically organized into dynamic, anticorrelated functional networks. *Proceedings of the National Academy of Sciences, USA*, **102**(27), 9673–9678.

Frackowiak, R., Friston, K., Frith, C., Dolan, R., Price, C., Zeki, S., Ashburner, J., and Penny, W., editors (2003). *Human Brain Function*. Academic Press, 2nd edition.

Friston, K. (1998). Modes or models: a critique on independent component analysis for fMRI. *Trends in Cognitive Sciences*, **2**, 373–375.

Friston, K., Josephs, O., Zarahan, E., Holmes, A., Rouquette, S., and Poline, J.-B. (2000). To smooth or not to smooth? Bias and efficiency in fMRI time-series analysis. *NeuroImage*, **12**, 196–208.

Friston, K., Glaser, D., Henson, R., Kiebel, S., Phillips, C., and Ashburner, J. (2002a). Classical and Bayesian inference in neuroimaging: Applications. *NeuroImage*, **16**, 484–512.

Friston, K., Penny, W., Phillips, C., Kiebel, S., Hinton, G., and Ashburner, J. (2002b). Classical and Bayesian inference in neuroimaging: Theory. *NeuroImage*, **16**, 465–483.

Friston, K. J., Holmes, A. P., Poline, J.-B., Grasby, P. J., Williams, S. C. R., Frackowiak, R. S. J., and Turner, R. (1995). Analysis of fMRI time series revisited. *NeuroImage*, **2**(1), 45–53.

Genovese, C., Lazar, N., and Nichols, T. (2002). Thresholding of statistical maps in functional neuroimaging using false discovery rates. *NeuroImage*, **15**, 870–878.

Genovese, C. R. (2000). A Bayesian time-course model for functional magnetic resonance imaging. *Journal of the American Statistical Association*, **95**(451), 691–719. With discussion.

Gössl, C., Auer, D., and Fahr, L. (2001). Bayesian spatiotemporal inference in functional magnetic resonance imaging. *Biometrics*, **57**, 554–562.

Gray, H. (1918). *Anatomy of the human body*. Lea & Febiger, Philadelphia, 20th edition. Thoroughly revised and re-edited by Warren H. Lewis. Bartleby.com, 2000. www.bartleby.com/107 [19.07.2006].

Greicius, M. D. and Menon, V. (2004). Default-mode activity during a passive sensory task: Uncoupled from deactivation but impacting activation. *Journal of Cognitive Neuroscience*, **16**, 1484–1492.

Greicius, M. D., Krasnov, B., Reiss, A. L., and Menon, V. (2003). Functional connectivity in the resting brain: a network analysis of the default mode hypothesis. *Proceeding of the National Academy of Sciences, USA*, **100**(1), 253–258.

Greicius, M. D., Srivastava, G., Reiss, A. L., and Menon, V. (2004). Default-mode network activity distinguishes Alzheimer's disease from healthy aging: evidence from functional MRI. *Proceeding of the National Academy of Sciences, USA*, **101**(13), 4637–4642.

Greig, D., Porteous, B., and Seheult, A. (1989). Exact maximum a posteriori estimation for binary images. *Journal of the Royal Statistical Society, Series B*, **51**(2), 271–279.

Haacke, E. M., Brown, R., Thompson, M., and Venkatesan, R. (1999). *Magnetic Resonance Imaging: Physical Principles and Sequence Design*. John Wiley.

Hartvig, N. (2002). A stochastic geometry model for functional magnetic resonance imaging data. *Scandinavian Journal of Statistics*, **29**, 333–353.

Hartvig, N. V. (2000). *Parametric modelling of functional magnetic resonance imaging data*. Ph.D. thesis, University of Aarhus.

Hartvig, N. V. and Jensen, J. L. (2000). Spatial mixture modeling of fMRI data. *Human Brain Mapping*, **11**, 233–248.

Hasson, U., Nir, Y., Levy, I., Fuhrmann, G., and Malach, R. (2004). Inter-subject synchronization of cortical activity during natural vision. *Science*, **303**, 1634–1640.

Hochstein, S. and Ahissar, M. (2002). View from the top: Hierarchies and reverse hierarchies in the visual system. *Neuron*, **36**, 791–804.

Horwitz, B. and Poeppel, D. (2002). How can EEG/MEG and fMRI/PET data be combined? *Human Brain Mapping*, **17**, 1–3.

Hyvärinen, A. and Oja, E. (2000). Independent component analysis: Algorithms and applications. *Neural Networks*, **13**(4–5), 411–430.

Ives, J., Warach, S., Schmitt, F., Edelman, R., and Schomer, D. (1993). Monitoring the patient's EEG during echo planar MRI. *Electroencephalography and Clinical Neurophysiology*, **87**, 417–420.

Jenkinson, M. (2003). Fast, automated, N-dimensional phase-unwrapping algorithm. *Magnetic Resonance in Medicine*, **49**(1), 193–197.

Jensen, E. B. V. and Thorarinsdottir, T. L. (2006). Spatio-temporal model for fmri data - with a view to resting state networks. To appear in *Scandinavian Journal of Statistics*.

Jensen, E. V. V. and Kiderlen, M. (2003). Directional analysis of digitized planar sets by configuration counts. *Journal of Microscopy*, **212**(2), 158–168.

Jezzard, P. and Buxton, R. B. (2006). The clinical potential of functional magnetic resonance imaging. *Journal of Magnetic Resonance Imaging*, **23**, 787–793.

Kiderlen, M. and Jensen, E. B. V. (2003). Estimation of the directional measure of planar random sets by digitization. *Advances in Applied Probability*, **35**, 583–602.

Logothesis, N. K. (2003). The underpinnings of the BOLD functional magnetic resonance imaging signal. *The Journal of Neuroscience*, **23**(10), 3963–3971.

Logothetis, N. and Wandell, B. A. (2004). Interpreting the BOLD signal. *Annual Review Physiology*, **66**, 735–769.

Logothetis, N. K., Pauls, J., Augath, M., Trinath, T., and Oeltermann, A. (2001). Neurophysiological investigation of the basis of the fMRI signal. *Nature*, **412**, 150–157.

Lund, T. E., Madsen, K. H., Sidaros, K., Luo, W.-L., and Nichols, T. E. (2006). Non-white noise in FMRI: Does modelling have an impact? *NeuroImage*, **29**, 54–66.

Marchini, J. and Presanis, A. (2004). Comparing methods of analyzing fmri statistical parametric maps. *NeuroImage*, **22**, 1203–1213.

McKeown, M. J., Hansen, L. K., and Sejnowski, T. J. (2003). Independent component analysis of functional MRI: What is signal and what is noise? *Current Opinion in Neurobiology*, **13**, 620–629.

Mecke, J. (1967). Staionäre zufällige masse of lokal-kompakten abelschen gruppe. *Zeitschrift für Wahrscheinlichkeitstheorie und verwandte Gebiete*, **9**, 36–58.

Møller, J. and Waagepetersen, R. P. (2004). *Statistical Inference and Simulation for Spatial Point Processes*. Chapmann & Hall/CRC.

Mukame, R., Gelbard, H., Arieli, A., Hasson, U., Fried, I., and Malach, R. (2005). Coupling between neuronal firing, field potentials, and fMRI in human auditory cortex. *Science*, **309**(5736), 951–954.

Oakes, T., Johnstone, T., Ores Walsh, K., Greischar, L., Alexander, A., Fox, A., and Davidson, R. (2005). Comparison of fMRI motion correction software tools. *NeuroImage*, **28**(3), 529–543.

Ogawa, S., Lee, T., Kay, A., and D.W., T. (1990). Brain magnetic resonance imaging with contrast dependent on blood oxygenation. *Proceedings of the National Academy of Sciences, USA*, **87**, 9868–9872.

Poline, J.-B., Strother, S. C., Dehaene-Lambertz, G., Egan, G. F., and Lancaster, J. L. (2006). Motivation and synthesis of the FIAC experiment: Reproducibility of fMRI results across expert analyses. *Human Brain Mapping*, **27**(5), 351–359.

Raichle, M. E. and Mintun, M. A. (2006). Brain work and brain imaging. *Annual Review of Neuroscience*, **29**, 449–476.

Robert, C. and Casella, G. (2004). *Monte Carlo Statistical Methods*. Springer, New York, 2nd edition.

Sahu, S. K. and Mardia, K. V. (2005). Recent trends in modeling spatio-temporal data. In *Meeting of the Italian Statistical Society on Statistics and the Environment, Messina, Italy, 21-23 Sep 2005*, pages 69–83.

Schoenberg, F., Brillinger, D., and Guttorp, P. (2002). Point processes, spatial-temporal. In A. El-Shaarawi and W. Piegorsch, editors, *Encyclopedia of Environmetrics*, volume 3, pages 1573–1577. Wiley, Chichester.

Smith, S. M., Jenkinson, M., Woolrich, M. W., Beckmann, C. F., Behrens, T. E. J., Johansen-Berg, H., Bannister, P. R., De Luca, M., Drobnjak, I., Flitney, D. E., Niazy, R. K., Saunders, J., Vickers, J., Zhang, Y., De Stefano, N., Brady, J. M., and Matthews, P. M. (2004). Advances in functional and structural MR image analysis and implementation as FSL. *NeuroImage*, **23**, 208–219.

Stoyan, D., Kendall, W. S., and Mecke, J. (1995). *Stochastic Geometry and its Applications*. Wiley, 2nd edition.

Talairach, P. and Tournoux, J. (1988). *A Stereotactic Coplanar Atlas of the Human Brain*. Stuttgart Thieme.

Thorarinsdottir, T. L. (2006). Bayesian image restoration, using configurations. To appear in *Image Analysis & Stereology*.

Thorarinsdottir, T. L. and Jensen, E. B. V. (2006). Modelling resting state networks in the human brain. In R. Lechnerová, I. Saxl, and V. Beneš, editors, *Proceedings S^4G: International Conference on Stereology, Spatial Statistics and Stochastic Geometry*.

Thorarinsdottir, T. L. and Stødkilde-Jørgensen, H. (2006). Functional imaging of pelvic floor muscle control. To appear as Thiele Research Report, Department of Mathematical Sciences, University of Aarhus.

Triantafyllou, C., Hoge, R., Krueger, G., Wiggins, C., Potthast, A., Wiggins, G., and Walda, L. (2005). Comparison of physiological noise at 1.5 T, 3 T and 7 T and optimization of fMRI acquisition parameters. *NeuroImage*, **26**, 243–250.

Wan, X., Iwata, K., Riera, J., Kitamura, M., and Kawashima, R. (2006). Artifact reduction for simultaneous EEG/fMRI recording: Adaptive FIR reduction of imaging artifacts. *Clinical Neurophysiology*, **117**(3), 681–692.

48

Woolrich, M. W., Jenkinson, M., Brady, J. M., and Smith, S. M. (2004). Fully Bayesian spatio-temporal modeling of FMRI data. *IEEE Transactions of Medical Imaging*, **23**(2), 213–231.

Worsley, K. (1994). Local maxima and the expected Euler characteristic excursion sets of χ^2, F, and t fields. *Advances in Applied Probability*, **26**, 13–42.

Worsley, K. (2000). Comment on "A Bayesian time-course model for functional magnetic resonance imaging" by C. Genovese. *Journal of the American Statistical Association*, **95**(451), 691–719.

Worsley, K. and Friston, K. J. (1995). Analysis of fMRI time series revisited - Again. *NeuroImage*, **2**, 173–181.

Worsley, K., Marrett, S., Neelin, P., and Evans, A. (1992). A three-dimensional statistical analysis for CBF activation studies in human brain. *Journal of Cerebral Blood Flow and Metabolism*, **12**, 900–918.

Eva B. Vedel Jensen and
Thordis L. Thorarinsdottir (2006).
**A spatio-temporal model for fMRI data
- with a view to resting state networks.**
To appear in *Scandinavian Journal of
Statistics.*

A spatio-temporal model for fMRI data - with a view to resting state networks

Eva B. Vedel Jensen and Thordis L. Thorarinsdottir
University of Aarhus

Abstract

Functional magnetic resonance imaging (fMRI) is a technique for studying the active human brain. During the fMRI experiment, a sequence of MR images is obtained, where the brain is represented as a set of voxels. The data obtained are a realization of a complex spatio-temporal process with many sources of variation, both biological and technical. Most current model-based methods of analysis are based on a two-step procedure. The initial step is a voxel-wise analysis of the temporal changes in the data while the spatial part of the modeling is done separately as a second step in the analysis. We present a spatio-temporal point process model approach for fMRI data where the temporal and spatial activation are modeled simultaneously. This modeling framework allows for more flexibility in the experimental design than most standard methods. It is also possible to analyze other characteristics of the data than just the locations of active brain regions, such as the interaction between the active regions. In this paper, we discuss both classical statistical inference and Bayesian inference in the model. We analyze simulated data without repeated stimuli both for location of the activated regions and for interactions between the activated regions. An example of analysis of fMRI data, using this approach, is presented.

1 Introduction

Functional Magnetic Resonance Imaging (fMRI) is a non-invasive imaging technique that has been available for about ten years. Cognitive psychologists and neuroscientists have shown an enormous interest in fMRI because it is believed that fMRI can reveal the human brain in action. There is a comprehensive literature on the topic, mainly in *Human Brain Mapping*, *Magnetic Resonance in Medicine* and *NeuroImage*, reporting various empirical findings and new methods of analysis.

During a typical fMRI experiment, the subject is asked to perform specific behavioral tasks (like finger-tapping or calculations) or the subject is exposed

to passive stimulus (like flashing light). The experiment is carefully designed with periods of rest ('off periods') between periods of stimuli ('on periods'). The brain is scanned during the experiment and represented as a set of voxels. At each voxel a time series is recorded, showing the local brain activity during the experiment. An informative introduction for statisticians to the design of fMRI experiments can be found in the paper by Genovese (2000).

The analysis of fMRI data is usually aimed at localizing the activated or de-activated parts of the brain during the experiment. The initial analysis is often performed voxel-wise, using the time series available at each voxel. The variation in the local signal intensity is analyzed using a temporal model, involving the known design of the experiment and the hemodynamic response function. Using this technique, local activation estimates based on level changes during on and off periods are assessed. Spatial modeling of fMRI data is usually done after the image of voxel-wise activation estimates (for instance an image of $p-$values for activation tested by $t-$tests) is obtained. The most common approach is to use Gaussian random field theory for this part of the modeling, see Friston $et\ al.$ (1995) and Cao and Worsley (1999). The approach is not without problems since the threshold value will depend on the search volume. This type of procedure, involving generalized linear models, has been implemented in the SPM (Statistical Parametric Mapping) software package. The package has been developed by members and collaborators of the Wellcome Department of Imaging Neuroscience, UCL, UK.

In Genovese (2000), a fully Bayesian analysis of fMRI data is discussed, see also Friston (2002), Friston $et\ al.$ (2002a), and Friston $et\ al.$ (2002b). The model still only involves one voxel at a time but is very heavy computationally. In the comments to Genovese (2000), see Worsley (2000), it is suggested to try to spatially link the voxel-wise models. In recent times, ICA (independent component analysis) has become quite popular, cf. Stone (2002), McKeown $et\ al.$ (2003), and Beckmann and Smith (2005). See also the early critical comments in Friston (1998). Techniques for detecting functional clusters have been described in Tonini $et\ al.$ (1998).

Especially amongst psychologists there has been some criticism of the localization paradigm. They argue that psychological processes are probably not realized as static constellations. Also, it is believed that the repeated stimulus experiments are artificial. In Greicius $et\ al.$ (2003), the functional connectivity in the resting brain is studied. In particular, the hypothesis of a default mode network is examined. Regions of interest, being deactivated during a cognitive task, are found to be interacting during periods of rest without particular stimulus. This finding is obtained, using an unconventional, but natural type of analysis. The average time series from one region is used as an explanatory variable in the analysis of the time variation in other regions of the brain. It is here of interest to try to develop models that can justify this type of data

analysis.

In a way, these developments are a consequence of the fact that fMRI is a more mature field now. Instead of seeking the locations of active brain regions, the focus is on the interaction between the active regions. This change of paradigm has consequences for the choice of appropriate method of analysis. Instead of looking for changes in level it seems to be more promising to study the covariation between the time series.

A first attempt to provide a modeling framework for experiments without repeated stimuli is outlined in the present paper. Such an experiment will be called a non-stimulus experiment. A simple simulated example of the experimental situation we have in mind is shown in Figure 1. Here, the MR signal intensity is observed in a two-dimensional slice of the 'brain' in the time interval (arbitrary units) [0,100]. In Figure 1, the development of the activity over time is shown, from $t = 5$ (upper left) to $t = 95$ (lower right) in jumps of 10 time units. Note that three regions of the brain simultaneously light up. The crucial point is that the random time points of activation is unknown to the experimenter. The aim of the analysis of the experiment is to find the areas of the brain that are simultaneously activated.
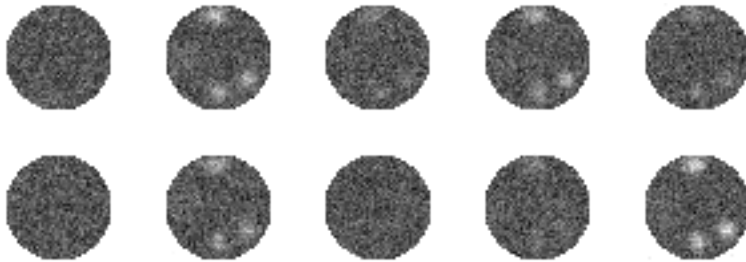
Figure 1: Development of the activity over time. From left to right and top to bottom: the activity at time $t = 5, 15, \ldots, 95$.

Our modeling approach is based on spatio-temporal point processes. Purely spatial processes have earlier been used in Taskinen (2001) and Hartvig (2002). Here, the spatial activation is modeled by Gaussian bell functions centered around the points from a spatial point process. As an example, the model studied in Hartvig (2002) is in its simplest form as follows

$$Z_{tx} = \sum_j h(x - x_j)\varphi_t + \sigma\varepsilon_{tx}$$

where Z_{tx} is the observed MR signal intensity at time t and voxel x, $\{x_j\}$ is a point process defined on the brain, h is a Gaussian density function with mean

0 and independent components, φ_t is a regression variable, containing information about the repeated stimulus experiment, and $\varepsilon_{tx} \sim N(0,1)$ represents the noise. For a non-stimulus experiment it seems obvious to replace φ_t with a stationary stochastic process $\{F_t\}$. One possibility is to consider stimuli at random time points such that

$$F_t = \sum_i g(t - t_i),$$

where $\{t_i\}$ is a Poisson point process on the real line and g is a hemodynamic response function.

The general model to be described in the present paper is specified, using marked point process theory. The classical repeated stimulus experiments can also be dealt with, using this modeling approach, but this is not our primary objective. Various methods of analyzing the model will be discussed, with increasing degree of computational complexity. Inference based on mean values, variances and covariances is relatively easy from a computationally point of view while likelihood or Bayesian methods are more demanding.

In Section 2, the suggested spatio-temporal model is described. Models for the temporal and spatial parts of the activation profile are discussed in Section 3 while Section 4 describes the underlying spatio-temporal point process. First and second order properties of Z_{tx} are expressed in terms of corresponding properties of the underlying spatio-temporal point process in Section 5 while specific point process models are discussed in Section 6. Section 7 describes statistical inference based on mean value and covariance relations as well as Bayesian analysis. A simulation study is presented in Section 8 while an analysis of real data can be found in Section 9. Future work and perspectives are outlined in Section 10. A summary of the main features of the new approach may be found in Section 11.

2 The spatio-temporal model

Our general model has the form

$$Z_{tx} = \mu_x + \sum_i f_{tx}(t_i, x_i; m_i) + \sigma_x \varepsilon_{tx}, \tag{1}$$

where μ_x is the baseline signal at voxel x and $\Psi = \{[t_i, x_i; m_i]\}$ is a marked spatio-temporal point process on $\mathbb{R} \times \mathcal{X}$ with marks in $\mathcal{M} \subseteq \mathbb{R}^d$. The observation period of the fMRI experiment is $[0, T]$. The set $\mathcal{X}$ is a bounded subset of $\mathbb{R}^2$ or $\mathbb{R}^3$, representing a two dimensional slice or a three dimensional volume of the brain. Furthermore, ε_{tx} is the error term with $\mathbb{E}\varepsilon_{tx} = 0$ and $\mathbb{V}\varepsilon_{tx} = 1$. It

is assumed that $\{\epsilon_{tx}\}$ are mutually independent. Various models for correlated noise are discussed in Section 10.

According to (1), the activation profile is described by the marked point process Ψ. Each marked point $[t_i, x_i; m_i]$ may be considered as a center of activation at location $x_i \in \mathcal{X}$. The center is activated at time t_i and its duration and extension are described by the mark $m_i \in \mathcal{M}$. In what follows, we let $m_i = (m_i^1, m_i^2) \in \mathcal{M}_1 \times \mathcal{M}_2$, $\mathcal{M}_i \subseteq \mathbb{R}^{d_i}$, say, $i = 1, 2$, where m_i^1 describes the duration and m_i^2 the spatial extension of the ith activation. If two regions $\mathcal{X}_0$ and $\mathcal{X}_1$ of the brain interact, it is expected that activations occur simultaneously in $\mathcal{X}_0$ and $\mathcal{X}_1$. Specific point process models with such long-distance dependencies will be described in Section 6. An illustration of the basic set-up may be found in Figure 2.
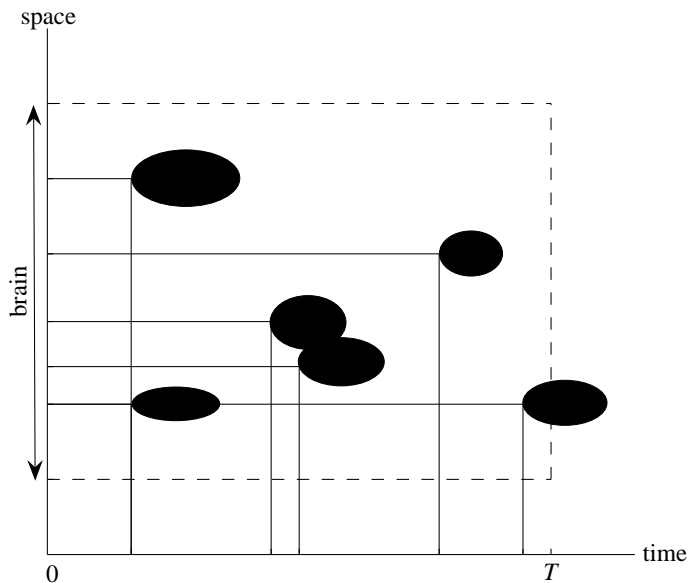
Figure 2: Illustration of the spatio-temporal point process model. Each ellipse illustrates the set of $(t, x) \in [0, T] \times \mathcal{X}$, affected by the activation in the leftmost point (t_i, x_i) of the ellipse. The mark m_i determines the shape and size of the ellipse. In the illustration, an example of simultaneous activation in two different places of the brain is seen, as well as activation of the same place of the brain at different time points.

In the analysis of fMRI data, spatial smoothing is often performed to reduce the noise of the data. The model (1) is closed under linear smoothing. Thus, suppose the data is smoothed by replacing Z_{tx} with $\tilde{Z}_{tx} = \sum_{z \in \mathcal{X}_x} \omega_{z-x} Z_{tz}$, where $\mathcal{X}_x$ is a neighborhood around x. We suppose that $\mathcal{X}_x = \mathcal{X}_0 + x$. Fur-

thermore, ω_y, $y \in \mathcal{X}_0$, satisfy $\omega_y \geq 0$ and $\sum_{y \in \mathcal{X}_0} \omega_y = 1$. If $\{Z_{tx}\}$ follow (1), then

$$\tilde{Z}_{tx} = \tilde{\mu}_x + \sum_i \tilde{f}_{tx}(t_i, x_i; m_i) + \tilde{\sigma}_x \tilde{\varepsilon}_{tx}$$

where

$$\tilde{\mu}_x = \sum_{u \in \mathcal{X}_0} \omega_u \mu_{x+u}, \ \tilde{f}_{tx} = \sum_{u \in \mathcal{X}_0} \omega_u f_{t,x+u}, \ \tilde{\sigma}_x^2 = \sum_{u \in \mathcal{X}_0} \omega_u^2 \sigma_{x+u}^2.$$

Our model is therefore closed under smoothing, except for the fact that smoothing introduces correlated errors.

3 Activation profile

Most current fMRI studies rely on the blood oxygenation level dependent (BOLD) effect (Ogawa *et al.* 1992) to detect changes in the MR signal intensity. Neural activity initiates a localized inflow of oxygenated blood to the active area, a *hemodynamic response*. This response is detectable in the MR signal due to different magnetic properties of oxygenated and deoxygenated blood. The biological processes behind the hemodynamic response are not known in detail, but the general structure of the temporal behavior has been described and reproduced in many studies. The hemodynamic response lags the neuronal activation with several seconds; it increases slowly to a peak value at about $4-7$ seconds after a neuronal impulse, and then returns to baseline again a few seconds after the neuronal impulse ceases. Often a late undershoot is reported as well, in the sense that when the signal drops after the peak value, it drops below baseline for a period before it returns to the baseline value.

Several different methods for modeling the hemodynamic response function have been introduced. Perhaps the most precise models are input-state-output models such as the Balloon model (see Buxton *et al.* (2004) and references therein for more details). These models are computationally very complex. The simpler models described below are considered to give a fairly good approximation to empirical studies of the HRF, see Friston *et al.* (1995) and Glover (1999). In these models, g is of the following form

$$g(u; m^1) = \int_0^l \kappa(u - v) dv, \tag{2}$$

where l is the temporal duration of the activation. The mark m^1 includes l and possibly other parameters describing the function κ. As discussed above, $\kappa(t) \approx 0$ for $t \leq 0$, κ increases in the interval from 0 to about $4 - 7$ seconds and then decreases to 0, possibly with a drop below 0 before returning to the value 0.

In the spatio-temporal point process model, each marked point $[t_i, x_i; m_i]$ represents an activation centered around x_i and starting at time t_i, with duration and extension specified by m_i^1 and m_i^2, respectively. Using the above established results, all voxels x around a voxel x_i activated at time t_i will contribute to the MR signal intensity with a hemodynamic response proportional to the one observed in x_i. We will here assume that the constant of proportionality depends on x and x_i only via $x - x_i$. The resulting model for the activation profile becomes

$$f_{tx}(u, y; m) = g(t - u; m^1)h(x - y; m^2). \tag{3}$$

In the fMRI literature, g is called the hemodynamic response function (HRF) and h is the spatial activation function (SAF). For a recent use of (3) in repeated stimulus experiments, see the seminal paper Hartvig (2002).

The modeling of the HRF and SAF is discussed below.

3.1 Temporal activation

3.1.1 HRF as an integral of Gaussian densities

Based on empirical studies, Friston *et al.* (1995) modeled the delay and dispersion of the hemodynamic response by a Gaussian density with mean 6 sec and variance 9 sec^2 as impulse response. In our formulation, this gives

$$\kappa(t) = \frac{1}{\sqrt{2\pi}3} \exp\left(-\frac{(t - 6)^2}{18}\right), \tag{4}$$

cf. Figure 3.
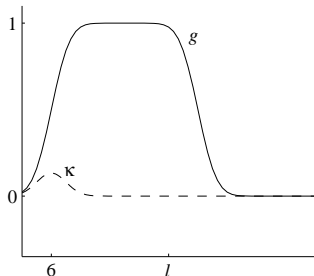
Figure 3: Gaussian response function κ (dashed) and the corresponding integrated response function g (solid).

This model assumes that the temporal activation pattern is the same for all activations during the experiment, which is a rather strong assumption. It

is not complicated to make (4) slightly more general, by allowing the mean and the variance of the Gaussian density to vary for each activation. That information would then be included in the mark m^1. The response function would though still not be able to account for a hemodynamic response with a late undershoot. A natural extension to improve this is to linearly combine (4) with its derivatives with respect to different parameters as in Friston *et al.* (1998).

3.1.2 HRF as an integral of gamma functions

Other empirical studies (Glover 1999) have shown that gamma functions may be more appropriate than Gaussian densities to capture the shape of the HRF. Glover uses the difference of two gamma functions, one to capture the main response and the other to capture the late undershoot. That is, the HRF is modeled by

$$\kappa(t) = \left[\left(\frac{t}{p_1}\right)^{a_1} \exp\left(-\frac{t - p_1}{b_1}\right) - c \left(\frac{t}{p_2}\right)^{a_2} \exp\left(-\frac{t - p_2}{b_2}\right) \right] \mathbb{1}\{t > 0\},$$

where t is the time in seconds and $p_j = a_j b_j$ is the time to the peak. In repeated stimulus experiments, $\kappa(t)$ is then convolved with the time course of the stimuli. This model can be made more flexible by expanding $\kappa(t)$ as a Taylor series and convolve the time course with $-\kappa(t) - t\partial\kappa(t)/\partial t$ instead (Worsley 2000).

This means that the mark m^1 is now given by $m^1 = \{a_1, a_2, b_1, b_2, c, l\}$, where l describes the duration of the activation. The number of unknown parameters in the mark can be reduced by using the results from Glover (1999). For auditory response, the parameters were fit to $a_1 = 6, a_2 = 12, b_1 = b_2 = 0.9$ and $c = 0.35$. Motor response gave the result $a_1 = 5, a_2 = 12, b_1 = 1.1, b_2 = 0.9$ and $c = 0.4$. An example is shown in Figure 4.
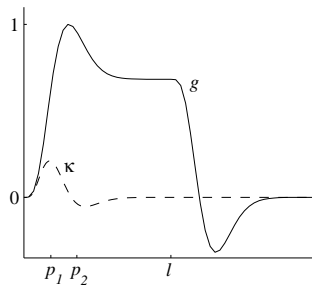

Figure 4: Gamma response function κ (dashed) and the corresponding integrated response function g (solid).

3.2   Spatial activation

The simplest model for the spatial activation is a symmetric Gaussian bell
function

$$h(y; m^2) = \theta_1 \exp\left(-\frac{\|y\|^2}{2\theta_2}\right), \tag{5}$$

where $m^2 = (\theta_1, \theta_2)$, $\theta_1, \theta_2 > 0$ and $\|\cdot\|$ is the Euclidean norm in $\mathcal{X}$.

This can be extended as follows. Let $m^2 = (\theta_1, \Theta_2)$ where $\theta_1 > 0$ and Θ_2
is a $p \times p$ positive definite matrix ($p = 2$ or 3). The spatial activation function
now becomes

$$h(y; m^2) = \theta_1 \exp\left(-\frac{1}{2}y^T \Theta_2^{-1} y\right), \tag{6}$$

where y is assumed to be a column vector and $(\cdot)^T$ stands for transpose, see
also Hartvig (2002).

4   The underlying spatio-temporal point process

The unmarked point process will be denoted by $\Phi = \{[t_i, x_i]\}$ and its intensity
measure by Λ. For $A \in \mathcal{B}(\mathbb{R} \times \mathcal{X})$, the Borel $\sigma-$algebra on $\mathbb{R} \times \mathcal{X}$, $\Phi(A)$ is the
number of unmarked points $[t_i, x_i]$ in A. Then,

$$\Lambda(A) = \mathbb{E}\Phi(A).$$

If $\Psi(A \times B)$ denotes the number of marked points $[t_i, x_i; m_i]$ with $[t_i, x_i] \in A$
and $m_i \in B$, $A \in \mathcal{B}(\mathbb{R} \times \mathcal{X})$ and $B \in \mathcal{B}(\mathcal{M})$, the intensity measure of the
marked point process is defined by

$$\Lambda_m(A \times B) = \mathbb{E}\Psi(A \times B).$$

Since $\Lambda_m(\cdot \times B) << \Lambda$, there exists for each $(u, y) \in \mathbb{R} \times \mathcal{X}$ a probability
distribution $P_{u,y}$ on $(\mathcal{M}, \mathcal{B}(\mathcal{M}))$ such that

$$\Lambda_m(A \times B) = \int_A P_{u,y}(B)\Lambda(du, dy),$$

see also (Stoyan *et al.* 1995, p. 108). Note that $P_{u,y}$ can be interpreted as the
distribution of the mark at (u, y).

Example 4.1 (The repeated stimulus experiment)**.** The standard repeated
stimulus experiment has earlier been described using this framework, cf. Hartvig
(2002). In such an experiment we have k activation periods with known start-
ing times t_i and known durations l_i, $i = 1, \ldots, k$, cf. Figure 5. The activation
centers in the brain is described in Hartvig (2002) by a marked spatial point

process $\{[x_j; m_j^2]\}$ where m_j^2 represents the spatial extension of the activation around x_j. The activation profile is specified as

$$\sum_{j=1}^{n} h(x - x_j; m_j^2)\varphi_t, \tag{7}$$

where φ_t is of the form

$$\varphi_t = \int_{-\infty}^{\infty} \pi_u \kappa(t - u)du,$$

$\pi_u = 1$ if $u \in \cup_{i=1}^{k}[t_i, t_i + l_i]$ and κ is the response function for an activation at time 0. The expression (7) can be rewritten as

$$\sum_{i=1}^{k} \sum_{j} f_{tx}(t_i, x_j; m_i^1, m_j^2),$$

where f_{tx} satisfies (3) with g of the form (2). It follows that the model can be described by a marked spatio-temporal process

$$\Psi = \{[t_i, x_j; (m_i^1, m_j^2)]\},$$

where t_i and $m_i^1 = l_i$ are known. Note that for this process the intensity measure Λ satisfies

$$\Lambda = \Lambda_1 \times \Lambda_2,$$

where Λ_1 and Λ_2 are measures on $(\mathbb{R}, \mathcal{B}(\mathbb{R}))$ and $(\mathcal{X}, \mathcal{B}(\mathcal{X}))$, respectively, and Λ_1 is a discrete measure with weight 1 in t_i, $i = 1, \dots, k$. $\qquad\square$
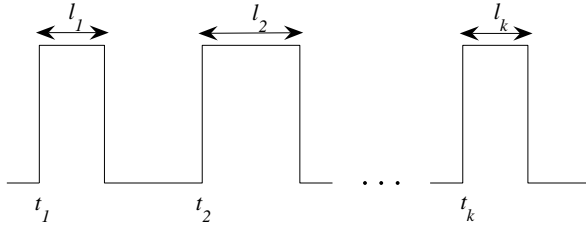

Figure 5: Repeated stimulus experiment.

Example 4.2 (The non-stimulus experiment)**.** During a non-stimulus experiment, the brain is not subjected to systematic stimuli but activated at random

time points unknown to the experimenter. We will formalize this in the following fashion. The marked point process Ψ is assumed to be time stationary in the sense that

$$\Psi_t = \{[t_i + t, x_i; m_i]\}$$

has the same distribution as Ψ for all $t \in \mathbb{R}$. As a consequence, the intensity measure Λ is of the form

$$\Lambda = c\nu^1 \times \Lambda_2,$$

where $c > 0$ and ν^1 is the Lebesgue measure on $\mathbb{R}$. Furthermore, time stationarity implies that the mark distribution $P_{u,y}$ does not depend on the time point u. $\qquad\square$

5 Moment relations

In this section, we derive moment relations for the observed MR signal Z_{tx}, under various assumptions on the spatio-temporal point process $\Psi = \{[t_i, x_i; m_i]\}$.

5.1 The mean value relation

Using the Campbell-Mecke theorem for marked point processes, we find

$$\mathbb{E}Z_{tx} = \mu_x + \int_{\mathbb{R}\times\mathcal{X}} \int_{\mathcal{M}} f_{tx}(u, y; m) P_{u,y}(dm) \Lambda(du, dy).$$

The mean value relation can be further simplified if Ψ is separable.

Definition 5.1 The spatio-temporal point process Ψ is called separable if the activation profile is on the product form (3),

$$\Lambda = \Lambda_1 \times \Lambda_2 \tag{8}$$

and

$$P_{u,y} = P_u^1 \times P_y^2. \tag{9}$$

Here, Λ_1 and Λ_2 are measures on $(\mathbb{R}, \mathcal{B}(\mathbb{R}))$ and $(\mathcal{X}, \mathcal{B}(\mathcal{X}))$ while P_u^1 and P_y^2 are probability measures on $(\mathcal{M}_1, \mathcal{B}(\mathcal{M}_1))$ and $(\mathcal{M}_2, \mathcal{B}(\mathcal{M}_2))$, respectively. $\square$

Note that (8) is satisfied for the repeated stimulus and non-stimulus experiments discussed in Example 4.1 and 4.2, respectively. The assumption (9) is trivially satisfied if the marks are nonrandom.

For a separable model, we have

$$\mathbb{E}Z_{tx} = \mu_x + \alpha_t \beta_x, \tag{10}$$

11

where

$$\alpha_t = \int_{\mathbb{R}} \int_{\mathcal{M}_1} g(t - u; m^1) P_u^1(dm^1) \Lambda_1(du)$$

and

$$\beta_x = \int_{\mathcal{X}} \int_{\mathcal{M}_2} h(x - y; m^2) P_y^2(dm^2) \Lambda_2(dy).$$

The parameters α_t can be further simplified for repeated stimulus and non-stimulus experiments, respectively.

Example 4.1 (continued). The measure Λ_1 is here a discrete measure with weight 1 in $t_i, i = 1, \ldots, k$, and

$$\alpha_t = \sum_{i=1}^{k} \int_{\mathcal{M}_1} g(t - t_i; m^1) P_{t_i}^1(dm^1). \tag{11}$$

In particular, if $P_{t_i}^1$ is concentrated in l_i, the known duration of the ith activation, then

$$\alpha_t = \sum_{i=1}^{k} g(t - t_i; m_i^1) \tag{12}$$

is known. The mean value specification (10) is a linear regression. $\qquad\square$

Example 4.2 (continued). Since $\Lambda_1 = c\nu^1$ and P_u^1 does not depend on $u \in \mathbb{R}$, we have

$$
\begin{aligned}
\alpha_t &= c \int_{\mathbb{R}} \int_{\mathcal{M}_1} g(t - u; m^1) P_u^1(dm^1) du \\
&= c \int_{\mathcal{M}_1} \int_{\mathbb{R}} g(t - u; m^1) du P^1(dm^1) \\
&= c\mathbb{E}\alpha_1(M^1),
\end{aligned}
$$

where

$$\alpha_1(m^1) = \int_{\mathbb{R}} g(v; m^1) dv$$

and M^1 is a random mark, distributed according to P^1. Accordingly, the parameter α_t does not depend on t and the same is true for $\mathbb{E}Z_{tx}$. $\qquad\square$

5.2 The covariance structure

In contrast to first-order properties, the covariance structure of Z_{tx} depends on the specific choice of point process model. The covariance can be expressed in terms of the so-called second-order factorial moment measure, see Stoyan *et al* (1995, p. 111 and onwards).

Let us here study the case of a marked point process $\Psi = \{[t_i, x_i; m_i]\}$ with conditional independent marks, such that conditionally on $\Phi = \{[t_i, x_i]\}$, $\{m_i\}$ are independent and $m_i \sim P_{t_i, x_i}$. Then,

$$\mathbb{E}\Big(\sum_{i,i'} f_{tx}(t_i, x_i; m_i) f_{t'x'}(t_{i'}, x_{i'}; m_{i'})\Big)$$

$$= \int_{\mathbb{R} \times \mathcal{X}} \int_{\mathcal{M}} f_{tx}(u, y; m) f_{t'x'}(u, y; m) P_{u,y}(dm) \ \Lambda(du, dy)$$

$$+ \int_{\mathbb{R} \times \mathcal{X}} \int_{\mathbb{R} \times \mathcal{X}} \int_{\mathcal{M}} \int_{\mathcal{M}} f_{tx}(u, y; m) f_{t'x'}(u', y'; m') P_{u,y}(dm) P_{u',y'}(dm')$$

$$\times \alpha^{(2)}(du, dy, du', dy'),$$

where $\alpha^{(2)}$ is the second-order factorial moment measure for Φ, which is defined for $A, A' \in \mathcal{B}(\mathbb{R} \times \mathcal{X})$ by

$$\alpha^{(2)}(A \times A') = \mathbb{E} \sum_{i \neq i'} \mathbb{1}\{[t_i, x_i] \in A, [t_{i'}, x_{i'}] \in A'\}.$$

It follows that

$$\mathrm{Cov}(Z_{tx}, Z_{t',x'})$$

$$= \int_{\mathbb{R} \times \mathcal{X}} \int_{\mathcal{M}} f_{tx}(u, y; m) f_{t'x'}(u, y; m) P_{u,y}(dm) \ \Lambda(du, dy)$$

$$+ \int_{\mathbb{R} \times \mathcal{X}} \int_{\mathbb{R} \times \mathcal{X}} \int_{\mathcal{M}} \int_{\mathcal{M}} f_{tx}(u, y; m) f_{t',x'}(u', y'; m') P_{u,y}(dm) P_{u',y'}(dm')$$

$$\times [\alpha^{(2)}(du, dy, du', dy') - \Lambda(du, dy)\Lambda(du', dy')]$$

$$+ \mathbb{1}\{(t, x) = (t', x')\}\sigma_x^2. \tag{13}$$

The second-order factorial moment measure $\alpha^{(2)}$ is equal to $\Lambda \times \Lambda$ if Φ is a Poisson point process, cf. Stoyan *et al* (1995, p. 44). If

$$\alpha^{(2)}(du, dy, du', dy') - \Lambda(du, dy)\Lambda(du', dy') > 0,$$

then pairs of activations are more likely to occur jointly at (u, y) and (u', y') than for a Poisson point process with intensity measure Λ.

6 Specific point process models

In this section, we give two examples of spatio-temporal point process models that can exhibit the desired long-distance dependence. Under such a model,

brain regions far apart may interact in the sense that if one of the regions is activated at time t then it is likely that the other regions are also activated at time t.

Example 6.1 (Independent spatial and temporal point patterns). Suppose that $\Psi = \{[t_i, x_j; m_i^1, m_j^2]\}$ where $\Psi_1 = \{[t_i; m_i^1]\}$ and $\Psi_2 = \{[x_j; m_j^2]\}$ are independent. This model is separable. An example with Ψ_1 and Ψ_2 Poisson is shown in Figure 6, left. We have

$$Z_{tx} = \mu_x + A_t B_x + \sigma_x \varepsilon_{tx},$$

where

$$A_t = \sum_i g(t - t_i; m_i^1) \text{ and } B_x = \sum_j h(x - x_j; m_j^2) \qquad (14)$$

are independent. The covariance is of the form

$$\mathrm{Cov}(Z_{tx}, Z_{t'x'}) = \mathrm{Cov}(A_t, A_{t'}) \, \mathrm{Cov}(B_x, B_{x'}) + \mathrm{Cov}(A_t, A_{t'}) \beta_x \beta_{x'}$$
$$+ \alpha_t \alpha_{t'} \, \mathrm{Cov}(B_x, B_{x'}) + \mathbb{1}\{(t, x) = (t', x')\} \sigma_x^2.$$

For a repeated stimulus experiment, A_t is deterministic and the expression for the covariance reduces to

$$\mathrm{Cov}(Z_{tx}, Z_{t'x'}) = \alpha_t \alpha_{t'} \, \mathrm{Cov}(B_x, B_{x'}) + \mathbb{1}\{(t, x) = (t', x')\} \sigma_x^2,$$

where α_t takes the form (11) or (12), depending on the specific assumption on the HRF. A model of this type has already been considered in Hartvig (2002).

In a non-stimulus experiment, Ψ is time stationary and $\mathrm{Cov}(A_t, A_{t'})$ only depends on $|t - t'|$. In particular, if the temporal process $\{t_i\}$ is Poisson and conditionally on $\{t_i\}$, $\{m_i^1\}$ are independent and $m_i^1 \sim P^1$, we have

$$\mathrm{Cov}(A_t, A_{t'}) = \int_{\mathbb{R}} \int_{\mathcal{M}_1} g(t - u; m^1) g(t' - u; m^1) P^1(dm^1) \Lambda_1(du) = \rho_{t,t'},$$

say. Since $\Lambda_1(du) = c\,du$, we get

$$\rho_{t,t'} = c \int_{\mathbb{R}} \int_{\mathcal{M}_1} g(t - u; m^1) g(t' - u; m^1) P^1(dm^1) du$$
$$= c \int_{\mathcal{M}_1} \int_{-\infty}^{\infty} g(v; m^1) g(v + |t' - t|; m^1) dv P^1(dm^1)$$
$$= c \mathbb{E}\alpha_2(|t' - t|; M^1),$$

say, where

$$\alpha_2(t; m^1) = \int_{-\infty}^{\infty} g(v; m^1) g(v + t; m^1) dv$$

14

and M^1 is a random mark distributed according to P^1. If the spatial process is Poisson with conditionally independent marking

$$\text{Cov}(B_x, B_{x'}) = \int_{\mathcal{X}} \int_{\mathcal{M}_2} h(x-y; m^2)h(x'-y; m^2)P_y^2(dm^2)\Lambda_2(dy) = \tau_{x,x'},$$

say. The parameter $\tau_{x,x'}$ will be small if Λ_2 is concentrated around x and x' but the distance between x and x' is large. If both processes are Poisson with conditionally independent marking, we thus have

$$\text{Cov}(Z_{tx}, Z_{t'x'}) = \rho_{t,t'}\tau_{x,x'} + \rho_{t,t'}\beta_x\beta_{x'} + \alpha_t\alpha_{t'}\tau_{x,x'} + \mathbb{1}\{(t,x) = (t',x')\}\sigma_x^2. \tag{15}$$

More generally, if both processes $\{t_i\}$ and $\{x_j\}$ have conditionally independent marking, $\{t_i\}$ is Poisson and $\{x_j\}$ is a general point process with second-order factorial moment measure $\alpha^{(2)}$, then

$$\begin{aligned} \text{Cov}(Z_{tx}, Z_{t'x'}) &= [\rho_{t,t'} + \alpha_t\alpha_{t'}][\tau_{x,x'} + \delta_{x,x'}] \\ &\quad + \rho_{t,t'}\beta_x\beta_{x'} + \mathbb{1}\{(t,x) = (t',x')\}\sigma_x^2, \end{aligned} \tag{16}$$

where

$$\delta_{x,x'} = \int_{\mathcal{X}} \int_{\mathcal{X}} \int_{\mathcal{M}_2} \int_{\mathcal{M}_2} h(x-y; m^2)h(x'-y'; m^{2'})P_y^2(dm^2)P_{y'}^2(dm^{2'})$$

$$\times [\alpha^{(2)}(dy, dy') - \Lambda_2(dy)\Lambda_2(dy')].$$

Note that $\delta_{x,x'} = 0$ if $\{x_j\}$ is Poisson. $\qquad\square$

Example 6.2 (Conditional independent spatial processes). The spatio-temporal process is given by $\Psi = \{[t_i, x_{ij}; m_i^1, m_{ij}^2]\}$. Conditionally on the temporal process $\Psi_1 = \{[t_i; m_i^1]\}$, the spatial processes $\Psi_{2i} = \{[x_{ij}; m_{ij}^2]\}$ are independent and identically distributed with second-order factorial moment measure $\alpha^{(2)}$. It is not difficult to show that if (3) is satisfied, then Ψ is separable.

Under this model, the covariance is of the form

$$\begin{aligned} \text{Cov}(Z_{tx}, Z_{t'x'}) &= \text{Cov}(A_t, A_{t'})\beta_x\beta_{x'} + \rho_{t,t'}\text{Cov}(B_x, B_{x'}) \\ &\quad + \mathbb{1}\{(t,x) = (t',x')\}\sigma_x^2, \end{aligned}$$

with the notation of the previous example. For a repeated stimulus experiment, cf. Example 4.1, A_t is deterministic and the expression for the covariance reduces to

$$\text{Cov}(Z_{tx}, Z_{t',x'}) = \rho_{t,t'}\text{Cov}(B_x, B_{x'}) + \mathbb{1}\{(t,x) = (t',x')\}\sigma_x^2.$$

If instead the temporal process is Poisson, we have an example of a non-stimulus experiment, cf. Example 4.2, and the covariance is of the form

$$\text{Cov}(Z_{tx}, Z_{t'x'}) = \rho_{t,t'}[\tau_{x,x'} + \delta_{x,x'} + \beta_x\beta_{x'}] + \mathbb{1}\{(t,x) = (t',x')\}\sigma_x^2, \quad (17)$$

again with the notation of the previous example. An example with Ψ_1 and Ψ_2 Poisson is shown in Figure 6, right. $\qquad\qquad\square$
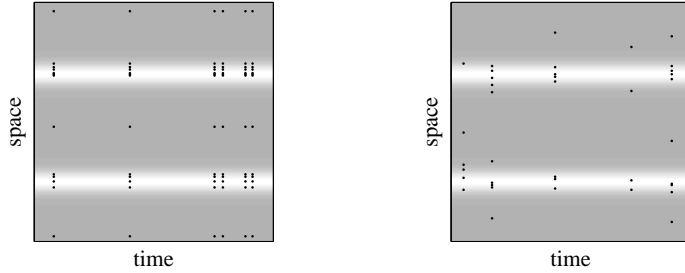
Figure 6: Independent spatial and temporal Poisson processes (left) and conditionally independent Poisson processes (right). The associated intensity functions are shown in gray scale.

7   Statistical inference

In this section, we discuss statistical inference based on moment relations. We also briefly touch upon Bayesian inference.

7.1   Inference based on the mean value relation

In this subsection, we will discuss within the framework of a separable model, the estimation of the intensity measure Λ_2 of the spatial point process, using the general mean value relation (10). We will assume that the marks are identical for all points in which case

$$\mathbb{E}Z_{tx} = \mu_x + \alpha_t\beta_x,$$

where

$$\alpha_t = \int_{\mathbb{R}} g(t - s; m^1)\Lambda_1(ds)$$

and

$$\beta_x = \int_{\mathcal{X}} h(x - y; m^2)\Lambda_2(dy).$$

16

In what follows, we let $\widetilde{\alpha}_t = \alpha_t$ in a repeated stimulus experiment (see (12)) while $\widetilde{\alpha}_t = 1$ in a non-stimulus experiment. Note that for fixed m^1 the parameters $\widetilde{\alpha}_t$ are known. Likewise, we let $\widetilde{\Lambda}_2 = \Lambda_2$ in a repeated stimulus experiment and $\widetilde{\Lambda}_2 = c\alpha_1(m^1)\Lambda_2$ in a non-stimulus experiment where

$$\alpha_1(m^1) = \int_{\mathbb{R}} g(u; m^1)du.$$

The method to be described can be applied if the baseline intensity μ_x can be regarded as known. The baseline intensity can vary by a factor of 2-3 across the brain, due to variations in the brain tissue as well as variations in the scanner. The baseline μ_x is well determined from data in repeated stimulus experiments, otherwise additional data is needed.

If μ_x can be regarded as known, we can let $\mu_x = 0$. The mean value relation can then be written as

$$\mathbb{E}Z_{tx} = \widetilde{\alpha}_t\widetilde{\beta}_x,$$

where

$$\widetilde{\beta}_x = \int_{\mathcal{X}} h(x - y; m^2)\widetilde{\Lambda}_2(dy).$$

We will consider the estimation of Λ_2 (or equivalently $\widetilde{\Lambda}_2$) under the assumption that Λ_2 is a discrete measure concentrated in $y_j, j = 1, \ldots, N$, with masses $\lambda_2(y_j) = \Lambda_2(\{y_j\})$, $j = 1, \ldots, N$. Here, N may be chosen as the number of voxels. Let us suppose that we have discretely observed data in time with spacing Δ

$$\{Z_{i\Delta,x} : i = i_0 + 1, \ldots, i_0 + n, x \in \mathcal{X}\},$$

where all time points are free of edge effects. A simple estimation procedure is to estimate $\widetilde{\beta}_x$ by the regression estimate

$$\widetilde{Z}_x = \sum_{i=1}^{n} \widetilde{\alpha}_{(i_0+i)\Delta} Z_{(i_0+i)\Delta,x} / \sum_{i=1}^{n} \widetilde{\alpha}^2_{(i_0+i)\Delta}$$

and for each m^1 and m^2 minimize

$$\sum_{i=1}^{N} \left[\widetilde{Z}_{y_i} - \sum_{j=1}^{N} h(y_i - y_j; m^2)\widetilde{\lambda}_2(y_j) \right]^2 \tag{18}$$

with respect to $\{\widetilde{\lambda}_2(y_j)\}$, subject to the condition $\widetilde{\lambda}_2(y_j) \geq 0$ for all j. Note that in a non-stimulus experiment, Λ_2 and c cannot be separated, using this estimation procedure.

17

The variance of $\widetilde{Z}_x$ may, however, depend on x. As an example, let us consider a repeated stimulus experiment with Poisson distributed activation centers as described in Example 6.1. Then,

$$\mathbb{V}\widetilde{Z}_x = \tau_{x,x} + \frac{1}{\sum_1^n \alpha_{(i_0+i)\Delta}^2}\sigma_x^2.$$

An unbiased estimate of σ_x^2 is

$$\hat{\sigma}_x^2 = \frac{1}{n-1}\sum_{i=1}^n (Z_{(i_0+i)\Delta,x} - \alpha_{(i_0+i)\Delta}\widetilde{Z}_x)^2.$$

Furthermore, a discrete version of $\tau_{x,x}$ is

$$\tau_{x,x} = \sum_{j=1}^N h(x-y_j;m^2)^2\lambda_2(y_j).$$

The unweighted sum of squares may then be replaced by

$$\sum_{i=1}^N \left[\widetilde{Z}_{y_i} - \sum_{j=1}^N h(y_i - y_j;m^2)\lambda_2(y_j)\right]^2 /\mathbb{V}\widetilde{Z}_{y_i},$$

where we insert the derived form of $\mathbb{V}\widetilde{Z}_{y_i}$ and the estimate $\hat{\sigma}_{y_i}^2$. This sum of squares should be minimized with respect to λ_2 for fixed m^1 and m^2.

As another example, let us consider a non-stimulus experiment with independent temporal and spatial Poisson point processes. Then,

$$\widetilde{Z}_x = \bar{Z}_{\cdot x} = \frac{1}{n}\sum_{i=1}^n Z_{(i_0+i)\Delta,x}$$

and, using (15), we find

$$\mathbb{V}\bar{Z}_{\cdot x} = \frac{c}{n^2}\left[n\alpha_2(0;m^1) + 2\sum_{i=1}^{n-1}(n-i)\alpha_2(i\Delta;m^1)\right]\left[\tau_{x,x} + \beta_x^2\right]$$
$$+ c^2\alpha_1(m^1)^2\tau_{x,x} + \frac{1}{n}\sigma_x^2.$$

The empirical variance

$$\hat{\sigma}_{x,x} = \frac{1}{n-1}\sum_{i=1}^n (Z_{(i_0+i)\Delta,x} - \bar{Z}_{\cdot x})^2$$

18

can be used to estimate σ_x^2 but it is important to correct for bias in this estimate caused by correlations inside the time series. We will now derive the bias of the estimate.

Generally, if $\mathrm{Cov}(Z_{tx}, Z_{tx'})$ only depend on t and t' via $|t - t'|$,

$$\mathrm{Cov}(Z_{tx}, Z_{t',x'}) = \sigma_{x,x'}(|t - t'|),$$

say, then the estimate

$$\hat{\sigma}_{x,x'} = \frac{1}{n-1} \sum_{i=1}^{n} (Z_{(i_0+i)\Delta,x} - \bar{Z}_{\cdot x})(Z_{(i_0+i)\Delta,x'} - \bar{Z}_{\cdot x'}), \tag{19}$$

is a biased estimate of $\sigma_{x,x'} = \sigma_{x,x'}(0)$. We thus have

$$\mathbb{E}(\hat{\sigma}_{x,x'}) = \sigma_{x,x'} - \frac{2}{n(n-1)} \sum_{i=1}^{n-1} (n-i)\sigma_{x,x'}(i\Delta). \tag{20}$$

Using (15), (19) and (20), we find that

$$\mathbb{E}(\hat{\sigma}_{x,x}) = c\left[\alpha_2(0; m^1) - \frac{2}{n(n-1)} \sum_{i=1}^{n-1} (n-i)\alpha_2(i\Delta; m^1)\right] \left[\tau_{x,x} + \beta_x^2\right] + \sigma_x^2.$$

The variance of $\bar{Z}_{\cdot x}$ can therefore be written as

$$\mathbb{V}\bar{Z}_{\cdot x} = \frac{1}{n}\mathbb{E}(\hat{\sigma}_{x,x}) + c^2\alpha_1(m^1)^2\tau_{x,x} + \frac{2c}{n(n-1)} \sum_{i=1}^{n-1} (n-i)\alpha_2(i\Delta; m^1)[\tau_{x,x} + \beta_x^2].$$

The unweighted sum of squares may be replaced by

$$\sum_{i=1}^{N} \left[\bar{Z}_{\cdot y_i} - c\alpha_1(m^1) \sum_{j=1}^{N} h(y_i - y_j; m^2)\lambda_2(y_j)\right]^2 \bigg/ \mathbb{V}\bar{Z}_{\cdot y_i}$$

and minimized with respect to $\{\lambda_2(y_j)\}$ for each fixed c, m^1 and m^2.

7.2 Inference based on covariances

The method described in the previous section is simple but requires, for a non-stimulus experiment, that μ_x is known from external sources. If this is not feasible, one may try to get information about the intensity measure Λ_2 of the spatial point process from $\mathrm{Cov}(Z_{tx}, Z_{t',x'})$ instead. The covariances do not depend on the μ_xs.

This approach depends on a specific point process model. As an example, let us consider the model for a non-stimulus experiment with both temporal

and spatial processes Poisson. Irrespectively of whether the processes are independent or conditionally independent (Example 6.1 or 6.2), the mean value of the empirical covariance estimate (19) can be approximated for x, x' with large mutual distance by

$$\mathbb{E}(\hat{\sigma}_{x,x'}) \approx c\gamma(m^1)\beta_x\beta_{x'},$$

where

$$\gamma(m^1) = \alpha_2(0; m^1) - \frac{2}{n(n-1)} \sum_{i=1}^{n-1}(n-i)\alpha_2(i\Delta; m^1),$$

cf. (15), (17), (19) and (20). Assume that an activation center $\mathcal{X}_0 \subset \mathcal{X}$ with N_0 points is known. Then, for x' with large mutual distance from all points $x \in \mathcal{X}_0$,

$$\mathbb{E}\Big(\frac{1}{N_0} \sum_{x \in \mathcal{X}_0} \hat{\sigma}_{x,x'}\Big) \approx c\gamma(m^1)\bar{\beta}. \sum_{i=1}^{N} h(x' - x_i; m^2)\lambda_2(x_i), \qquad (21)$$

where

$$\bar{\beta}. = \frac{1}{N_0} \sum_{x \in \mathcal{X}_0} \beta_x.$$

This expression is linear in λ_2 if we regard $\bar{\beta}.$ as an unknown constant. We can thus use least squares methods to estimate $\lambda_2(x)$ for $x \in \mathcal{X} \setminus \mathcal{X}_0$ up to a constant, as in the previous section.

Another relevant question is what kind of information about the model parameters can be gained from the covariances under a less specified model, for instance if we relax the assumption that the spatial point process is Poisson. Let us concentrate on the conditional independent processes, presented in Example 6.2. We consider a non-stimulus experiment with a Poisson process as temporal process. Then, cf. (17),

$$\begin{aligned}
\mathrm{Cov}(Z_{tx}, Z_{t',x'}) &= c\alpha_2(|t' - t|; m^1) \\
&\times \Big[\tau_{x,x'} + \int_{\mathcal{X}} \int_{\mathcal{X}} h(x - y; m^2)h(x' - y'; m^2)\alpha^{(2)}(dy, dy')\Big] \\
&+ \mathbb{1}\{(t, x) = (t', x')\}\sigma_x^2.
\end{aligned}$$

In particular, for x, x' with large mutual distance

$$\mathrm{Cov}(Z_{tx}, Z_{t',x'}) \approx c\alpha_2(0; m^1) \int_{\mathcal{X}} \int_{\mathcal{X}} h(x - y; m^2)h(x' - y'; m^2)\alpha^{(2)}(dy, dy').$$

The slope of the regression of $Z_{t,x'}$ on Z_{tx},

$$\mathrm{Cov}(Z_{tx}, Z_{tx'})/\mathbb{V}Z_{tx},$$

is thus for fixed x and varying x' proportional to

$$\int_{\mathcal{X}} \int_{\mathcal{X}} h(x - y; m^2) h(x' - y'; m^2) \alpha^{(2)}(dy, dy').$$

If $h(u; m^2)$ is concentrated around $u = 0$, a plot of the slopes will reveal $x' \in \mathcal{X}$ for which $\alpha^{(2)}(dx, dx')$ is large. Recall that $\alpha^{(2)}(dx, dx')$ can be interpreted as the probability of having simultaneously an activation at x and x'.

In Greicius *et al.* (2003), the average time series from one brain region is used as explanatory variable in the analysis of the time variation in other regions of the brain. Under the model specified above, Greicius' analysis leads to a study of the second-order factorial moment measure of the spatial point process.

7.3   Bayesian inference

In this subsection, we will briefly discuss Bayesian inference. A more complete treatment of this approach is planned to appear elsewhere. As earlier, μ_x requires a special treatment. When considering Bayesian methods we may simply replace Z_{tx} by $Z_{tx} - \bar{Z}_{\cdot x}$ and f_{tx} by $f_{tx} - \bar{f}_{\cdot x}$. The new data have $\mu_x = 0$ and the same correlation structure as the original data if T is large. For brevity, we write $Z = \{Z_{tx}\}$.

7.3.1   Prior distributions

We concentrate on the case where $m_i = m$ and $\sigma_x = \sigma$ are known. We then need to specify a prior density of the point process Φ and its parameters. We assume that the intensity function of Φ is of the following form

$$\lambda(t, x) = \sum_{l=1}^{k} \lambda_l \mathbf{1}\{x \in \mathcal{X}_l\},$$

where the sets $\mathcal{X}_l \subseteq \mathcal{X}$ are disjoint. Their union may be the whole brain $\mathcal{X}$ but need not be. The sets $\mathcal{X}_l$ should be specified by the experimenter while the parameters λ_l are unknown.

It turns out to be a good idea to transform the parameters. Thus, we let $c = \sum \lambda_l |\mathcal{X}_l|$ and $\pi_l = \lambda_l |\mathcal{X}_l| / \sum \lambda_l |\mathcal{X}_l|$. Note that the π_l's satisfy

$$\pi_l \geq 0, \ \sum_{l=1}^{k} \pi_l = 1.$$

The new parameters have nice interpretations. Thus,

$$
\begin{aligned}
c &= \frac{1}{T} \int_{[0,T] \times \mathcal{X}} \lambda(t,x) dt dx \\
&= \frac{1}{T} \mathbb{E} \Phi([0,T] \times \mathcal{X})
\end{aligned}
$$

is the expected number of activations per time unit while

$$
\begin{aligned}
\pi_l &= \int_{[0,T] \times \mathcal{X}_l} \lambda(t,x) dt dx \Big/ \int_{[0,T] \times \mathcal{X}} \lambda(t,x) dt dx \\
&= \mathbb{E} \Phi([0,T] \times \mathcal{X}_l) / \mathbb{E} \Phi([0,T] \times \mathcal{X})
\end{aligned}
$$

is the expected fraction of all activations that occur in $\mathcal{X}_l$. Note that

$$
\lambda(t,x) = c\lambda_2(x), \tag{22}
$$

where

$$
\lambda_2(x) = \sum_{l=1}^{k} \pi_l \frac{\mathbf{1}\{x \in \mathcal{X}_l\}}{|\mathcal{X}_l|}, \tag{23}
$$

satisfies

$$
\int_{\mathcal{X}} \lambda_2(x) dx = 1.
$$

The prior distribution of Φ will be chosen as Poisson with intensity function λ. Note that there is no interaction between points in the prior distribution. Interaction found in the posterior distribution of the point process will therefore be 'caused' by the data z. We consider the restriction

$$
\Phi_0 = \Phi \cap ([T_{0-}, T_{0+}] \times \mathcal{X})
$$

of Φ to a time interval $[T_{0-}, T_{0+}]$ containing $[0,T]$. The interval $[T_{0-}, T_{0+}]$ is chosen such that it is very unlikely that a point from $\Phi \backslash \Phi_0$ will affect an MR signal observed in $[0,T]$. Using (22) and (23), the density of Φ_0 with respect to the distribution ν of a unit rate Poisson process on $[T_{0-}, T_{0+}] \times \mathcal{X}$ becomes

$$
\begin{aligned}
p(\phi_0 | c, \pi) &= \exp(-\int_{[T_{0-}, T_{0+}] \times \mathcal{X}} [\lambda(t,x) - 1] dt dx) \prod_{[u,y] \in \phi_0} \lambda(u,y) \\
&= \exp(-(T_{0+} - T_{0-})(c - |\mathcal{X}|)) c^{n(\phi_0)} \prod_l (\frac{\pi_l}{|\mathcal{X}_l|})^{n_l(\phi_0)},
\end{aligned}
$$

where $n(\phi_0)$ is the number of points in ϕ_0 and $n_l(\phi_0)$ is the number of these points falling in $\mathcal{X}_l$.

We will use non-informative priors for c and $\pi = (\pi_1, \ldots, \pi_k)$. The prior density of c will be specified as

$$p(c) = \frac{1}{c_{\max}} \mathbf{1}\{c < c_{\max}\},$$

where $c_{\max}$ is a large known constant while the prior density of π is

$$p(\pi) = \frac{1}{\text{vol}(D)} \mathbf{1}\{\pi \in D\},$$

where

$$D = \{\pi : \pi_l > 0, \sum \pi_l = 1\}.$$

7.3.2 Posterior simulation

The complete posterior density is

$$p_{m,\sigma^2}(c, \pi, \phi_0 | z) \propto p(c)p(\pi)p(\phi_0 | c, \pi)p_{m,\sigma^2}(z | \phi_0), \tag{24}$$

since the conditional density of z given c, π, ϕ_0

$$p_{m,\sigma^2}(z | \phi_0) = [2\pi\sigma^2]^{-NT/2} \exp(-\frac{1}{2\sigma^2} \|z - f(\phi_0; m)\|^2).$$

only depends on ϕ_0. Here,

$$\|z - f(\phi_0; m)\|^2 = \sum_{t,x} \left(z_{tx} - \sum_{[t_i, x_i] \in \phi_0} f_{tx}(t_i, x_i; m) \right)^2$$

For simulation from the posterior density we use a fixed scan Metropolis within Gibbs algorithm where in each scan c, π and ϕ_0 are updated in turn. The full conditional for c is a Gamma distribution

$$c | \pi, \phi_0, z \sim \Gamma(n(\phi_0) + 1, T_{0+} - T_{0-}), \tag{25}$$

with the constraint that $c < c_{\max}$. We use (25) as proposal where ϕ_0 is the current state, and sample from $\Gamma(n(\phi_0) + 1, T_{0+} - T_{0-})$ until the constraint is satisfied.

The density of the full conditional distribution of π takes the form

$$\begin{aligned} p(\pi | c, \phi_0, z) &\propto p(\pi)p(\phi_0 | c, \pi) \\ &\propto \prod \pi_l^{n_l(\phi_0)} \end{aligned}$$

with the constraint $\pi \in D$. For $k = 1$, this step can be omitted as $D = \{1\}$. For $k = 2$,

$$\pi | c, \phi_0, z \sim \text{Beta}(n_1(\phi_0) + 1, n_2(\phi_0) + 1).$$

while for $k > 2$ we have

$$\pi|c, \phi_0, z \sim \text{ Dirichlet}\big(n_1(\phi_0) + 1, n_2(\phi_0) + 1, \ldots, n_k(\phi_0) + 1\big).$$

We sample a π from the appropriate distribution, using the current value of ϕ_0.

The last step is to simulate from

$$p(\phi_0|c, \pi, z) \propto c^{n(\phi_0)} \prod_l \pi_l^{n_l(\phi_0)} \exp(-\frac{1}{2\sigma^2}\|z - f(\phi_0; m)\|^2).$$

The point process is simulated using a birth, death, and move algorithm as described in Chapter 7 in Møller and Waagepetersen (2004). The starting value of the simulation is a Poisson process. In each iteration we then propose one of the following steps: deleting a uniformly chosen point from the current point pattern, moving a uniformly chosen point in the current point pattern to a new random location (in time and space), or adding a new point in a random location. The different proposals are selected with equal probability. We use the current values of c and π to calculate the acceptance ratio for the suggested change in the point pattern.

8 A simulation study

We have simulated data from the model in (1) with independent spatial and temporal Poisson point patterns as in Example 6.1. The object of the simulation study was the analysis of a non-stimulus experiment. Thus, we gave the temporal intensity function a constant value, $\lambda_1(t) = c$ for all $t \in [0, 100]$, while the spatial activation pattern comprised activated areas of various sizes, shapes and peak intensity. The HRF was given by an integral (sum) of Gaussian densities as in Section 3.1.1 with $m^1 = l = 5$ and the spatial activation was modeled by a symmetric Gaussian bell function as in Section 3.2 with $m^2 = (\theta_1, \theta_2) = (4, 4)$. Further, the errors were standard Gaussian distributed, $\varepsilon_{tx} \sim N(0, 1)$, and we set σ_x^2 to be equal to 40% of the baseline signal. The standard deviation σ_x is roughly three times larger than the maximum intensity of an activation center.

The activation pattern is shown in Figure 7, with the realization of the temporal activity left and the arranged spatial activity right. Two time series from the simulation are shown in Figure 8, one is from an activated area and one from an area with no activation. The activation pattern in the former clearly follows the temporal activation pattern shown in Figure 7 (left). The development of the activation over time has also been shown in Figure 1.

We have estimated the spatial intensity function λ_2, using the three different methods outlined in Section 7. In Section 8.1, we used the method based
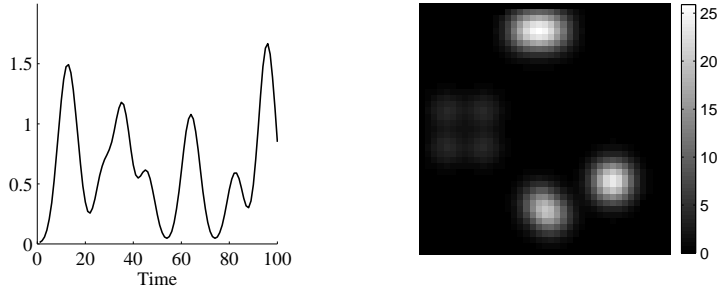
Figure 7: The realization of the temporal activity used in the simulation (left) and the spatial activity (right). The HRF was modeled by a sum of Gaussian functions with mark $m^1 = 5$ and the SAF was modeled by a Gaussian bell function with $m^2 = (4, 4)$. See the main text for more details.
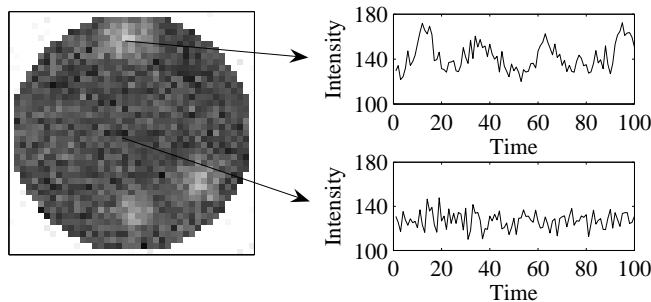

Figure 8: Illustration of time series data from the simulation. Left: simulated data at time $t = 20$. Right: time series of respectively an active (top) and a nonactive (bottom) voxel.

on the general mean value relation as described in Section 7.1. In Section 8.2, we assumed one of the activated areas, $\mathcal{X}_0 \subset \mathcal{X}$, to be known and we searched for other areas in $\mathcal{X}$, functionally connected to $\mathcal{X}_0$. That is, we estimated λ_2 in $\mathcal{X} \setminus \mathcal{X}_0$ using covariances. This method is similar to the inference discussed in Section 7.2. Finally, in Section 8.3, we use Bayesian inference.

8.1 Estimation of λ_2 using mean value relations

We used the method described in Section 7.1 and, for fixed m^1 and m^2, minimized (18). This method gave us an estimate $\hat{\lambda}_2$ of λ_2 up to a constant of proportionality. We scaled $\hat{\lambda}_2$ such that $0 \leq \hat{\lambda}_2(y_i) \leq 1$ for all $i = 1, \ldots, N$, with y_i being the midpoint of each voxel (pixel). The estimated activation

pattern was determined at each $x \in \mathcal{X}$ as

$$\sum_{i=1}^{N} h(x - y_i; m^2) \hat{\lambda}_2(y_i).$$

Figure 9 shows the estimated activation pattern for $m^1 = 5$ and $m^2 = (4, 4)$ (right) together with the true activation pattern (left). The method gives an estimate of the correct activation pattern, up to multiplication with a constant.
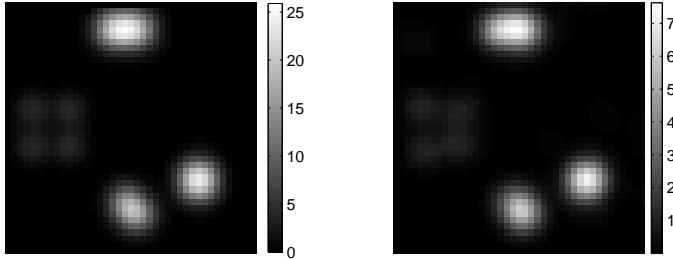

Figure 9: The true spatial activation pattern (left) and the estimated spatial activation pattern (right) with marks $m^1 = 5$ and $m^2 = (4, 4)$.

8.2   Estimation of λ_2 using covariances

We assume that we have given an activated area, $\mathcal{X}_0$, in $\mathcal{X}$ and wish to find other areas with functional connection to $\mathcal{X}_0$, using analysis based on covariances. Following Section 7.2 we calculate the slope of the regression of $Z_{tx'}$ on Z_{tx} for the simulated data, where x is the point in $\mathcal{X}$ with maximum intensity. This approach gives a first estimate of the spatial intensity function.

We can also estimate the spatial activation, using the covariances. We supposed the upper middle activation center in Figure 7 (right) to be known. We then used (21) to obtain an estimate $\hat{\lambda}_2(x)$ of $\tilde{\lambda}_2(x) = c\gamma(m^1)\bar{\beta}.\lambda_2(x)$ for all $x \in \mathcal{X} \setminus \mathcal{X}_0$. Given the estimate of the spatial intensity function, the spatial activation was reconstructed as in the previous section. The results for $m^1 = 5$ and $m^2 = (4, 4)$ are shown in Figure 11. As before, the method finds the correct activation areas, but the intensities are only known up to a multiplication with a constant.

8.3   Bayesian inference

We analyzed the simulated data in two different ways with the method described in Section 7.3. In the first case, we have restricted our attention to

26
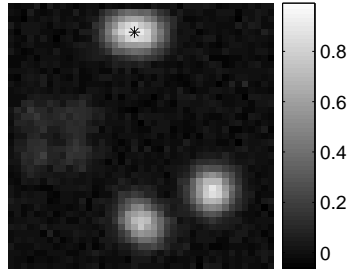
Figure 10: The slope of the regression of $Z_{tx'}$ on Z_{tx} for a fixed point $x \in \mathcal{X}$ and all $x' \in \mathcal{X}$. The point x, shown as a star in the figure, is the point in $\mathcal{X}$ with maximum intensity.
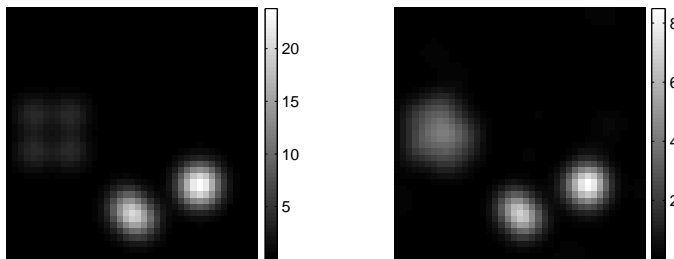

Figure 11: The true spatial activation pattern (left) and the estimated spatial activation pattern (right) for the marks $m^1 = 5$ and $m^2 = (4, 4)$. The upper middle activation center in Figure 7, denoted by $\mathcal{X}_0$ in the text above, is not shown, as it is assumed known and thus not estimated.

two regions of the brain, the high intensity region $\mathcal{X}_1$ and the low intensity region $\mathcal{X}_2$. The areas of these two regions are 51 and 49 pixels, respectively. We assumed there is no activation in $\mathcal{X} \setminus (\mathcal{X}_1 \cup \mathcal{X}_2)$, and so we used the method in Section 7.3 with $k = 2$. In the second case, we have set $k = 1$ with the region of interest equal to $\mathcal{X}$. The area of $\mathcal{X}$ is 1245 pixels. Figure 12 shows plots of the log posterior density, $\log p_{m,\sigma^2}(c, \pi, \phi_0 | z)$, as a function of iteration number. The normalization constant for the posterior density is unknown, cf. (24), so we only know the log posterior density up to addition with a constant. This is, however, irrelevant when the plots are used to study the convergence of the algorithm.

When the algorithm had converged, we sampled point processes $\{\Phi_j\}_{j=1}^M$ from the posterior and used them to estimate the activation pattern. The
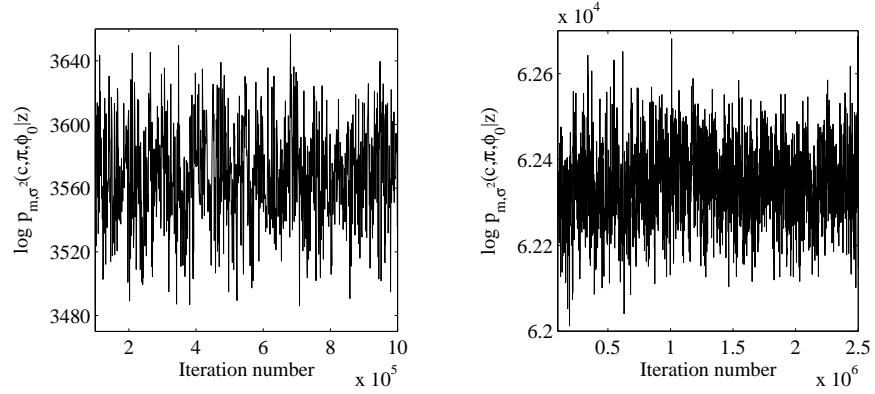
Figure 12: The log posterior density as a function of iteration number for $k = 2$ (left) and $k = 1$ (right). Note that the log posterior density is only know up to a constant, cf. (24). The values on the y-axis are thus only correct up to an additive constant.

estimated spatial activation pattern was determined at each $x \in \mathcal{X}$ as

$$\frac{1}{M} \sum_{j=1}^{M} \sum_{y_i \in \Phi_j} h(x - y_i; m^2).$$

In Figure 13, the resulting estimates of the activation pattern are shown together with the true activation pattern. Note that for comparison the true activation pattern shown in Figure 13, left, has been multiplied with 13, the number of time points of activation in the true pattern.
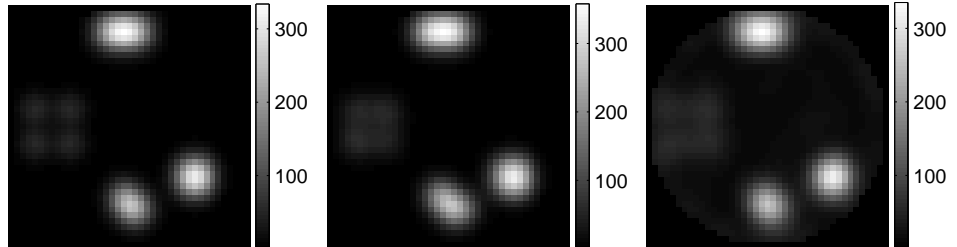
Figure 13: The true spatial activation pattern (left), the estimated spatial activation pattern for $k = 2$ (middle), and the estimated spatial activation pattern for $k = 1$ (right). The marks have values $m^2 = (4, 4)$ in all the figures.

28

The simulated point processes give us information about the temporal activation as well as the spatial activation. We estimate the temporal activation in the same manner as the spatial activation by

$$\frac{1}{M} \sum_{j=1}^{M} \sum_{s_i \in \Phi_j} g(t - s_i; m^1)$$

for each $t \in [0, T]$. The resulting estimates are shown in Figure 14 together with the true activation pattern. Note that for comparison the true activation pattern shown in Figure 14 (solid line) has been multiplied with 30, the number of activation centers in space in the true pattern.
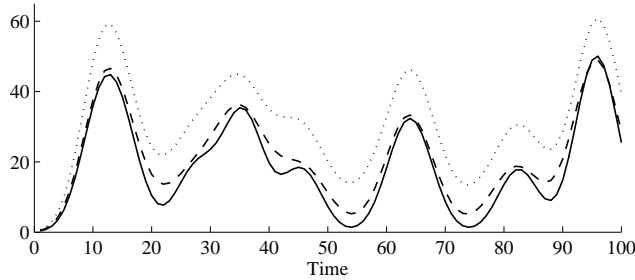

Figure 14: The true temporal activation pattern (solid), the estimated temporal activation pattern for $k = 2$ (dashed), and the estimated temporal activation pattern for $k = 1$ (dotted). The mark has value $m^1 = 5$.

In order to explain the higher level of activation obtained for $k = 1$, we have divided $\mathcal{X}$ into two parts and estimated the temporal activation pattern for $k = 1$ in each part separately. The first part, $\tilde{\mathcal{X}}_1$, consists of the areas that were used in the analysis for $k = 2$, along with those voxels in $\mathcal{X} \setminus (\mathcal{X}_1 \cup \mathcal{X}_2)$ influenced by voxels in $\mathcal{X}_1 \cup \mathcal{X}_2$. Thus,

$$\tilde{\mathcal{X}}_1 = \{x \in \mathcal{X} \mid \exists y \in \mathcal{X}_1 \cup \mathcal{X}_2 : h(x - y; m^2) \geq 2\}.$$

The threshold chosen equals half the maximum of the function h. The estimated temporal activation pattern for $\tilde{\mathcal{X}}_1$ is shown as a dotted line in Figure 15. The second part, $\tilde{\mathcal{X}}_2$, consists of the remaining voxels in $\mathcal{X}$, $\tilde{\mathcal{X}}_2 = \mathcal{X} \setminus \tilde{\mathcal{X}}_1$. The estimated temporal activation pattern for $\tilde{\mathcal{X}}_2$ is shown by a dash-dotted line in Figure 15. The estimated temporal activation pattern for $\tilde{\mathcal{X}}_1$ is close to the true pattern, while the estimated pattern for $\tilde{\mathcal{X}}_2$ is approximately uniform in time apart from an edge effect in the beginning. The higher level of the temporal activation pattern for $k = 1$ in Figure 14 can thus be explained by extra points, uniformly distributed in time, in the simulated point process outside the activated areas.

29
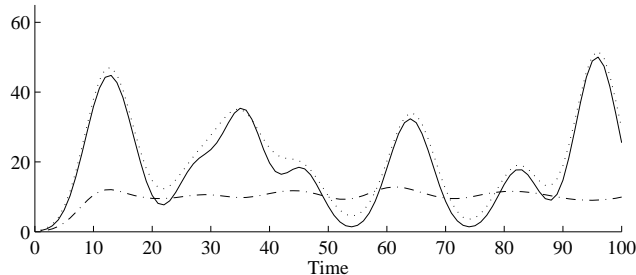
Figure 15: The true temporal activation pattern (solid), the estimated temporal activation pattern for $k = 1$ in activated areas (dotted), and the estimated temporal activation pattern for $k = 1$ in non-activated areas (dash-dotted). The mark has value $m^1 = 5$.

9 An example of analysis of fMRI data

The data we consider here are from a larger investigation of the resting state network, cf. Beckmann *et al.* (2005). The data have an exceptional high time resolution with 120 ms between neighboring time points. Such high resolution enables the investigator to distinguish neural effects from non-neural physiological effects such as aliased cardiac or respiratory cycles. An independent component analysis of these data revealed a resting state network involving the sensory-motor cortices bilaterally, cf. Beckmann *et al.* (2005). A Fourier analysis of the estimated temporal activation pattern of the network showed a dominating period of approximately 15-20 s.

The data are from a single slice through an axial plane that intersects the sensory-motor cortices bilaterally. The number of time points is 2000, corresponding to a total duration of the experiment of 4 min. After masking the data, in order to remove non-brain voxels, it consists of 932 voxels. We analyze this data under our model using Bayesian inference for one area, the whole slice, with $l = 5s$, $\theta_1 = 100$ and $\theta_2 = 2$. Initially, we performed band-pass filtration with limits of 1 s and 60 s in order to remove low frequency drift as well as some of the effects relating to cardiac and respiratory cycles. We have used the program FSL for the preprocessing of the data, see Smith *et al.* (2004) for an overview of FSL.

The resting state network found in Beckmann *et al.* (2005) involves three regions of interest, the middle region $\mathcal{X}_1$, the left motor cortex $\mathcal{X}_2$, and the right motor cortex $\mathcal{X}_3$ as shown in Figure 16. A Bayesian analysis supports such a network. In Figure 17 samples from the posteriori density of time points of activation in the three regions of interest are shown. Clearly, the three temporal point processes are positively correlated. Examples of observed

and estimated time series are shown in Figure 18 while the estimated spatial activation pattern in the three regions can be found in Figure 19.
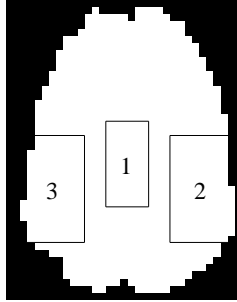
Figure 16: Delineation of the three regions of interest, $\mathcal{X}_1$, a middle region, $\mathcal{X}_2$ that includes the left motor cortex, and $\mathcal{X}_3$ that includes the right motor cortex.
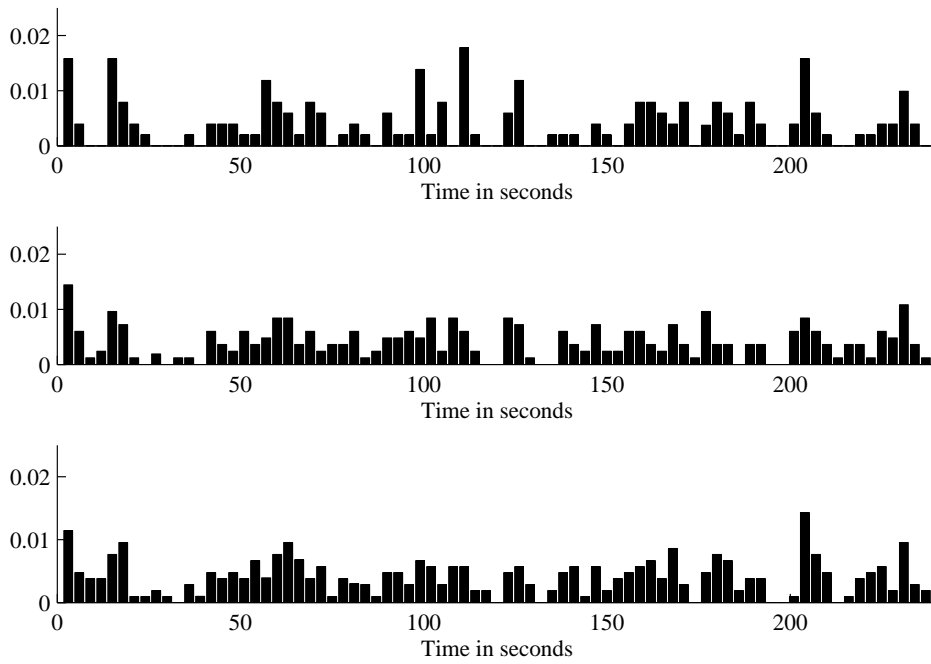
Figure 17: Samples from the posterior density of time points of activation for region $\mathcal{X}_1$ (top), $\mathcal{X}_2$ (middle), and $\mathcal{X}_3$ (bottom). Each bar represents 3 seconds.

31
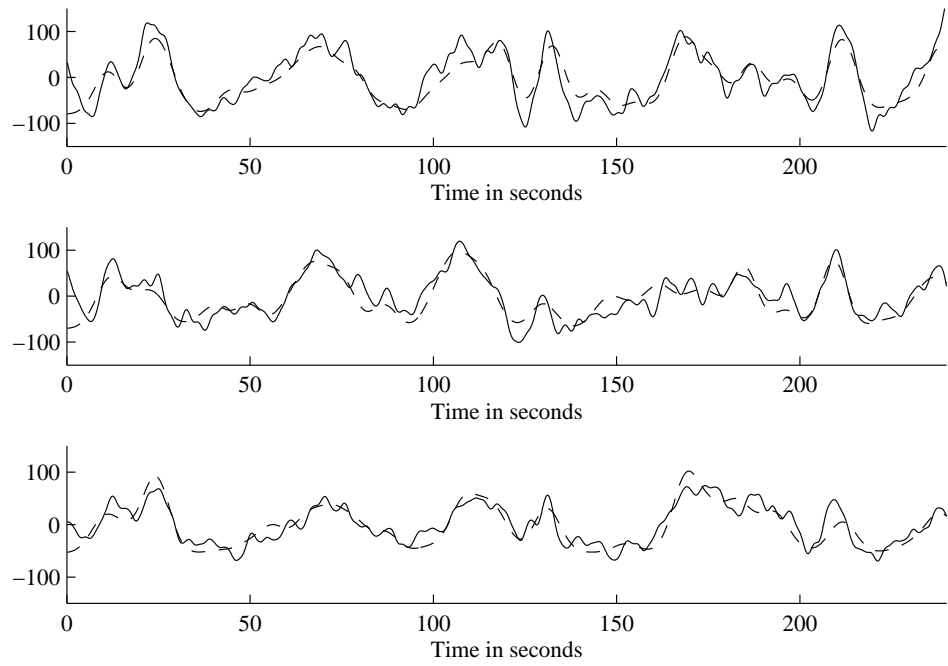
Figure 18: Examples of time series from the three regions after preprocessing (solid) together with the estimated temporal activation (dashed). The top figure shows a time series from $\mathcal{X}_1$, the middle figure shows a time series from $\mathcal{X}_2$, and the bottom figure shows a time series from $\mathcal{X}_3$.
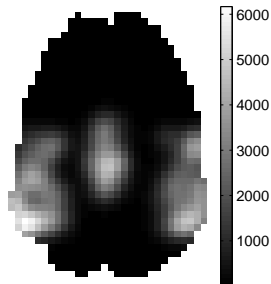
Figure 19: The estimated spatial activation pattern in the three regions cumulated over time.

32

10   Discussion

In fMRI experiments, data may have a more complicated structure than the one predicted by our model, cf. e.g. Hartvig (2002). An extended model will most likely include a drift component d_{tx}

$$Z_{tx} = \mu_x + d_{tx} + \sum_i f_{tx}(t_i, x_i; m_i) + \sigma_x \varepsilon_{tx}, \tag{26}$$

cf. Genovese (2000). This component describes the slow drifts in the static magnetic field during the experiment and residual motion not accounted for by prior motion correction. Often, the drift is removed using filtering, before any further analysis of the data, cf. Friston *el al.* (2000), or included in a general linear model, cf. Friston *et al.* (1995). It should also be part of an initial analysis to examine whether the data should be transformed. In Hartvig (2002), log-transformed signal intensities are analyzed by a model as in (26) with $\sigma_x^2 = \sigma^2$. Note that the variance of the untransformed intensities will then depend on t and x.

   In the present paper we have mainly used the simple model described in Section 3.1.1 for the temporal activity, one reason being that we want to focus on the spatial modeling. In Genovese (2000), models for the HRF are reviewed, including a model based on splines. In Purdon *et al.* (2001), a new model for a physiologically based hemodynamic response is described.

   We have assumed that the errors $\{\varepsilon_{tx}\}$ are mutually independent. It is here important to consider more general error models. In particular, the noise is often autocorrelated in time, as emphasized in Worsley (2000). A more general model for the errors is the multivariate Gaussian model,

$$\varepsilon \sim N_{|\mathcal{X}| \times T}(0, \Sigma). \tag{27}$$

For a standard whole brain analysis, the covariance model Σ will be very large, e.g. $|\mathcal{X}| \times T = 10000 \times 100 = 10^6$. It is therefore necessary to make some simplifications of the model to make it computationally feasible. In Woolrich *et al.* (2004), this type of noise models is investigated in Bayesian settings. The authors propose the use of a space-time simultaneously specified autoregressive model,

$$\varepsilon_{tx} = \sum_{y \in \mathcal{N}_x} \beta_{xy} \varepsilon_{(t-1)y} + \sum_{s=1}^{3} \alpha_{sx} \varepsilon_{(t-s)x} + \eta_{tx},$$

where $\mathcal{N}_x$ is a neighborhood of the voxel x, β_{xy} is the spatial autocorrelation between voxel x and y at a time lag of one with $\beta_{xy} = \beta_{yx}$, α_{sx} is the temporal autocorrelation between time point t and $t - s$ at voxel x, and $\{\eta_{tx}\}$ are independent noise variables with distribution

$$\eta_{tx} \sim N(0, \sigma_\eta^2).$$

It still remains to study more systematically explicit point process models that can describe how activities in different regions of the brain are related. The regions may either be activated simultaneously or some regions may be activated with delay compared to other regions. For modeling the spatial point process $\{x_i\}$, Taskinen (2001) has suggested a cluster point process. Note also that the point process term

$$\sum_i f_{tx}(t_i, x_i; m_i)$$

of (26) has the form of the random intensity field of a shot noise Cox process if Ψ is Poisson, see e.g. Møller (2003).

From an applied point of view, an important next step is to design non-stimulus experiments along the lines described in Greicius *et al.* (2003) and analyze the data, using the modeling framework presented in this paper. In the examples considered until now, we have assumed that the marks are identical for all activations. The common value m has been treated as an unknown parameter. It will be interesting to include the distribution of the temporal duration of the activation in a Bayesian analysis.

One further possibility for extending the model is to consider K independent marked spatio-temporal point processes Ψ_k, $k = 1, \ldots, K$, instead of just one spatio-temporal point process. In the particular case of independent spatial and temporal point processes where

$$\Psi_k = (\Psi_{k1}, \Psi_{k2}),$$

and $\Psi_{k1} = \{[t_{ki}; m_{ki}^1]\}$ and $\Psi_{k2} = \{[x_{kj}; m_{kj}^2]\}$ are independent, we obtain the following model equation

$$Z_{tx} = \mu_x + \sum_{k=1}^{K} A_{kt} B_{xk} + \sigma_x \varepsilon_{tx},$$

where

$$A_{kt} = \sum_i g(t - t_{ki}; m_{ki}^1) \text{ and } B_{xk} = \sum_j h(x - x_{kj}; m_{kj}^2).$$

Note that $\{A_{k*}\}$ are independent corresponding to a temporal ICA model and $\{B_{*k}\}$ are independent corresponding to a spatial ICA model, respectively, cf. McKeown *et al.* (2003). The resulting model may be analyzed by first performing an ICA analysis and then analyzing the estimated components, using point process theory.

11   Summary

In the present paper, we have suggested a new modeling framework for non-stimulus experiments, using point process theory. The key idea is to replace

the controlled on-off activation times from repeated stimulus experiments with *random* activation times from a stationary point process. Bayesian analysis of the model provides an estimate of the posterior distribution of the spatio-temporal point process of activations. Such dynamic output (including the posterior density of time points of activation) is not provided by the standard methods available for analysis. The model may be used for an exploratory analysis of the whole brain or a more detailed analysis of parts of the brain that have been spotted as regions of special interest in earlier analyses. Since knowledge of the activation profile is used in the model, it is expected that the new approach will give a more clear picture of what is going on in the brain than nonparametric analysis like Greicius' regression method. The model offers a way of further analyzing output from ICA analysis.

Acknowledgments

Bibliography

Beckmann, C.F., DeLuca, M., Devlin, J.T., and Smith, S.M. (2005): Investigations into resting-state connectivity using independent component analysis. *Philosophical Transactions of the Royal Society B* **360** 1001-1013.

Beckmann, C.F. and Smith, S.M. (2005): Tensorial extensions of independent component analysis for multisubject fMRI analysis. *NeuroImage* **25** 294-311.

Buxton, R.B., Uludağ, K., Dubowitz, D.J., and Liu, T.T. (2004): Modelling the hemodynamic response to brain activation. *NeuroImage* **23** 220-233.

Buckner, R.L., Snyder, A.Z., Sanders, A.L., Raichle, M.E. and Morris, J.C. (2000): Functional brain imaging of young, nondemented, and demented older adults. *Journal of Cognitive Neuroscience* **12 (Supplement 2)**, 24-34.

Cao, J. and Worsley, K. (1999): The geometry of correlation fields with an application to functional connectivity of the brain. *The Annals of Applied Probability* **9** 1021-1057.

Friston, K.J. (1998): Modes or models: a critique on independent component analysis for fMRI. With discussion. *Trends in Cognitive Sciences* **2** 373-375.

Friston, K.J. (2002): Bayesian estimation of dynamical systems: an application to fMRI. *NeuroImage* **16** 513-530.

Friston, K.J., Flecther, P., Josephs, O., Holmes, A., Rugg, M.D., and Turner, R. (1998): Event-related fMRI: characterizing differential responses. *NeuroImage* **7** 30-40.

Friston, K.J., Glaser, D.E., Henson, R.N.A., Kiebel, S., Phillips, C., and Ashburner, J. (2002b): Classical and Bayesian inference in neuroimaging: applications. *NeuroImage* **16** 484-512.

Friston, K.J., Holmes, A.P., Poline, J.-B., Grasby, P.J., Williams, S.C.R., Frackowiak, R.S.J., and Turner, R. (1995): Analysis of fMRI time-series revisited. *NeuroImage* **2** 45-53.

Friston, K.J., Josephs, O., Zarahn, E., Holmes, A.P., Rouquette, and Poline, J.-B. (2000): To smooth or not to smooth? *NeuroImage* **12** 196-208.

Friston, K.J., Penny, W., Philips, C., Kiebel, S., Hinton, G., and Ashburner, J. (2002a): Classical and Bayesian inference in neuroimaging: theory. *NeuroImage* **16** 465-483.

Genovese, C.R. (2000): A Bayesian time-course model for functional magnetic resonance imaging data. With discussion and a reply by the author. *Journal of the American Statistical Association* **95** 691-719.

Glover, G.H. (1999): Deconvolution of impulse response in event related fMRI. *NeuroImage* **9** 416-429.

Greicius, M.D., Krasnow, B., Reiss, A.L., and Menon, V. (2003): Functional connectivity in the resting brain: a network analysis of the default mode hypothesis. *Proceedings of the National Academy of Sciences USA* **100** 253-258.

Greicius, M.D., Srivastava, G., Reiss, A.L., and Menon, V. (2004): Default-mode network activity distinguishes Alzheimer's disease from healthy aging: Evidence from functional MRI. *Proceedings of the National Academy of Sciences USA* **101(13)** 4637-4642.

Hartvig, N.V. (1999): A stochastic geometry model for fMRI data. Research Report 410, Department of Theoretical Statistics, University of Aarhus.

Hartvig, N.V. (2000): Parametric modelling of functional magnetic resonance imaging data. PhD thesis, Department of Theoretical Statistics, University of Aarhus.

Hartvig, N.V. (2002): A stochastic geometry model for functional magnetic resonance images. *Scandinavian Journal of Statistics* **29** 333-353.

Lange, N. and Zeger, S.L. (1997): Non-linear Fourier time series analysis for human brain mapping by functional magnetic resonance imaging. With discussion and a reply by the author. *Journal of the Royal Statistical Society, Series C (Applied Statistics)* **46** 1-29.

McKeown, M.J., Hansen, L.K., and Sejnowski, T.J. (2003): Independent component analysis of functional MRI: what is signal and what is noise? *Current Opinion in Neurobiology* **13** 620-629.

Møller, J. (2003): Shot noise Cox processes. *Advances in Applied Probability* **35** 614-640.

Møller, J. and Waagepetersen, R.P. (2004): *Statistical Inference and Simulation for Spatial Point Processes*, Chapman & Hall/CRC, New York.

Ogawa, S., Tank, D.W., Menon, R., Ellermann, J.E., Kim, S., Merkle, H., and Ugurbil, K. (1992): Intrinsic signal changes accompanying sensory stimulation: functional brain mapping with magnetic resonance imaging. *Proceedings of the National Academy of Sciences USA* **89** 5951-5955.

Purdon, P.L., Solo, V., Weisskoff, R.M., and Brown, E.N. (2001): Locally regularized spatiotemporal modeling and model comparison for functional MRI. *NeuroImage* **14** 912-923.

Smith, S.M., Jenkinson, M., Woolrich, M.W., Beckmann, C.F., Behrens, T.E.J., Johansen-Berg, H., Bannister, P.R., De Luca, M., Drobnjak, I., Flitney, D.E., Niazy, R.K., Saunders, J., Vickers, J., Zhang, Y., De Stefano, N., Brady, J.M., and Matthews, P.M. (2004): Advances in functional and structural MR image analysis and implementation as FSL. *NeuroImage* **23** S208-S219.

Stone, J.V. (2002): Independent component analysis: an introduction. *Trends in Cognitive Sciences* **6** 59-64.

Stoyan, D., Kendall, W.S., and Mecke, J. (1995): *Stochastic Geometry and Its Applications*, second edn. John Wiley & Sons, Chichester.

Taskinen, I. (2001): Cluster priors in the Bayesian modelling of fMRI data. *PhD Thesis*. Department of Statistics, University of Jyväskylä, Jyväskylä.

Tonini, G., McIntosh, A.R., Russell, D.P., and Edelman, G.M. (1998): Functional clustering: identifying strongly interactive brain regions in neuroimaging data. *NeuroImage* **7** 133-149.

Woolrich, M.W., Jenkinson, M., Brady, J.M., and Smith, S.M. (2004): Fully Bayesian spatio-temporal modeling of fMRI data. *IEEE Transactions on Medical Imaging* **23** **(2)** 213-231.

Worsley, K.J. (2000): Comment on *A Bayesian time-course model for functional magnetic resonance imaging* by C. Genovese. *Journal of the American Statistical Association* **95** 691-719.

Modelling resting state networks
in the human brain

Thordis L. Thorarinsdottir and Eva B. Vedel Jensen
University of Aarhus

Abstract

In the present paper, we show how spatio-temporal point process models for functional magnetic resonance imaging (fMRI) data can be used in the study of resting state networks in the human brain. The model explicitly includes knowledge of the hemodynamic response to neuronal activation. Fully Bayesian analysis of the model is described and an example of analysis of a fMRI data set is given. Other methods of analysis of resting state networks are also discussed.

Keywords: Bayesian inference, fMRI, hemodynamic response function, Markov chain Monte Carlo, spatio-temporal point processes

1   Introduction

Cognitive psychologists and neuroscientists are presently very interested in the functioning of the human brain during rest. One of the reasons is that analyses of data obtained by functional magnetic resonance imaging (fMRI) indicate the existence of resting state networks of regions in the human brain, cf. [3, 7, 8, 15] and references therein. See also the collection of papers presented in the special issue of *Phil. Trans. R. Soc.* from 2005 on 'Multimodal neuroimaging of brain connectivity'. Changes of these networks under aging or disease have been reported ([5], [15]).

During an fMRI experiment the brain is scanned and represented as a set of voxels. At each voxel a time series of MR signal intensities is recorded, showing the local brain activity during the experiment. Time series from regions far apart may show similar variation during rest, indicating the presence of a resting state network. An example of such data, earlier analyzed in [3], is shown in Fig. 1. At each voxel of a slice through the human brain, the MR signal intensity is shown at 12 equidistant time points of the scanning experiment. The person being scanned here has not received any particular stimuli
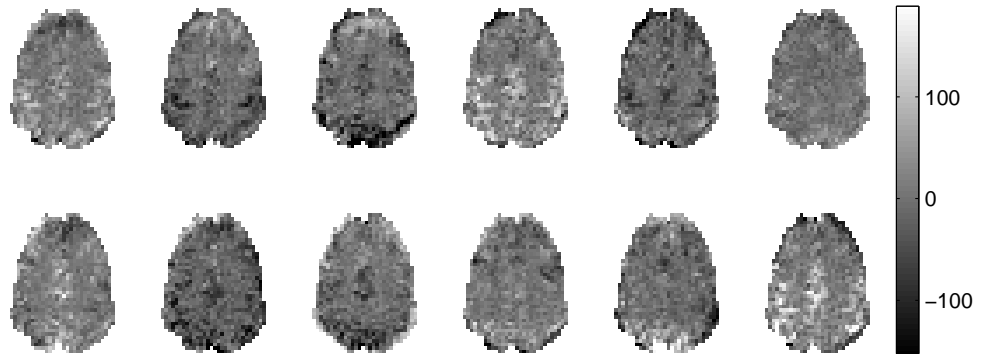
Figure 1: Development of the MR signal intensity over time in a single axial slice through the human brain. From left to right and top to bottom: the activity at time $t = 12, 30, 48, \ldots, 210$ seconds.

during the experiment but still covariation between activities in different regions of the brain may appear. As we shall see, there is evidence of covariation between activities in the three regions shown in Fig. 3 below, but this is not immediate from Fig. 1. We will return to this example at the end of the paper. Generally, modelling and statistical analysis of such data constitute a major challenge because of a high level of noise and no prior knowledge of time points of activation. Another complication is possible aliasing with respiratory and cardiac cycles. The difficulties faced in such non-stimulus experiments are much more serious than those met in more traditional experimental designs of fMRI experiments with known periods of stimuli ('on periods') between periods of rest ('off periods'). Recently, experiments with a more continuous but known type of stimulus has also been tried out, cf. [1, 2]. A good statistical review on design of fMRI experiments may be found in [10].

The aim of this paper is to show how spatio-temporal point process models for functional magnetic resonance imaging (fMRI) data can be used in the study of resting state networks in the human brain. A more detailed account will be published elsewhere [19].

2 Correlation analysis

The data from an fMRI experiment constitute a collection of time series

$$Z_{tx}, \quad t = t_1, \ldots, t_m,$$

$x \in \mathcal{X}$. Here, Z_{tx} is the MR signal intensity at time t and voxel x. The time points $t_1, \ldots, t_m$ are usually equidistant and belong to the interval $[0, T]$, where T is the length of the experiment. The set $\mathcal{X}$ is a finite subset of $\mathbb{R}^2$ or

2

$\mathbb{R}^3$ with N elements, called voxels, representing a two dimensional slice or a three dimensional volume of the brain.

In [8], the functional connectivity in the resting brain is studied by a simple correlation analysis. A seed region $\mathcal{X}_0 \subset \mathcal{X}$ is selected and the correlation between the average time series for this region

$$\bar{Z}_{t\mathcal{X}_0} = \frac{1}{|\mathcal{X}_0|} \sum_{x \in \mathcal{X}_0} Z_{tx}, \quad t = t_1, \ldots, t_m$$

and the time series of any other brain voxel is calculated in order to find regions $\mathcal{X}_1$ interacting with $\mathcal{X}_0$. Here, $|\cdot|$ indicates number. Similarly, in [13], the average time series is used as explanatory variable in a regression type of analysis of the time variation in other regions of the brain. The software package SPM (Statistical Parametric Mapping), developed by the Wellcome Department of Imaging Neuroscience, UCL, UK, can be used for such an analysis.

This analysis is attractive because it is simple. It does, however, require an a priori expectation of the network pattern.

3   Independent component analysis

Independent component analysis (ICA) has become a very popular technique for analyzing data from fMRI experiments without specific stimuli. A number of interesting findings relating to specific resting state networks have been reported using ICA ([3, 14, 15]). A special variant of the technique is called probabilistic independent component analysis (PICA), cf. [7]. There were some early critiques of ICA, see [9], but it seems now to be generally recognized in the neuroscience community that ICA is a powerful nonparametric tool for studying resting state networks. A good introduction to ICA can be found in [21]. This paper also contains a comprehensive list of references with specific guidance to the literature. Analysis of groups of individuals by ICA is discussed in [4].

ICA is an explorative analysis, closely related to factor analysis and discriminant analysis. The analysis is based on a model of the following type

$$Z_{tx} = \mu_x + \sum_{k=1}^{K} A_{tk} B_{kx} + \sigma \epsilon_{tx}.$$

Here, μ_x is the baseline signal at voxel x which can vary by a factor of 2-3 across the brain. The number K of components is unknown. Furthermore, $(A_{\star k}, B_{k\star}), \quad k = 1, \ldots, K$, are assumed to be independent. Software packages performing ICA are available, e.g. the program FSL presented in [25]. An ICA analysis results in estimates of temporal activation profiles $\{A_{\star k}\}$ and spatial

activation profiles $\{B_{k\star}\}$ for each k. The estimated temporal profiles are shown together with their associated power spectra. Only frequency components of a certain bandwidth are regarded as having neuronal origin. High frequence components may be caused by cardiac or respiratory activities, while very low frequence components are considered to be drift. In an actual application, the estimated number K of components may be quite large.

4 A model based on spatio-temporal point processes

Especially amongst psychologists, there has recently been some criticism of ICA analysis because such an analysis decomposes a particular type of activity in the brain into a spatial activation map showing regions of the brain activated during the experiment and a temporal activation graph showing when the brain is activated during the experiment. They are not particularly fond of this type of 'product brain'. Instead, a more dynamic type of analysis is asked for in order to be able to reveal more complicated interaction phenomenon. For instance, a particular region of the brain may only be active if a collection of other regions are active. An example of this is the visual system which seems to have a very strong hierarchical structure, see [17]. It may also be of interest to investigate whether the duration and extend of activation may depend on the particular region of the brain studied. As we shall see, this criticism can be met by using a spatio-temporal point process modelling approach.

The model to be presented depends on well established knowledge on the hemodynamic response which is a localized inflow of oxygenated blood to a region of the brain with neural activity. This response causes an increase of the MR signal intensity in the region in question. Its general temporal form has been reproduced in many studies. First, the hemodynamic response increases to a peak value at about 4–7 seconds after a neuronal response and then it returns to baseline again a few seconds after the neuronal impulse has ceased.

A neuronal activation at location y and time u will therefore contribute to the observed MR signal intensity at y at the later time $t > u$ by an amount proportional to

$$g(t - u)$$

where g is a function with the properties described above. In particular, $g(v)$ increases to a maximal value for v equal to 4-7 seconds and then decreases to 0 after the neuronal activation has stopped. A neuronal activity in voxel y is expected to affect the activity at neighbour voxels in a similar way but less intensely. For a voxel x, an activation at location y and time u will contribute to the observed MR signal intensity at x at the later time $t > u$ by the following

amount

$$g(t - u)h(x - y),$$

where $h(z)$ is a decreasing function of $\|z\|$. The resulting model for the contribution to the observed MR signal intensity at voxel x at time t caused by a neuronal activation at voxel y at time u becomes

$$f_{tx}(u, y; m) = g(t - u; m^1)h(x - y; m^2)$$

where $m = (m^1, m^2)$ and m^1 and m^2 are model parameters, describing the duration of a neuronal activation and its spatial extent.

The actual modelling of the hemodynamic response function g has been studied intensively in the fMRI literature, see [6] and references therein. We will here adopt a fairly simple but well-known model where the response is a Gaussian distributed random variable with mean 6 sec (the delay) and variance 9 sec^2. Accordingly, the function g takes the form

$$g(u; m^1) = \int_0^{m^1} \kappa(u - v)dv,$$

where m^1 is the temporal duration of the neuronal activation and

$$\kappa(t) = \frac{1}{\sqrt{2\pi}3} \exp\left(-\frac{(t - 6)^2}{18}\right).$$

The spatial activation function is modelled by a Gaussian bell function

$$h(y; m^2) = \theta_1 \exp\left(-\frac{\|y\|^2}{2\theta_2}\right),$$

where $m^2 = (\theta_1, \theta_2)$.

In Fig. 2, we show the effect of superposition of three such activations. Here, $\mathcal{X}$ is a digitized circular disc. The activation profile

$$\left\{ \sum_{i=1}^3 f_{tx}(t_i, x_i; m) : x \in \mathcal{X} \right\}$$

is shown for 12 equidistant time points. The time points and positions of the three activations (t_i, x_i), $i=1, 2, 3$, are indicated in the legend of Fig. 2. The duration m^1 and the spatial extent m^2 are the same for all three activations.

In an fMRI experiment without specific stimuli, the activations occur at random time points not known to the experimenter. It is natural to describe the activations by a marked point process $\Psi = \{[t_i, x_i; m_i]\}$ on $\mathbb{R} \times \mathcal{X}$ with
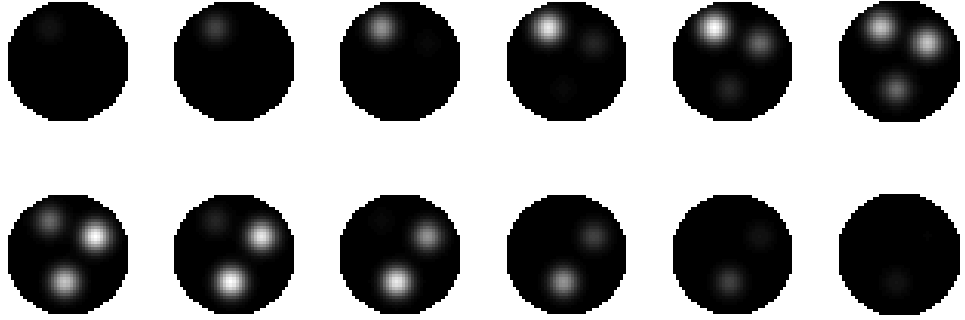
Figure 2: Development of the activity over time in simulated data. From left to right and top to bottom: the activity at time $t = 2, 4, \ldots, 24$ time units. The activity starts at times $t = 1, 6, 8$, clockwise from the top, and the marks are given by $m^1 = 5$ time units and $m^2 = (10, 10)$ voxel units. The diameter of the circular disc is 40 voxel units. For more details, see the text.

marks $m_i = (m_i^1, m_i^2) \in \mathbb{R}_+^3$. The resulting model for the observed MR signal intensity at time t and voxel x becomes

$$Z_{tx} = \mu_x + \sum_i f_{tx}(t_i, x_i; m_i) + \sigma \epsilon_{tx}, \tag{1}$$

where μ_x is the baseline signal at voxel x as above and ϵ_{tx} is an error term with mean 0 and variance 1. The errors are expected to be correlated, see [20, 26]. It can be shown that this spatio-temporal model is closed under local smoothing, cf. [19].

Since the brain is not subjected to systematic stimuli under the fMRI experiment, it is natural to assume (investigate) that the marked point process Ψ is time stationary in the sense that

$$\Psi_t = \{[t_i + t, x_i; m_i]\}$$

has the same distribution as Ψ for all $t \in \mathbb{R}$. Then, the intensity measure Λ of the unmarked point process is of the form

$$\Lambda = c\nu^1 \times \Lambda_2,$$

where $c > 0$, ν^1 is the Lebesgue measure on $\mathbb{R}$ and Λ_2 is the intensity measure for the spatial point process $\{x_i\}$. Furthermore, time stationarity implies that the mark distribution does not depend on the particular time point considered but it may still depend on the location.

Under the resting state network hypothesis, the spatio-temporal point process Ψ will show long-distance dependencies. Recall that each marked point

$[t_i, x_i; m_i]$ may be considered as a center of activation at location $x_i \in \mathcal{X}$ starting at time t_i and with temporal and spatial duration described by m_i. If two regions of the brain $\mathcal{X}_0$ and $\mathcal{X}_1$ interact, it is expected that activations occur almost simultaneously in $\mathcal{X}_0$ and $\mathcal{X}_1$. Such interactions may be revealed, using a ayesian analysis, see Section 5 below. The earlier modelling of a 'product brain' corresponds to the use of independent spatial and temporal point processes such that

$$\Psi = \{[t_i, x_j; m_i^1, m_j^2]\},$$

where $\Psi_1 = \{[t_i; m_i^1]\}$ and $\Psi_2 = \{[x_j; m_j^2]\}$ are independent. If the intensity measure of Ψ_2 is very concentrated in $\mathcal{X}_0$ and $\mathcal{X}_1$, then activations will appear simultaneously in the two regions. This type of modelling of the dependency may appear somewhat simplistic and a model based on conditional independence may be more natural. Here,

$$\Psi = \{[t_i, x_{ij}; m_i^1, m_{ij}^2]\},$$

where, given $\Psi_1 = \{[t_i; m_i^1]\}$, $\Psi_{2i} = \{[x_{ij}; m_{ij}^2]\}$ are independent and identically distributed with an intensity measure concentrated in $\mathcal{X}_0$ and $\mathcal{X}_1$, say.

In accordance with the emerging belief of the existence of more than one resting state network, it is natural to consider a point process model of the type $\Psi = \bigcup_{k=1}^{K} \Psi_k$ where $\Psi_k, k = 1, \ldots, K$, are independent and refer to activities in the K networks. If

$$\Psi_k = (\Psi_{k1}, \Psi_{k2})$$

where $\Psi_{k1} = \{[t_{ki}; m_{ki}^1]\}$ and $\Psi_{k2} = \{[x_{kj}; m_{kj}^2]\}$ are independent, then we obtain the following model equation

$$Z_{tx} = \mu_x + \sum_{k=1}^{K} A_{tk} B_{kx} + \sigma \epsilon_{tx}, \tag{2}$$

where

$$A_{tk} = \sum_i g(t - t_{ki}; m_{ki}^1) \text{ and } B_{kx} = \sum_j h(x - x_{kj}; m_{kj}^2).$$

Note that (2) is actually an ICA model. The model may be analyzed by first performing an ICA analysis and then analyzing the estimated components, using point process theory.

In the next section we will discuss Bayesian inference of the spatio-temporal point process model (1) and its parameters. A related model for repeated stimulus experiments has been developed in [16], see also [12].

7

5 Bayesian inference

5.1 Prior distributions

Without loss of generality we can set $\mu_x = 0$ in the following. The prior distribution of Ψ will be that of a Poisson point process. A typical point will, for convenience, be written as $[t, x; (\theta_0, \theta_1, \theta_2)] \in \mathbb{R} \times \mathcal{X} \times \mathbb{R}_+^3$ so we write here θ_0 instead of m^1 for the temporal duration of the neuronal activation. The intensity function of Ψ is assumed to be of the form

$$\lambda_\Psi(t, x; \theta_0, \theta_1, \theta_2) = \lambda(t, x) \prod_{i=0}^2 \mathbf{1}\{\theta_i \in [a_i, b_i]\},$$

where a_i, b_i, $i = 0, 1, 2$, are known positive constants. Note that there is no interaction between points in this prior distribution so interactions will appear in the posterior distribution if they are present in the data.

We consider the restriction Ψ_0 of Ψ to

$$\mathcal{Y} = [T_{0-}, T_{0+}] \times \mathcal{X} \times \prod_{i=0}^2 [a_i, b_i],$$

where the interval $[T_{0-}, T_{0+}]$ has been chosen such that an activation occurring outside this interval is very unlikely to affect the MR signal observed in $[0, T]$. The density of Ψ_0 with respect to the unit rate Poisson point process on $\mathcal{Y}$ becomes

$$p(\psi_0 | \lambda, a_*, b_*) = \exp\left(-\prod_{i=0}^2 (b_i - a_i) \int_{[T_{0-}, T_{0+}] \times \mathcal{X}} [\lambda(t, x) - 1] dt dx\right)$$

$$\times \prod_{[u, y; \theta_0, \theta_1, \theta_2] \in \psi_0} \left[\lambda(u, y) \prod_{i=0}^2 \mathbf{1}\{\theta_i \in [a_i, b_i]\}\right].$$

We will model the function λ by a piecewise constant function only depending on location, i.e.

$$\lambda(t, x) = \sum_{l=1}^K \lambda_l \mathbf{1}\{x \in \mathcal{X}_l\}.$$

Here, the disjoint sets $\mathcal{X}_l$ are supposed to be specified by the experimenter while the parameters λ_l are unknown. The union of the sets $\mathcal{X}_l$ need not be the whole brain. We can write the intensity function as

$$\lambda(t, x) = c\lambda_2(x)$$

where $c > 0$ and

$$\int_{\mathcal{X}} \lambda_2(x)dx = 1.$$

Note that λ_2 is on the following form

$$\lambda_2(x) = \sum_{l=1}^{k} \pi_l \frac{\mathbf{1}\{x \in \mathcal{X}_l\}}{|\mathcal{X}_l|}$$

where $\pi_l > 0$ and $\sum_{l=1}^{k} \pi_l = 1$.

We will use non-informative priors for c, $\pi = (\pi_1, \ldots, \pi_k)$ and the error variance σ^2. The prior density of c will be specified as

$$p(c) = \frac{1}{(c_+ - c_-)} \mathbf{1}\{c \in [c_-, c_+]\}$$

while the prior density of π is

$$p(\pi) = \frac{1}{\text{vol}(D)} \mathbf{1}\{\pi \in D\},$$

where

$$D = \left\{ \pi \in \mathbb{R}^k : \pi_l > 0, \sum_{l=1}^{k} \pi_l = 1 \right\}.$$

The prior density of σ^2 will be of the form

$$p(\sigma^2) = \frac{1}{(\sigma_+ - \sigma_-)} \mathbf{1}\{\sigma \in [\sigma_-, \sigma_+]\}.$$

5.2   The likelihood model

Let the data be denoted by

$$z = \{z_{tx} : t = t_1, \ldots, t_m, x \in \mathcal{X}\}.$$

Then, the conditional density of z given c, π, ψ_0 and σ is

$$p(z|\psi_0, \sigma) = [2\pi\sigma^2]^{-Nm/2} \exp\left(-\frac{1}{2\sigma^2} \|z - f(\psi_0)\|^2 \right), \tag{3}$$

where

$$\|z - f(\psi_0)\|^2 = \sum_{t,x} \left(z_{tx} - \sum_{[t_i, x_i; \theta_{i0}, \theta_{i1}\theta_{i2}] \in \psi_0} f_{tx}(t_i, x_i; \theta_{i0}, \theta_{i1}, \theta_{i2}) \right)^2.$$

This is the simplest choice of model, see also [20] and references therein. Note that (3) does not depend on c and π.

9

5.3 Posterior simulation

The posterior density will be of the following form

$$p(c, \pi, \sigma, \psi_0 | z) \propto p(c)p(\pi)p(\sigma^2)p(\psi_0 | c, \pi)p(z | \psi_0, \sigma)$$

since the conditional density of ψ_0 given c, π and σ only depends on c and π and the conditional density of z given the remaining variables only depends on ψ_0 and σ. For the simulation from the posterior density we use a fixed scan Metropolis within Gibbs algorithm where in each scan c, π, σ and ψ_0 are updated in turn. For a detailed description of algorithms of this kind, see [24]. The full conditional for c is a Gamma distribution with restricted range while for $k > 2$ the full conditional of π is a Dirichlet distribution. The full conditional of σ^2 is an inverse Gamma distribution with restricted range.

Finally, we need to simulate from

$$p(\psi_0 | c, \pi, z) \propto c^{n(\psi_0)} \prod_{l=1}^{k} \pi_l^{n_l(\psi_0)} \exp\left(-\frac{1}{2\sigma^2} \|z - f(\psi_0)\|^2 \right).$$

Note that this is in fact a pairwise interaction density. The point process is simulated using a birth, death and move algorithm as described in Chapter 7 of [23].

5.4 An example

We consider here shortly a Bayesian analysis of a fMRI data set analyzed in [3] by ICA analysis and illustrated in Fig. 1. In the Bayesian analysis performed here, the values of $\theta_\star$ and σ^2 were fixed and equal to empirically assessed values. In [3], evidence was found of a resting state network involving three regions of the brain slice, the left and right motor cortices and a middle region. Those regions are delineated in Fig. 3. In Fig. 4, we show the estimated two-dimensional posterior density of time points of activation for pairs of regions from Fig. 3. All estimated correlations are positive and significantly different from zero. In Fig. 5, we show examples of observed time series and their estimated temporal activation.

Acknowledgements
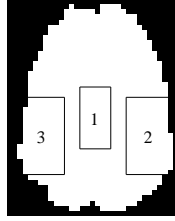
Figure 3: Delineation of the three regions of interest, $\mathcal{X}_1$, a middle region, $\mathcal{X}_2$ that includes the left motor cortex, and $\mathcal{X}_3$ that includes the right motor cortex.
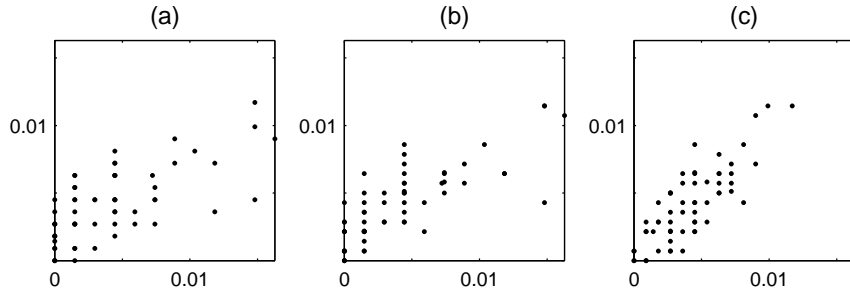
Figure 4: Two-dimensional posterior densities of time points of activation for pairs of regions delineated in Fig. 3. Regions $\mathcal{X}_1$ and $\mathcal{X}_2$ are shown in (a), $\mathcal{X}_1$ and $\mathcal{X}_3$ in (b) and $\mathcal{X}_2$ and $\mathcal{X}_3$ in (c). Each point represents a time interval of 4 seconds.
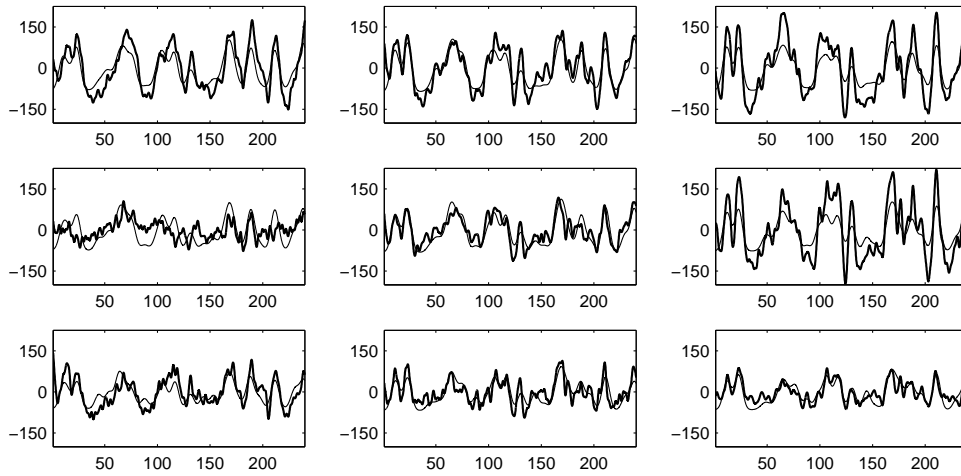
Figure 5: Time series from nine neighbouring voxels from the left motor cortex. In each plot, the thick line is the true, preprocessed time series for that voxel and the thin line is the estimated time series for the same voxel. The units on the x-axis are given in seconds.

11

Bibliography

[1] Bartels, A. and Zeki, S.: *The Chronoartitecture of the Human Brain - Natural Viewing Conditions Reveal a Time-based Anatomy of the Brain.* NeuroImage **22** (2004), 419–433.

[2] Bartels, A. and Zeki, S.: *Brain Dynamics during Natural Viewing Conditions – A New Guide for Mapping Connectivity in Vivo.* NeuroImage **24** (2005), 339–349.

[3] Beckmann, C. F., DeLuca, M., Devlin, J. T. and Smith, S. M.: *Investigations into Resting-State Connectivity using Independent Component Analysis.* Phil. Trans. R. Soc. B **360** (2005), 1001–1013.

[4] Beckmann, C. F. and Smith, S. M.: *Tensorial Extensions of Independent Component Analysis for Multisubject FMRI Analysis.* NeuroImage **25** (2005), 294–311.

[5] Buckner, R. L., Snyder, A. Z., Sanders, A. L., Raichle, M. E. and Morris, J. C.: *Functional Brain Imaging of Young, Nondemented, and Demented Older Adults.* Journal of Cognitive Neuroscience **12** (2000), 24–34.

[6] Buxton, R. B., Uludağ, K., Dubowitz, D. J. and Liu, T. T.: *Modelling the Hemodynamic Response to Brain Activation.* NeuroImage **23** (2004), 220–233.

[7] De Luca, M., Beckmann, C. F., De Stefano, N., Matthews, P. M. and Smith, S. M.: *FMRI Resting State Networks Define Modes of Long-distance Interactions in the Human Brain.* NeuroImage **29** (2006), 1359–1367.

[8] Fox, M. D., Snyder, A. Z., Vincent, J. L., Corbetta, M., Van Essen, D. C. and Raichle, M. E.: *The Human Brain is Intrinsically Organized into Dynamic, Anticorrelated Functional Networks.* PNAS **102** (2005), 9673–9678.

[9] Friston, K.: *Modes or Models: a Critique on Independent Component Analysis for FMRI.* Trends in Cognitive Sciences **2** (1998), 373–375.

[10] Genovese, C. R.: *A Bayesian Time-Course Model for Functional Magnetic Resonance Imaging Data. With Discussion and a Reply by the Author.* J. Amer. Statist. Assoc. **95** (2000), 691–719.

[11] Giuliani, M.: *Selected Problems in Modelling.* Computer Press, Prague 2005.

[12] Gössl, C., Auer, D. P. and Fahr, L.: *Bayesian Spatiotemporal Inference in Functional Magnetic Resonance Imaging.* Biometrics **57** (2001), 554–562.

[13] Greicius, M. D., Krasnow, B., Reiss, A. L. and Menon, V.: *Functional Connectivity in the Resting Brain: a Network Analysis of the Default Mode Hypothesis.* PNAS **100** (2003), 253–258.

[14] Greicius, M. D. and Menon, V.: *Default-mode Activity during a Passive Sensory Task: Uncoupled from Deactivation but Impacting Activation.* Journal of Cognitive Neuroscience **16** (2004), 1484–1492.

[15] Greicius, M. D., Srivastava, G., Reiss, A. L. and Menon, V.: *Default-mode Network Activity Distinguishes Alzheimer's Disease from Healthy Aging: Evidence from Functional MRI.* PNAS **101** (2004), 4637–4642.

[16] Hartvig, N.: *A Stochastic Geometry Model for Functional Magnetic Resonance Imaging Data.* Scand. J. Statist. **29** (2002), 333–353.

[17] Hochstein, S. and Ahissar, M.: *View from the Top: Hierarchies and Reverse Hierarchies in the Visual System.* Neuron **36** (2002), 791–804.

[18] Houston, W.: *Unexpected Simulation Problem.* Appl. Math. **44** (1999), 267–276.

[19] Jensen, E. B. V. and Thorarinsdottir, T. L.: *A Spatio-temporal Model for FMRI Data - With a View to Resting State Networks.* Submitted.

[20] Lund, T. E., Madsen, K. H., Sidaros, K., Luo, W.-L. and Nichols, T. E.: *Non-white Noise in FMRI: Does Modelling have an Impact?* NeuroImage **29** (2006), 54–66.

[21] McKeown, M. J., Hansen, L. K. and Sejnowski, T. J.: *Independent Component Analysis of Functional MRI: What is Signal and What is Noise?* Current Opinion in Neurobiology **13** (2003), 620–629.

[22] Molchanov, I.: *Statistics of the Boolean Model for Practitioners and Mathematicians.* John Wiley & Sons, Chichester (1997).

[23] Møller, J. and Waagepetersen, R. P. : *Statistical Inference and Simulation for Spatial Point Processes.* Chapman & Hall/CRC, New York (2004).

[24] Robert, C.P. and Casella, G: *Monte Carlo Statistical Methods, 2nd Edition.* Springer, New York (2004).

[25] Smith, S. M., Jenkinson, M., Woolrich, M. W., Beckmann, C. F., Behrens, T. E. J., Johansen-Berg, H., Bannister, P. R., De Luca, M., Drobnjak, I., Flitney, D. E., Niazy, R. K., Saunders, J., Vickers, J., Zhang, Y., De Stefano, N., Brady, J. M. and Matthews, P. M.: *Advances in Functional and Structural MR Image Analysis and Implementation as FSL.* NeuroImage **23** (2004), 208–219.

[26] Woolrich, M. W., Jenkinson, M., Brady, J. M. and Smith, S. M.: *Fully Bayesian Spatio-temporal Modeling of FMRI Data.* Transactions of Medical Imaging **23** (2004), 213–231.

P A P E R

C

Bayesian image restoration, using configurations

THORDIS L. THORARINSDOTTIR
University of Aarhus

Abstract

In this paper, we develop a Bayesian procedure for removing noise from images that can be viewed as noisy realisations of random sets in the plane. The procedure utilises recent advances in configuration theory for noise free random sets, where the probabilities of observing the different boundary configurations are expressed in terms of the mean normal measure of the random set. These probabilities are used as prior probabilities in a Bayesian image restoration approach. Estimation of the remaining parameters in the model is outlined for salt and pepper noise. The inference in the model is discussed in detail for 3×3 and 5×5 configurations and examples of the performance of the procedure are given.

1 Introduction

The comparison of neighbouring grid points in a discrete realisation of a random closed set Z in $\mathbb{R}^2$ has been used for decades to make inference on various characteristics of the random set. A classical result, cf. Serra (1982), states that the information obtained by comparing pairs of neighbouring grid points can be used to estimate the mean length of the total projection of the boundary of the random set in directions associated with the digitisation. This, in turn, yields certain information about the directional properties of the boundary. Larger configurations, such as grid squares of size 2×2 or 3×3, were used in Ohser *et al.* (1998) and Ohser and Mücklich (2000) to estimate the area density, length density, and density of the Euler number of Z.

In Jensen and Kiderlen (2003) and Kiderlen and Jensen (2003), the authors use grid squares of size $n \times n$, $n \geq 2$, to estimate the mean normal measure of the random set Z. The knowledge of this can then be used to quantify the anisotropy of Z. Events of type $tB \subset Z$, $tW \subset \mathbb{R}^2 \setminus Z$ are observed, where tB

and tW are finite subsets of the scaled standard grid $t\mathbb{Z}^2$. The probability of such events,

$$\mathbb{P}(tB \subset Z, tW \subset \mathbb{R}^2 \setminus Z),$$

can effectively be estimated by filtering the discrete image. In digitised images, B usually stands for "black" points and W for "white" points. Here, we use the notion point for the mid-point of a pixel in the digitised image. We will not distinguish between a pixel and its mid-point and we use both notions in the following.

Another interesting aspect in the analysis of discrete planar random sets is the restoration of the random set from a noisy image. If the mean normal measure of the random set Z is known, the method in Kiderlen and Jensen (2003) and Jensen and Kiderlen (2003) can be reversed to obtain the prior probabilities for a Bayesian restoration procedure. The fundaments for Bayesian image analysis were developed by Ulf Grenander, see Grenander (1981), while the method itself was developed and popularised mainly by Geman and Geman (1984). For further readings on the subject, see e.g. Winkler (1995).

Hartvig and Jensen (2000a) introduce a spatial mixture modelling approach to the Bayesian image restoration. They consider $n \times n$ neighbourhoods around each pixel in the image, where $n \geq 3$ is an odd number. The prior probability of a certain constellation or pattern to be observed in the neighbourhood then depends on the number of black points in the given configuration. In other words, every two configurations with equal number of black points have the same prior probability. If, however, the restored image represents a random closed set Z that fulfils some regularity conditions and the resolution of the image is "good enough", the following configurations should not have equal prior probabilities:
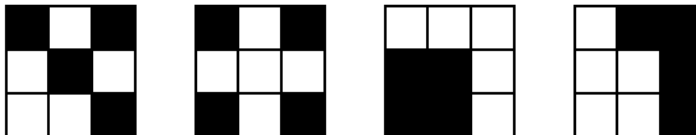
We use the theory from Jensen and Kiderlen (2003) and Kiderlen and Jensen (2003) to specify new prior probabilities for the spatial mixture model of Hartvig and Jensen (2000a). Here, a black and white configuration has a positive prior probability if and only if there exists a line going through the centre of at least two pixels that separates the black and the white points and hits only points of one colour.

The paper is organised as follows. Preliminaries concerning convex geometry, random sets, and image analysis are given in Section 2. The prior probabilities based on configuration theory are presented in Section 3. In

2

Section 4, we specify the posterior probabilities for noisy images and discuss parameter estimation under the model. Three examples are given in Section 5. Finally, there are some concluding remarks in Section 6.

2 Preliminaries

A compact convex subset of $\mathbb{R}^2$ is called a *convex body* and we denote by $\mathcal{K}$ the family of convex bodies in $\mathbb{R}^2$. The *convex ring*, $\mathcal{R}$, is the family of finite unions of convex bodies while the *extended convex ring* is the family of all closed subsets $F \in \mathbb{R}^2$ such that $F \cap K \in \mathcal{R}$ for all $K \in \mathcal{K}$. Further, we denote by $L(K, \cdot)$ the *normal measure of $K \in \mathcal{R}$* on the unit circle S^1. For a Borel set $A \in \mathcal{B}(S^1)$, $L(K, A)$ is the length of the part of the boundary of K with outer normal in A. L is thus a Borel measure on S^1 and the total mass $L(K, S^1)$ is just the boundary length $L(K)$ of K. The normal measure is sometimes called the first surface area measure and then denoted by $S^1(K, \cdot)$, cf. Schneider (1993, p. 214-218).

Now, let Z be a stationary random set in $\mathbb{R}^2$ with values in the extended convex ring. We assume in the following that Z satisfies the integrability condition

$$\mathbb{E} 2^{N(Z \cap K)} < +\infty \qquad (1)$$

for all $K \in \mathcal{K}$. Here, $N(U)$ is the minimal $k \in \mathbb{N}$ such that $U = \cup_{i=1}^{k} K_i$ with $K_i \in \mathcal{K}$ if $U \neq \emptyset$ and $N(\emptyset) = 0$. This condition is stricter than most standard integrability conditions, but it guarantees that the realisations of Z do not become too complex in structure. The *mean normal measure* of Z is defined by

$$\bar{L}(Z, \cdot) = \lim_{r \to +\infty} \frac{\mathbb{E} L(Z \cap rK, \cdot)}{\nu_2(rK)},$$

where ν_2 is the Lebesgue measure on $\mathbb{R}^2$. See e.g. Schneider and Weil (2000) for more details.

A digitisation (or discretisation) of Z is the intersection of Z with a scaled lattice. For a fixed scaling factor $t > 0$, we consider $Z \cap t\mathbb{L}$, where

$$\mathbb{L} := \mathbb{Z}^2 = \{(i, j) : i, j \in \mathbb{Z}\}$$

is the usual lattice of points with integer coordinates. The lattice square

$$\mathbb{L}_n := \left\{ (i, j) : i, j = -\frac{n-1}{2}, \dots, \frac{n-1}{2} \right\}$$

consists of n^2 points ($n \geq 3, n$ odd). Here, we follow the notation in Hartvig and Jensen (2000a) and place the lattice square around a centre pixel. As we only consider lattice squares with odd number of points, this should not cause

3

any conflicts in the notation. A line passing through at least two points of $\mathbb{L}_n$ will be called an *n-lattice line*.

Let $X \subset t\mathbb{Z}^2$ be a finite set and $t > 0$. A binary image on X is a function $f : X \to \{0, 1\}$. Here, f is given by $f(x) = \mathbb{1}\{x \in Z \cap X\}$ so that f is a random function due to the randomness of the set Z. We call a certain pattern of the values of f on a $n \times n$ grid a *configuration*. We denote it by C_t^n, where $t > 0$ is the resolution of the grid, as in the definition of a lattice above. The elements of the configuration are numbered to match the numbering of the elements in the lattice square $\mathbb{L}_n$. For $n = 3$ this gives

$$C_t^3 = \begin{bmatrix} c_{-1,1} & c_{0,1} & c_{1,1} \\ c_{-1,0} & c_{0,0} & c_{1,0} \\ c_{-1,-1} & c_{0,-1} & c_{1,-1} \end{bmatrix}_t,$$

and similarly for other allowed values of n. If the size of the configuration is clear from the context, we will omit the index n. Examples of 3×3 configurations are

$$\begin{bmatrix} \bullet & \circ & \circ \\ \bullet & \bullet & \circ \\ \bullet & \bullet & \circ \end{bmatrix}_t, \quad \begin{bmatrix} \circ & \circ & \circ \\ \bullet & \circ & \bullet \\ \bullet & \bullet & \circ \end{bmatrix}_t, \quad \begin{bmatrix} \circ & \bullet & \bullet \\ \bullet & \circ & \bullet \\ \bullet & \bullet & \circ \end{bmatrix}_t$$

where $\bullet$ means that $f(x) = 1$ or equivalently $z \cap \{x\} \neq \emptyset$, while $\circ$ means that $f(x) = 0$ or equivalently $z \cap \{x\} = \emptyset$. Here, z is the realisation of the random set Z observed in the image f.

3 Configuration probabilities

Let $f : X \to \{0, 1\}$ be an image as before and let Z be a stationary random set that fulfils (1). In Kiderlen and Jensen (2003), the authors show that for $n > 0$, a given $x \in X$, and a given configuration C_t,

$$\lim_{t \to 0^+} \frac{1}{t} \mathbb{P}\big(Z \cap t(\mathbb{L}_n + x) = C_t\big) = \int_{S^1} h(-v) \bar{L}(Z, dv). \tag{2}$$

The function h is given by

$$h(\cdot) = \big[\min_{x \in B}\langle x, \cdot\rangle - \max_{x \in W}\langle x, \cdot\rangle\big]^+,$$

where $(tB, tW) = C_t$ is the partitioning of the configuration C_t in "black" and "white" points, that is, $tB \subset Z$ and $tW \subset \mathbb{R}^2 \setminus Z$. Here, $g^+ := \max\{g, 0\}$ denotes the positive part of the function g and $\langle x, y\rangle$ denotes the usual inner product of the vectors x and y. A configuration C_t with non-identically zero h is called an *informative configuration*. C_t is informative if and only if there exists a n-lattice line separating tB and tW not hitting both of them. More precisely, $C_t = (tB, tW)$ is informative if and only if there exists an n-lattice

line g such that tB is on one side of g, tW is on the other side of g and all the lattice points on g are either all black or all white.

Furthermore, it is shown in Jensen and Kiderlen (2003) that for a given informative configuration C_t, there exist vectors $a, b \in \mathbb{R}^2$ such that

$$h(-v) = \min\{\langle a, v\rangle^+, \langle b, v\rangle^+\}$$

for all $v \in S^1$. These results are then used to obtain estimators for the mean normal measure $\bar{L}(Z, \cdot)$ based on observed frequencies of the different types of configurations. If we, on the other hand, assume we have a discrete noisy image in $\mathbb{R}^2$, where the underlying image is a realisation of a stationary random closed set Z with a known mean normal measure $L(Z, \cdot)$, (2) provides prior probabilities in a Bayesian restoration procedure.

As an example, let us assume that Z is isotropic. Then, the mean normal measure $\bar{L}(Z, \cdot)$ is, up to a positive constant of proportionality, the Lebesgue measure on $[0, 2\pi)$. Equation (2) thus becomes

$$\lim_{t \to 0^+} \frac{1}{t} \mathbb{P}\big(Z \cap t(\mathbb{L}_n + x) = C_t\big)$$
$$= k \int_0^{2\pi} \min\big\{\langle a, (\cos\theta, \sin\theta)\rangle^+, \langle b, (\cos\theta, \sin\theta)\rangle^+\big\} d\theta, \qquad (3)$$

where $k > 0$ is a constant. For $t > 0$ small enough, such that only informative, all black, and all white configurations have positive probability, this gives the marginal probability of each informative configurations up to a constant of proportionality.

For $n = 3$, the vectors a and b are given in Jensen and Kiderlen (2003). We can thus insert those values without further effort into the right hand side of (3). For $x \in X$, this gives

$$\mathbb{P}\big(Z \cap (t\mathbb{L}_3 + x) = C_t\big) = \begin{cases} p_0, & C_t = \begin{bmatrix} \circ & \circ & \circ \\ \circ & \circ & \circ \\ \circ & \circ & \circ \end{bmatrix}_t \\ p_1, & C_t = \begin{bmatrix} \bullet & \bullet & \bullet \\ \bullet & \bullet & \bullet \\ \bullet & \bullet & \bullet \end{bmatrix}_t \\ p_2, & C_t \in R\left(\begin{bmatrix} \bullet & \circ & \circ \\ \bullet & \circ & \circ \\ \bullet & \circ & \circ \end{bmatrix}_t, \begin{bmatrix} \bullet & \bullet & \circ \\ \bullet & \bullet & \circ \\ \bullet & \bullet & \circ \end{bmatrix}_t\right) \\ p_3, & C_t \in R\left(\begin{bmatrix} \circ & \circ & \circ \\ \bullet & \circ & \circ \\ \bullet & \bullet & \circ \end{bmatrix}_t, \begin{bmatrix} \bullet & \bullet & \circ \\ \bullet & \bullet & \bullet \\ \bullet & \bullet & \bullet \end{bmatrix}_t\right) \\ p_4, & C_t \in R\left(\begin{bmatrix} \bullet & \bullet & \bullet \\ \bullet & \bullet & \bullet \\ \bullet & \bullet & \bullet \end{bmatrix}_t, \begin{bmatrix} \circ & \circ & \circ \\ \bullet & \circ & \circ \\ \bullet & \bullet & \circ \end{bmatrix}_t\right) \\ p_5, & C_t \in R\left(\begin{bmatrix} \bullet & \circ & \circ \\ \bullet & \circ & \circ \\ \bullet & \bullet & \circ \end{bmatrix}_t, \begin{bmatrix} \bullet & \bullet & \circ \\ \bullet & \bullet & \circ \\ \bullet & \bullet & \circ \end{bmatrix}_t, \begin{bmatrix} \bullet & \bullet & \circ \\ \bullet & \bullet & \bullet \\ \bullet & \bullet & \bullet \end{bmatrix}_t, \begin{bmatrix} \circ & \circ & \circ \\ \bullet & \circ & \circ \\ \circ & \circ & \circ \end{bmatrix}_t\right) \\ 0, & \text{otherwise,} \end{cases}$$

5

where $R(\cdot)$ is the set of all possible rotations and reflections. The probabilities $p_2, \ldots, p_5$ are determined from (3) up to a multiplicative constant c. They are given by

$$
\begin{aligned}
p_2 &= c\big[5\sin(\operatorname{atan}(2)) - 4\big], \\
p_3 &= c\big[5\sin(\operatorname{atan}(2)) - 3\sqrt{2}\big], \\
p_4 &= c\big[2 - \sqrt{2}\big], \\
p_5 &= c\big[1 + \sqrt{2} - \frac{5}{2}\sin(\operatorname{atan}(2))\big].
\end{aligned}
$$

As the total probability is 1, we can express c in terms of the other unknown probabilities,

$$
c = \frac{1 - p_0 - p_1}{16}.
$$

For $n = 5$, we have used the methods described in Jensen and Kiderlen (2003) to determine the informative 5×5 configurations and the vectors a and b for each configuration. We have then calculated the prior probabilities in the same manner as described above for 3×3 configurations. The results from this can be found in Appendix A.

Knowledge of the mean normal measure of Z will not give us information about the probability of observing all white and all black configurations, as the mean normal measure is a property of the boundary of the set. The remaining parameters, p_0 and p_1 must thus be estimated from the data. This problem is treated in the next section.

4   Restoration of a noisy image

Let $F : X \to \{0, 1\}$ be a binary image on a finite set $X \subset t\mathbb{Z}^2$ for $t > 0$ and such that F can be viewed as a realisation of an isotropic stationary random set Z with noise. Note that the randomness in the image F is two-fold. First, the noise free image is random due to the randomness of the set Z. Second, a random noise is added to the image. By Bayes rule we have, for $x \in X$ and a given configuration C_t,

$$
\mathbb{P}\big(Z \cap (t\mathbb{L}_n + x) = C_t | F(t\mathbb{L}_n + x)\big)
$$
$$
\propto \mathbb{P}\big(Z \cap (t\mathbb{L}_n + x) = C_t\big) p\big(F(t\mathbb{L}_n + x) | Z \cap (t\mathbb{L}_n + x) = C_t\big).
$$

We assume that $F(x_i)$ and $F(x_j)$ are conditionally independent given Z for all $x_i, x_j \in X$, and that the conditional distribution of $F(x)$ given Z only depends on $Z \cap x$ for all $x \in X$. Under these conditions, we get

$$
p\big(F(t\mathbb{L}_n + x) | Z \cap (t\mathbb{L}_n + x) = C_t\big) = \prod_{k=1}^{n^2} p\big(F(y_k) | Z \cap \{y_k\} = \{c_k\}\big),
$$

where $\{y_k\}_{k=1}^{n^2} = t\mathbb{L}_n + x$ and $\{c_k\}_{k=1}^{n^2} = C_t$.

By summing over the neighbouring states, we obtain the probability of Z hitting a single point $x \in X$,

$$\mathbb{P}\big(Z \cap \{x\} \neq \emptyset | F(t\mathbb{L}_n + x)\big)$$

$$\propto \sum_{\{C_t : c_{00} = \bullet\}} \mathbb{P}\big(Z \cap (t\mathbb{L}_n + x) = C_t\big) \prod_{k=1}^{n^2} p\big(F(y_k) | Z \cap \{y_k\} = \{c_k\}\big) \quad (4)$$

$$=: S_1(x).$$

The probability of Z not hitting a single point $x \in X$ is obtained in a similar way. It is given by

$$\mathbb{P}\big(Z \cap \{x\} = \emptyset | F(t\mathbb{L}_n + x)\big)$$

$$\propto \sum_{\{C_t : c_{00} = \circ\}} \mathbb{P}\big(Z \cap (t\mathbb{L}_n + x) = C_t\big) \prod_{k=1}^{n^2} p\big(F(y_k) | Z \cap \{y_k\} = \{c_k\}\big) \quad (5)$$

$$=: S_2(x).$$

As the probabilities in (4) and (5) sum to one, we only need to compare $S_1(x)$ and $S_2(x)$ for determining the restored value of the image for a pixel x. The restored value is 1 if $S_1(x) > S_2(x)$ and 0 otherwise.

To compare $S_1(x)$ and $S_2(x)$, we need to determine the densities $p\big(F(x) | Z \cap \{x\}\big)$ which depend on the distribution of the noise. As an example, we consider salt and pepper noise. That is, a black point is replaced by a white point with probability q, and vice versa. More precisely,

$$p\big(F(x) | Z \cap \{x\}\big) = q^{F(x)} (1 - q)^{1 - F(x)} \mathbb{1}\big\{Z \cap \{x\} = \emptyset\big\}$$
$$+ (1 - q)^{F(x)} q^{1 - F(x)} \mathbb{1}\big\{Z \cap \{x\} \neq \emptyset\big\},$$

for some $0 \leq q \leq 1$. This noise model has one unknown parameter, q, which must be estimated from the data.

Further, we need to determine the marginal probability $\mathbb{P}\big(Z \cap (t\mathbb{L}_n + x) = C_t\big)$ of observing a given configuration, C_t. A method to obtain the prior probabilities of observing the different types of boundary configurations, that is configurations that contain both black and white points, is given in the previous section. We still lack information about the prior probabilities of observing configurations that are all black or all white, that is

$$p_0 = \mathbb{P}\Big(Z \cap (t\mathbb{L}_3 + x) = \Big[\begin{smallmatrix} \circ & \circ & \circ \\ \circ & \circ & \circ \\ \circ & \circ & \circ \end{smallmatrix}\Big]_t\Big)$$

and

$$p_1 = \mathbb{P}\Big(Z \cap (t\mathbb{L}_3 + x) = \Big[\begin{smallmatrix} \bullet & \bullet & \bullet \\ \bullet & \bullet & \bullet \\ \bullet & \bullet & \bullet \end{smallmatrix}\Big]_t\Big)$$

7

if $n = 3$ and similarly for larger n.

We use the parameter estimation approach introduced in Hartvig and Jensen (2000a) which is related to maximum likelihood estimation. Within the model, we can calculate the marginal density of an $n \times n$ neighbourhood. It is given by

$$
\begin{aligned}
p\big(&F(t\mathbb{L}_n + x); p_0, p_1, q\big) \\
&= \sum_{C_t} p\big(F(t\mathbb{L}_n + x)|Z \cap (t\mathbb{L}_n + x) = C_t; q\big) \mathbb{P}\big(Z \cap (t\mathbb{L}_n + x) = C_t; p_0, p_1\big) \\
&= p_0 q^{\sum F(y_k)} (1-q)^{n^2 - \sum F(y_k)} + p_1 q^{n^2 - \sum F(y_k)} (1-q)^{\sum F(y_k)} \\
&\quad + \frac{1 - p_0 - p_1}{A(n)} \sum_{C_t \text{ inform.}} B(C_t) \prod_{k=1}^{n^2} \big[q^{F(y_k)} (1-q)^{1-F(y_k)} \mathbb{1}\{Z \cap \{y_k\} = \emptyset\} \\
&\qquad\qquad\qquad\qquad\qquad\qquad + q^{1-F(y_k)} (1-q)^{F(y_k)} \mathbb{1}\{Z \cap \{y_k\} \neq \emptyset\} \big],
\end{aligned}
$$

where the constant $B(C_t)$ is given by the integral on the right hand side of (3) and $A(n) = \sum_{C_t \text{ inform.}} B(C_t)$. We have $A(3) = 16$ and $A(5) = 32$.

A possibility for estimating the parameters p_0, p_1, and q is to maximise the contrast function

$$
\gamma(p_0, p_1, q) = \sum_{x \in X} \log p\big(F(t\mathbb{L}_n + x); p_0, p_1, q\big). \tag{6}
$$

This is, however, computationally a very demanding task. We have therefore used a simplified version of the approach. The probability that a single point $x \in X$ is in the set Z is

$$
\begin{aligned}
\mathbb{P}\big(Z \cap \{x\} \neq \emptyset\big) &= \sum_{\{C_t : c_{00} = \bullet\}} \mathbb{P}\big(Z \cap (t\mathbb{L}_n + x) = C_t\big) \\
&= \frac{1 - p_0 - p_1}{2} + p_1 \\
&= \frac{1 - p_0 + p_1}{2},
\end{aligned}
$$

as exactly half of the boundary configurations have a black mid-point. The marginal density of a single point is thus given by

$$
\begin{aligned}
p\big(&F(x); p_0, p_1, q\big) \\
&= \mathbb{P}\big(Z \cap \{x\} \neq \emptyset; p_0, p_1\big) p\big(F(x)|Z \cap \{x\} \neq \emptyset; q\big) \\
&\quad + \mathbb{P}\big(Z \cap \{x\} = \emptyset; p_0, p_1\big) p\big(F(x)|Z \cap \{x\} = \emptyset; q\big) \\
&= \frac{1}{2} \Big[(1 - p_0 + p_1) q^{1-F(x)} (1-q)^{F(x)} + (1 + p_0 - p_1) q^{F(x)} (1-q)^{1-F(x)} \Big].
\end{aligned}
$$

The corresponding contrast function

$$\gamma_m(p_0, p_1, q) = \sum_{x \in X} \log p\big(F(x); p_0, p_1, q\big),$$

can easily be differentiated with repect to the parameters p_0, p_1, and q. The differentiation yields that the maximum of γ_m is obtained when

$$p_1 = p_0 + \frac{2 \sum F(x) - |X|}{|X|(1 - 2q)},$$

where $|X|$ denotes the number of points in X. In the examples in Section 5, we have inserted this into (6) and maximised γ on a grid with $q \in [0.05, 0.1, \ldots, 0.45, 0.49]$ and $p_0 \in [0.05, 0.1, \ldots, 0.9]$ under the constraints

$$2p_0 + \frac{2 \sum F(x) - |X|}{|X|(1 - 2q)} < 1, \qquad p_0 + \frac{2 \sum F(x) - |X|}{|X|(1 - 2q)} \geq 0.$$

5 Examples

We illustrate the method by applying it to two synthetic datasets and one real data set. We use the salt and pepper noise model and isotropic priors for the configuration probabilities in all three examples. The method can not be used directly to restore the values on the edge of an image. In the examples below, we have therefore a one-pixel-wide edge of white (background) pixels in each restored image for $n = 3$ and a two-pixel-wide edge of white pixels in each restored image for $n = 5$. Another possibility here would be to add either a one-pixel-wide boundary of white pixels for $n = 3$, or a two-pixel-wide boundary of white pixels for $n = 5$, around the noisy image before restoration. This will, however, lead to a slight underestimate of black pixels on the edge. We will quantify the results by the classification error. The classification error is estimated as the percentage of misclassified pixels (either type I or type II errors). The results given for the classification error are based on those pixels from the interior of each image where there are no edge effects.

Example 1 (Boolean model with isotropic grains)**.** The first example is based on digitisation of a simulated Boolean model, see Schneider and Weil (2000). Boolean models are widely used as simple geometric models for random sets. The simulation of a Boolean model is a two-step procedure. First, independent uniform points are simulated in a sampling window. Second, a random grain is attached to each point. The grains are independent from one another and from the points. In order to avoid edge effects, the sampling window must be larger than the target window. Here, the target window is the unit square

and the grains are circular discs with random radii. The radius of each grain is a uniform number from the interval $[0.0375, 0.15]$. Figure 1 (left) shows a realisation of this model. We have then digitised the image with $t = 0.01$ which gives a resolution of 100×100. The digitised image is shown in Figure 1 (right).
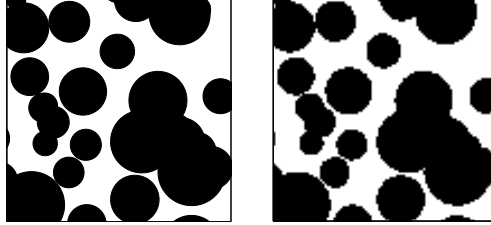
Figure 1: Boolean model with circular grains. Left: a realisation of the model on the unit square. Right: a digitised image of the realisation with resolution 100×100.

The digitised realisation of the Boolean model from Figure 1 (right) is now our original image. We have added salt and pepper noise to it for three different values of the noise parameter q. The noisy images are shown in Figure 2 (top row). In the leftmost image we have $q = 0.25$, in the middle image $q = 0.33$, and in the rightmost image $q = 0.4$. We have restored the original image from the noisy images using both 3×3 configurations and 5×5 configurations as described in the previous section. The resulting images for 3×3 configurations are shown in the middle row of Figure 2 and the resulting images for 5×5 configurations are shown in the bottom row of Figure 2. The parameter estimates and the classification errors for the restoration are given in Table 1.

Table 1: Parameter estimates, true parameter values, and classification errors for the restoration of a Boolean model with isotropic grains. The parameter estimates are based on five independent simulations of the degraded image. The standard errors of the estimates are given in parentheses. The classification errors are given in percentage.

$n \times n$	q	$\hat{q}$	p_0	$\hat{p}_0$	p_1	$\hat{p}_1$	Class. error
3×3	0.25	0.25(0)	0.30	0.31(0.02)	0.45	0.45(0.01)	8.98(0.55)
5×5	0.25	0.25(0)	0.20	0.21(0.02)	0.35	0.35(0.01)	5.11(0.39)
3×3	0.33	0.32(0.03)	0.30	0.33(0.08)	0.45	0.48(0.10)	17.79(0.01)
5×5	0.33	0.33(0.03)	0.20	0.22(0.07)	0.35	0.37(0.09)	10.61(0.32)
3×3	0.40	0.40(0)	0.30	0.31(0.08)	0.45	0.45(0.06)	29.19(0.77)
5×5	0.40	0.40(0)	0.20	0.22(0.06)	0.35	0.36(0.05)	21.20(1.02)
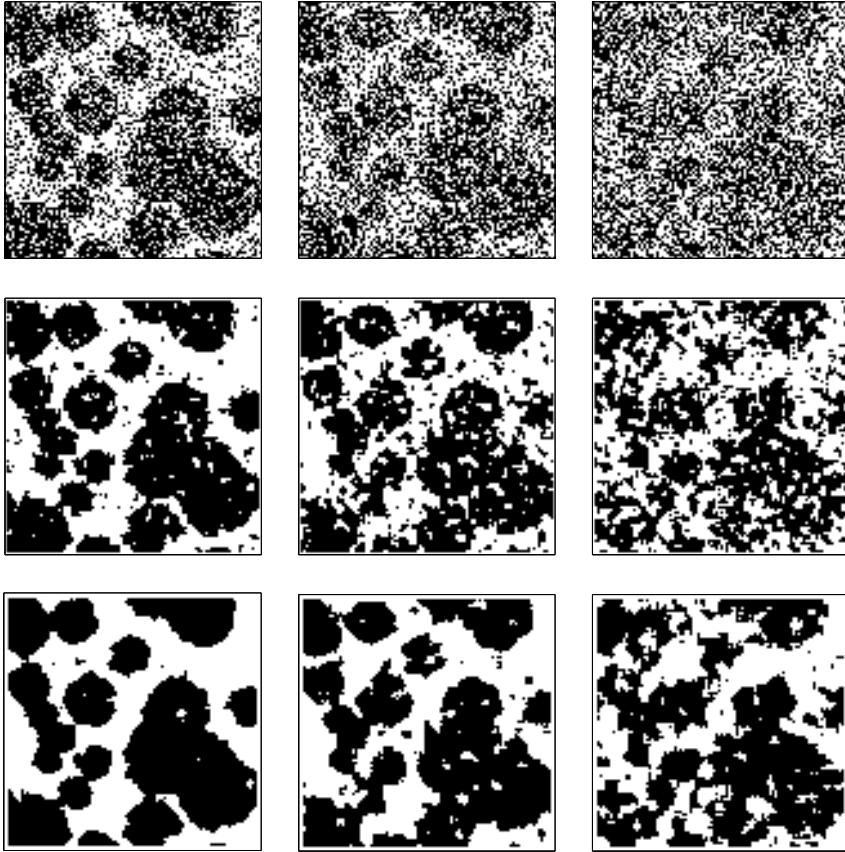
Figure 2: Restoration of the digitised realisation of the Boolean model with isotropic grains. Top row: the original image disturbed with salt and pepper noise for q equal to $0.25, 0.33$, and 0.4. Middle row: estimates of the true image using 3×3 configurations. Bottom row: estimates of the true image using 5×5 configurations.

Example 2 (Boolean model with non-isotropic grains)**.** The grains in the Boolean model are here the right half of circular discs with random radii. The radius of each grain is a uniform number from the interval $[0.0375, 0.15]$ and the target window is again the unit square. A realisation of this model is shown in Figure 3 (left). As before, we have digitised the image with $t = 0.01$ which gives a resolution of 100×100. The digitised image is shown in Figure 3 (right). We have proceeded exactly as in the previous example. The noisy images are shown in Figure 4 (top row). In the leftmost image we have $q = 0.25$, in the middle image $q = 0.33$, and in rightmost image $q = 0.4$. The restored images for 3×3 configurations are shown in the middle row of Figure 4 and the restored images for 5×5 configurations are shown in the bottom row of Figure 4. Further, Table 2 shows the parameter estimates and the classification errors

for the restoration.
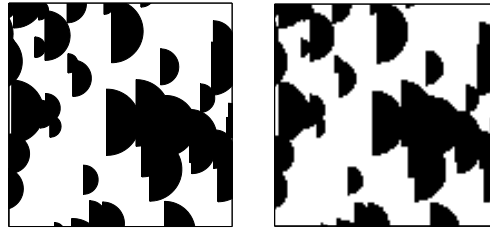
Figure 3: Boolean model with non-isotropic grains. Left: a realisation of the model on the unit square. Right: a digitised image of the realisation with resolution 100×100.
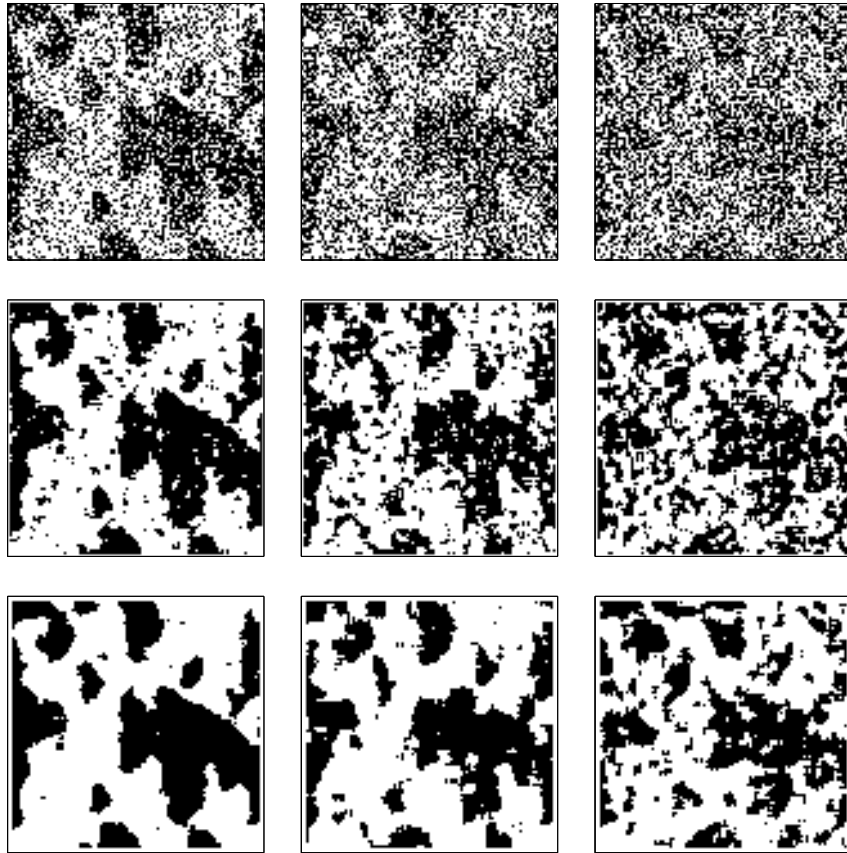

Figure 4: Restoration of the digitised realisation of the non-isotropic Boolean model. Top row: the original image disturbed with salt and pepper noise for q equal to $0.25, 0.33$, and 0.4. Middle row: estimates of the true image using 3×3 configurations. Bottom row: estimates of the true image using 5×5 configurations.

Table 2: Parameter estimates, the true parameter values, and classification errors for the restoration of the non-isotropic Boolean model. The parameter estimates are based on five independent simulations of the degraded image. The standard errors of the estimates are given in parentheses. The classification errors are given in percentage.

$n \times n$	q	$\hat{q}$	p_0	$\hat{p}_0$	p_1	$\hat{p}_1$	Class. error
3×3	0.25	0.25(0)	0.48	0.47(0.03)	0.31	0.30(0.03)	9.03(0.15)
5×5	0.25	0.25(0)	0.39	0.39(0.02)	0.22	0.22(0.01)	5.05(0.29)
3×3	0.33	0.35(0)	0.48	0.55(0)	0.31	0.36(0.02)	18.27(0.88)
5×5	0.33	0.35(0)	0.39	0.44(0.02)	0.22	0.25(0.03)	10.72(0.60)
3×3	0.40	0.40(0)	0.48	0.48(0.03)	0.31	0.35(0.04)	29.06(0.52)
5×5	0.40	0.40(0)	0.39	0.36(0.04)	0.22	0.23(0.04)	20.62(0.74)

Example 3 (Image from steel data). Our last example is an image showing the micro-structure of steel. The image is from Ohser and Mücklich (2000), where it has been analysed to estimate the mean normal measure, see also Jensen and Kiderlen (2003). The thresholded, binary image of the data is shown in Figure 5. We have used Otsu's method for the thresholding. This method minimises the intraclass variance of the black and the white pixels, see Otsu (1979). The resolution of the image is 896×1280 pixels.
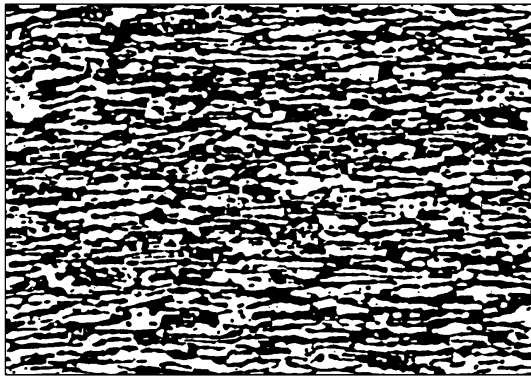
Figure 5: Binary image of rolled stainless steel in a longitudinal section. The light phase is ferrite, the black phase is austenite. From Osher and Mücklich (2000).

We have added salt and pepper noise to the binary image for $q = 0.25$ and $q = 0.33$. The noisy images can be seen in Figure 6 (top row). We have used the method described in the previous section for the restoration of the noisy images, using isotropic priors for the informative configurations. The

resulting images can be seen in Figure 6 (middle row) for 3×3 configurations and in Figure 6 (bottom row) for 5×5 configurations. Further, the parameter estimates and the classification errors for the estimates are shown in Table 3.
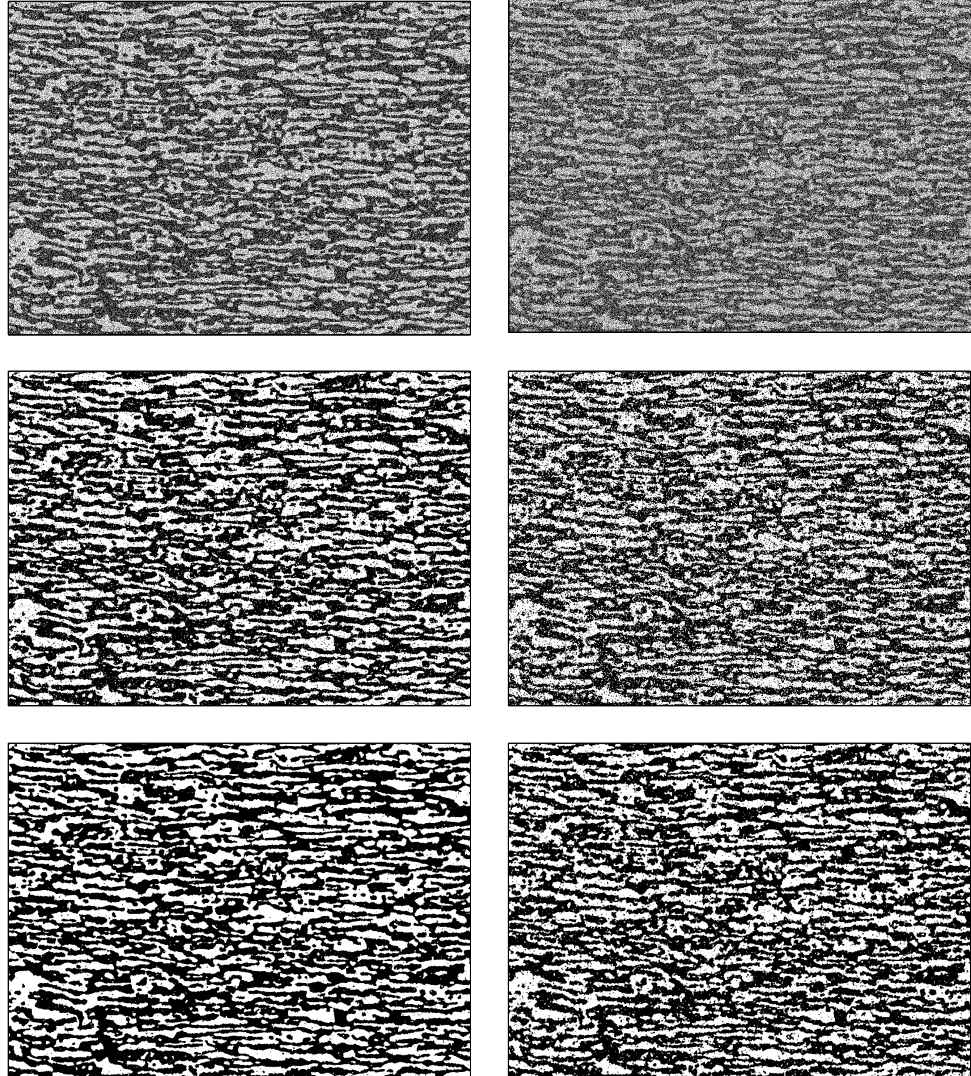
Figure 6: Restoration of the steel data image. Top row: the original binary image disturbed with salt and pepper noise for $q = 0.25$ (left) and $q = 0.33$ (right). Middle row: estimates of the true image using 3×3 configurations. Bottom row: estimates of the true image using 5×5 configurations.

Table 3: Parameter estimates, the true parameter values, and classification errors for the restoration of the steel data image. The parameter estimates are based on five independent simulations of the degraded image. The standard errors of the estimates are given in parentheses. The classification errors are given in percentage.

$n \times n$	q	$\hat{q}$	p_0	$\hat{p}_0$	p_1	$\hat{p}_1$	Class. error
3×3	0.25	0.25(0)	0.34	0.35(0)	0.45	0.46(0.002)	8.92(0.03)
5×5	0.25	0.25(0)	0.25	0.25(0)	0.35	0.36(0.002)	4.90(0.03)
3×3	0.33	0.35(0)	0.34	0.40(0)	0.45	0.53(0.003)	17.74(0.03)
5×5	0.33	0.35(0)	0.25	0.30(0)	0.35	0.43(0.003)	10.71(0.05)

6   Discussion

In the two first examples we have images of a similar type, the only difference is the mean normal measure of the boundary of the objects. In Example 1, the grains have isotropic boundaries which means that the model is using the correct prior probabilities for the configurations. In Example 2, on the other hand, there are some configurations that have much higher probability than suggested in the prior. The configurations

$$\begin{bmatrix} \circ & \bullet & \bullet \\ \circ & \bullet & \bullet \\ \circ & \bullet & \bullet \end{bmatrix}_t \text{ and } \begin{bmatrix} \circ & \circ & \bullet \\ \circ & \circ & \bullet \\ \circ & \circ & \bullet \end{bmatrix}_t$$

are, for instance, more likely to occur in the image than the configurations

$$\begin{bmatrix} \circ & \circ & \circ \\ \bullet & \bullet & \bullet \\ \bullet & \bullet & \bullet \end{bmatrix}_t \text{ and } \begin{bmatrix} \circ & \circ & \circ \\ \circ & \circ & \circ \\ \bullet & \bullet & \bullet \end{bmatrix}_t .$$

According to the isotropic prior, however, these configurations are all equaly likely to occur. If we compare the results in Table 1 and Table 2, we see that the classification error in Example 2 is very similar to the classification error in Example 1 for the same amount of noise and the same type of model. This suggests that it is not necessary to know the mean normal measure of the boundary of the object precisely for our model to perform in a close to optimal way.

It is also clear from the results in the previous section that the model using 5×5 configurations is superior to the model using 3×3 configurations. This is not surprising since the true images are quite regular with large patches of either black or white pixels. One might suspect that the model using 3×3 configurations would be more appropriate for images where the object Z consists of relatively small, disconnected components. Another consideration here is whether it is of interest to consider larger configurations than 5×5 configurations. As one can see from Appendix A, the model is already quite

complicated if we use 5×5 configurations. We think, therefore, that it is computationally not feasible to consider larger configurations. Further, and maybe more importantly, very large configurations will tend to remove any finer details in the original image.

The model presented in this paper is very local in nature. The estimated restored value in a given pixel only depends on the image values in a small neighbourhood around that pixel. For this reason, there is no obvious way how to derive the joint posterior distribution over the entire image from the posterior distribution of the marginals in the small neighbourhoods and it is the former that is needed for estimating the unknown global parameters in the model. We have chosen to use the contrast function from Hartvig and Jensen (2000a), as this seems a sensible choice with a close relation to maximum likelihood estimation. As noted in Woolrich *et al.* (2005), the difference between the parameter estimates using this contrast function and those that could be obtained if the joint posterior were available is not known. Our method seems, however, not very sensitive towards small changes in the parameter estimates. We can also see from Table 1 - 3 that we get fairly good parameter estimates by maximising the contrast function if the noise in the image is moderate, especially for the larger image in Example 3. For higher levels of noise, the accuracy in the parameter estimates seems to depend on the accuracy of the prior for the informative configurations. Furthermore, note that the noise parameter q is estimated very accurately if the correct value of the parameter is available on the grid. The accuracy of the remaining estimates of the prior probabilities of all black and all white configurations, p_0 and p_1, depends on how well the noise parameter is estimated. It might therefore be of interest to use a finer grid for the estimation of q.

Acknowledgements

A Informative 5×5 configurations

Using the methods described in Jensen and Kiderlen (2003), we have constructed all informative 5×5 configurations and calculated the vectors a and b which are needed for the calculation of the prior probabilities of the configurations, see Section 3. The results are given in Table 4. We have omitted both the index for the resolution of the grid and the index for the size of the configuration to save space in the table.

In the examples in Section 5, we have used an isotropic prior for the boundary configurations. For $x \in X$, the prior probabilities for 5×5 configurations are in this case given by

$$
\mathbb{P}\big(Z \cap (t\mathbb{L}_5 + x) = C_t\big) =
\begin{cases}
p_0, & C_t = \begin{bmatrix} \circ\,\circ\,\circ\,\circ\,\circ \\ \circ\,\circ\,\circ\,\circ\,\circ \\ \circ\,\circ\,\circ\,\circ\,\circ \\ \circ\,\circ\,\circ\,\circ\,\circ \\ \circ\,\circ\,\circ\,\circ\,\circ \end{bmatrix}_t \\[1.2em]
p_1, & C_t = \begin{bmatrix} \bullet\,\bullet\,\bullet\,\bullet\,\bullet \\ \bullet\,\bullet\,\bullet\,\bullet\,\bullet \\ \bullet\,\bullet\,\bullet\,\bullet\,\bullet \\ \bullet\,\bullet\,\bullet\,\bullet\,\bullet \\ \bullet\,\bullet\,\bullet\,\bullet\,\bullet \end{bmatrix}_t \\[1.2em]
p_2, & C_t \text{ in group nr. } 1, \ldots, 4 \\
p_3, & C_t \text{ in group nr. } 5, \ldots, 8 \\
p_4, & C_t \text{ in group nr. } 9, \ldots, 12 \\
p_5, & C_t \text{ in group nr. } 13, \ldots, 20 \\
p_6, & C_t \text{ in group nr. } 21, \ldots, 24 \\
p_7, & C_t \text{ in group nr. } 25, \ldots, 32 \\
p_8, & C_t \text{ in group nr. } 33, \ldots, 36 \\
p_9, & C_t \text{ in group nr. } 37, \ldots, 44 \\
p_{10}, & C_t \text{ in group nr. } 45, \ldots, 52 \\
p_{11}, & C_t \text{ in group nr. } 53, \ldots, 60 \\
p_{12}, & C_t \text{ in group nr. } 61, \ldots, 68 \\
p_{13}, & C_t \text{ in group nr. } 69, \ldots, 76 \\
p_{14}, & C_t \text{ in group nr. } 77, \ldots, 84 \\
p_{15}, & C_t \text{ in group nr. } 85, \ldots, 92 \\
0, & \text{otherwise.}
\end{cases}
$$

The prior probabilities for the informative configurations are ordered in a decreasing order. They can be calculated up to a multiplicative constant c by inserting the vectors a and b in Table 4 into the right hand side of (3). The unknown constant c can be expressed in terms of p_0 and p_1 by

$$
c = \frac{1 - p_0 - p_1}{32}.
$$

Table 4: The 92 groups of informative 5×5 configurations.

No.	Config.	Twin	Config.	Twin	a	b
1					$\begin{pmatrix}1\\0\end{pmatrix}$	$\begin{pmatrix}0\\-1\end{pmatrix}$
2					$\begin{pmatrix}0\\-1\end{pmatrix}$	$\begin{pmatrix}-1\\0\end{pmatrix}$
3					$\begin{pmatrix}0\\1\end{pmatrix}$	$\begin{pmatrix}-1\\0\end{pmatrix}$
4					$\begin{pmatrix}1\\0\end{pmatrix}$	$\begin{pmatrix}0\\1\end{pmatrix}$
5					$\begin{pmatrix}1\\4\end{pmatrix}$	$\begin{pmatrix}1\\-4\end{pmatrix}$
6					$\begin{pmatrix}4\\-1\end{pmatrix}$	$\begin{pmatrix}-4\\-1\end{pmatrix}$
7					$\begin{pmatrix}-1\\4\end{pmatrix}$	$\begin{pmatrix}-1\\-4\end{pmatrix}$
8					$\begin{pmatrix}4\\1\end{pmatrix}$	$\begin{pmatrix}-4\\1\end{pmatrix}$
9					$\begin{pmatrix}2\\1\end{pmatrix}$	$\begin{pmatrix}-1\\-2\end{pmatrix}$
10					$\begin{pmatrix}1\\-2\end{pmatrix}$	$\begin{pmatrix}-2\\1\end{pmatrix}$
11					$\begin{pmatrix}1\\2\end{pmatrix}$	$\begin{pmatrix}-2\\-1\end{pmatrix}$
12					$\begin{pmatrix}2\\-1\end{pmatrix}$	$\begin{pmatrix}-1\\2\end{pmatrix}$
13					$\begin{pmatrix}1\\1\end{pmatrix}$	$\begin{pmatrix}0\\-1\end{pmatrix}$
14					$\begin{pmatrix}1\\0\end{pmatrix}$	$\begin{pmatrix}-1\\-1\end{pmatrix}$
15					$\begin{pmatrix}1\\-1\end{pmatrix}$	$\begin{pmatrix}-1\\0\end{pmatrix}$

Table 4: The 92 groups of informative 5×5 configurations (continued).

No.	Config.	Twin	Config.	Twin	a	b
16					$\begin{pmatrix} 0 \\ -1 \end{pmatrix}$	$\begin{pmatrix} -1 \\ 1 \end{pmatrix}$
17					$\begin{pmatrix} 0 \\ 1 \end{pmatrix}$	$\begin{pmatrix} -1 \\ -1 \end{pmatrix}$
18					$\begin{pmatrix} 1 \\ 1 \end{pmatrix}$	$\begin{pmatrix} -1 \\ 0 \end{pmatrix}$
19					$\begin{pmatrix} 1 \\ 0 \end{pmatrix}$	$\begin{pmatrix} -1 \\ 1 \end{pmatrix}$
20					$\begin{pmatrix} 1 \\ -1 \end{pmatrix}$	$\begin{pmatrix} 0 \\ 1 \end{pmatrix}$
21					$\begin{pmatrix} 3 \\ 2 \end{pmatrix}$	$\begin{pmatrix} -2 \\ -3 \end{pmatrix}$
22					$\begin{pmatrix} 2 \\ -3 \end{pmatrix}$	$\begin{pmatrix} -3 \\ 2 \end{pmatrix}$
23					$\begin{pmatrix} 2 \\ 3 \end{pmatrix}$	$\begin{pmatrix} -3 \\ -2 \end{pmatrix}$
24					$\begin{pmatrix} 3 \\ -2 \end{pmatrix}$	$\begin{pmatrix} -2 \\ 3 \end{pmatrix}$
25					$\begin{pmatrix} 1 \\ 1 \end{pmatrix}$	$\begin{pmatrix} -1 \\ -3 \end{pmatrix}$
26					$\begin{pmatrix} 3 \\ 1 \end{pmatrix}$	$\begin{pmatrix} -1 \\ -1 \end{pmatrix}$
27					$\begin{pmatrix} 1 \\ -1 \end{pmatrix}$	$\begin{pmatrix} -3 \\ 1 \end{pmatrix}$
28					$\begin{pmatrix} 1 \\ -3 \end{pmatrix}$	$\begin{pmatrix} -1 \\ 1 \end{pmatrix}$
29					$\begin{pmatrix} 1 \\ 3 \end{pmatrix}$	$\begin{pmatrix} -1 \\ -1 \end{pmatrix}$
30					$\begin{pmatrix} 1 \\ 1 \end{pmatrix}$	$\begin{pmatrix} -3 \\ -1 \end{pmatrix}$

Table 4: The 92 groups of informative 5×5 configurations (continued).

No.	Config.	Twin	Config.	Twin	a	b
31					$\begin{pmatrix} 3 \\ -1 \end{pmatrix}$	$\begin{pmatrix} -1 \\ 1 \end{pmatrix}$
32					$\begin{pmatrix} 1 \\ -1 \end{pmatrix}$	$\begin{pmatrix} -1 \\ 3 \end{pmatrix}$
33					$\begin{pmatrix} 4 \\ 3 \end{pmatrix}$	$\begin{pmatrix} -3 \\ -4 \end{pmatrix}$
34					$\begin{pmatrix} 3 \\ -4 \end{pmatrix}$	$\begin{pmatrix} -4 \\ 3 \end{pmatrix}$
35					$\begin{pmatrix} 3 \\ 4 \end{pmatrix}$	$\begin{pmatrix} -4 \\ -3 \end{pmatrix}$
36					$\begin{pmatrix} 4 \\ -3 \end{pmatrix}$	$\begin{pmatrix} -3 \\ 4 \end{pmatrix}$
37					$\begin{pmatrix} 1 \\ 2 \end{pmatrix}$	$\begin{pmatrix} 0 \\ -1 \end{pmatrix}$
38					$\begin{pmatrix} 1 \\ 0 \end{pmatrix}$	$\begin{pmatrix} -2 \\ -1 \end{pmatrix}$
39					$\begin{pmatrix} 2 \\ -1 \end{pmatrix}$	$\begin{pmatrix} -1 \\ 0 \end{pmatrix}$
40					$\begin{pmatrix} 0 \\ -1 \end{pmatrix}$	$\begin{pmatrix} -1 \\ 2 \end{pmatrix}$
41					$\begin{pmatrix} 0 \\ 1 \end{pmatrix}$	$\begin{pmatrix} -1 \\ -2 \end{pmatrix}$

20

Table 4: The 92 groups of informative 5×5 configurations (continued).

No.	Config.	Twin	Config.	Twin	a	b
42					$\begin{pmatrix} 2 \\ 1 \end{pmatrix}$	$\begin{pmatrix} -1 \\ 0 \end{pmatrix}$
43					$\begin{pmatrix} 1 \\ 0 \end{pmatrix}$	$\begin{pmatrix} -2 \\ 1 \end{pmatrix}$
44					$\begin{pmatrix} 1 \\ -2 \end{pmatrix}$	$\begin{pmatrix} 0 \\ 1 \end{pmatrix}$
45					$\begin{pmatrix} 2 \\ 3 \end{pmatrix}$	$\begin{pmatrix} -1 \\ -3 \end{pmatrix}$
46					$\begin{pmatrix} 1 \\ 3 \end{pmatrix}$	$\begin{pmatrix} -2 \\ -3 \end{pmatrix}$
47					$\begin{pmatrix} 3 \\ 1 \end{pmatrix}$	$\begin{pmatrix} -3 \\ -2 \end{pmatrix}$
48					$\begin{pmatrix} 3 \\ 2 \end{pmatrix}$	$\begin{pmatrix} -3 \\ -1 \end{pmatrix}$

Table 4: The 92 groups of informative 5 × 5 configurations (continued).

No.	Config.	Twin	Config.	Twin	a	b
49					$\begin{pmatrix} 3 \\ -2 \end{pmatrix}$	$\begin{pmatrix} -3 \\ 1 \end{pmatrix}$
50					$\begin{pmatrix} 3 \\ -1 \end{pmatrix}$	$\begin{pmatrix} -3 \\ 2 \end{pmatrix}$
51					$\begin{pmatrix} 2 \\ -3 \end{pmatrix}$	$\begin{pmatrix} -1 \\ 3 \end{pmatrix}$
52					$\begin{pmatrix} 1 \\ -3 \end{pmatrix}$	$\begin{pmatrix} -2 \\ 3 \end{pmatrix}$
53					$\begin{pmatrix} 1 \\ 2 \end{pmatrix}$	$\begin{pmatrix} -1 \\ -1 \end{pmatrix}$
54					$\begin{pmatrix} 2 \\ 1 \end{pmatrix}$	$\begin{pmatrix} -1 \\ -1 \end{pmatrix}$
55					$\begin{pmatrix} 1 \\ 1 \end{pmatrix}$	$\begin{pmatrix} -1 \\ -2 \end{pmatrix}$
56					$\begin{pmatrix} 1 \\ -1 \end{pmatrix}$	$\begin{pmatrix} -2 \\ 1 \end{pmatrix}$

22

Table 4: The 92 groups of informative 5×5 configurations (continued).

No.	Config.	Twin	Config.	Twin	a	b
57					$\begin{pmatrix} 2 \\ -1 \end{pmatrix}$	$\begin{pmatrix} -1 \\ 1 \end{pmatrix}$
58					$\begin{pmatrix} 1 \\ 1 \end{pmatrix}$	$\begin{pmatrix} -2 \\ -1 \end{pmatrix}$
59					$\begin{pmatrix} 1 \\ -2 \end{pmatrix}$	$\begin{pmatrix} -1 \\ 1 \end{pmatrix}$
60					$\begin{pmatrix} 1 \\ -1 \end{pmatrix}$	$\begin{pmatrix} -1 \\ 2 \end{pmatrix}$
61					$\begin{pmatrix} 1 \\ 3 \end{pmatrix}$	$\begin{pmatrix} 0 \\ -1 \end{pmatrix}$
62					$\begin{pmatrix} 0 \\ 1 \end{pmatrix}$	$\begin{pmatrix} -1 \\ -3 \end{pmatrix}$
63					$\begin{pmatrix} 1 \\ 0 \end{pmatrix}$	$\begin{pmatrix} -3 \\ -1 \end{pmatrix}$

23

Table 4: The 92 groups of informative 5×5 configurations (continued).

No.	Config.	Twin	Config.	Twin	a	b
64					$\begin{pmatrix} 3 \\ 1 \end{pmatrix}$	$\begin{pmatrix} -1 \\ 0 \end{pmatrix}$
65					$\begin{pmatrix} 3 \\ -1 \end{pmatrix}$	$\begin{pmatrix} -1 \\ 0 \end{pmatrix}$
66					$\begin{pmatrix} 1 \\ 0 \end{pmatrix}$	$\begin{pmatrix} -3 \\ 1 \end{pmatrix}$
67					$\begin{pmatrix} 0 \\ -1 \end{pmatrix}$	$\begin{pmatrix} -1 \\ 3 \end{pmatrix}$
68					$\begin{pmatrix} 1 \\ -3 \end{pmatrix}$	$\begin{pmatrix} 0 \\ 1 \end{pmatrix}$
69					$\begin{pmatrix} 1 \\ 4 \end{pmatrix}$	$\begin{pmatrix} -1 \\ -2 \end{pmatrix}$
70					$\begin{pmatrix} 4 \\ 1 \end{pmatrix}$	$\begin{pmatrix} -2 \\ -1 \end{pmatrix}$
71					$\begin{pmatrix} 1 \\ 2 \end{pmatrix}$	$\begin{pmatrix} -1 \\ -4 \end{pmatrix}$
72					$\begin{pmatrix} 4 \\ -1 \end{pmatrix}$	$\begin{pmatrix} -2 \\ 1 \end{pmatrix}$
73					$\begin{pmatrix} 1 \\ -2 \end{pmatrix}$	$\begin{pmatrix} -1 \\ 4 \end{pmatrix}$

24

Table 4: The 92 groups of informative 5×5 configurations (continued).

No.	Config.	Twin	Config.	Twin	a	b
74					$\begin{pmatrix} 1 \\ -4 \end{pmatrix}$	$\begin{pmatrix} -1 \\ 2 \end{pmatrix}$
75					$\begin{pmatrix} 2 \\ 1 \end{pmatrix}$	$\begin{pmatrix} -4 \\ -1 \end{pmatrix}$
76					$\begin{pmatrix} 2 \\ -1 \end{pmatrix}$	$\begin{pmatrix} -4 \\ 1 \end{pmatrix}$
77					$\begin{pmatrix} 3 \\ 4 \end{pmatrix}$	$\begin{pmatrix} -1 \\ -2 \end{pmatrix}$
78					$\begin{pmatrix} 4 \\ 3 \end{pmatrix}$	$\begin{pmatrix} -2 \\ -1 \end{pmatrix}$
79					$\begin{pmatrix} 4 \\ -3 \end{pmatrix}$	$\begin{pmatrix} -2 \\ 1 \end{pmatrix}$
80					$\begin{pmatrix} 3 \\ -4 \end{pmatrix}$	$\begin{pmatrix} -1 \\ 2 \end{pmatrix}$
81					$\begin{pmatrix} 1 \\ 2 \end{pmatrix}$	$\begin{pmatrix} -3 \\ -4 \end{pmatrix}$
82					$\begin{pmatrix} 2 \\ 1 \end{pmatrix}$	$\begin{pmatrix} -4 \\ -3 \end{pmatrix}$
83					$\begin{pmatrix} 2 \\ -1 \end{pmatrix}$	$\begin{pmatrix} -4 \\ 3 \end{pmatrix}$
84					$\begin{pmatrix} 1 \\ -2 \end{pmatrix}$	$\begin{pmatrix} -3 \\ 4 \end{pmatrix}$
85					$\begin{pmatrix} 1 \\ 1 \end{pmatrix}$	$\begin{pmatrix} -2 \\ -3 \end{pmatrix}$
86					$\begin{pmatrix} 2 \\ 3 \end{pmatrix}$	$\begin{pmatrix} -1 \\ -1 \end{pmatrix}$
87					$\begin{pmatrix} 3 \\ 2 \end{pmatrix}$	$\begin{pmatrix} -1 \\ -1 \end{pmatrix}$
88					$\begin{pmatrix} 1 \\ 1 \end{pmatrix}$	$\begin{pmatrix} -3 \\ -2 \end{pmatrix}$

Table 4: The 92 groups of informative 5×5 configurations (continued).

No.	Config.	Twin	Config.	Twin	a	b
89					$\begin{pmatrix} 1 \\ -1 \end{pmatrix}$	$\begin{pmatrix} -3 \\ 2 \end{pmatrix}$
90					$\begin{pmatrix} 3 \\ -2 \end{pmatrix}$	$\begin{pmatrix} -1 \\ 1 \end{pmatrix}$
91					$\begin{pmatrix} 2 \\ -3 \end{pmatrix}$	$\begin{pmatrix} -1 \\ 1 \end{pmatrix}$
92					$\begin{pmatrix} 1 \\ -1 \end{pmatrix}$	$\begin{pmatrix} -2 \\ 3 \end{pmatrix}$

Bibliography

Geman, S. and Geman, D. (1984): Stochastic relaxation, Gibbs distributions, and the Bayesian restoration of images. *IEEE Transactions on Pattern Analysis and Machine Intelligence* **6** 721–741.

Greig, D., Porteous, B., and Seheult, A. (1989): Exact maximum a posteriori estimation for binary images. *Journal of the Royal Statistical Society, Series B* **51** 271–279.

Grenander, U. (1981): *Lectures in Pattern Theory*, Vol. I–III. Springer, New York.

Hartvig, N.V. and Jensen, J.L. (2000a): Spatial mixture modeling of fMRI data. *Human Brain Mapping* **11** 233–248.

Jensen, E.B.V. and Kiderlen, M. (2003): Directional analysis of digitized planar sets by configuration counts. *Journal of Microscopy* **212** 158–168.

Kiderlen, M. and Jensen, E.B.V. (2003): Estimation of the directional measure of planar random sets by digitization. *Advances in Applied Probability* **35** 583–602.

Ohser, J. and Mücklich, F. (2000): *Statistical Analysis of Microstructures in Material Science*. John Wiley, Chichester.

Ohser, J., Steinbach, B., and Lang, C. (1998): Efficient texture analysis of binary images. *Journal of Microscopy* **192** 20–28.

Otsu, N. (1979): A threshold selection method from gray-level histograms. *IEEE Transactions on Systems, Man, and Cybernetics* **9** 62–66.

Schneider, R. (1993): *Convex Bodies: the Brunn-Minkowski Theory*. Cambridge University Press, Cambridge.

Schneider, R. and Weil, W. (2000): *Stochastische Geometrie*. Teubner, Stuttgart.

Serra, J. (1982): *Image Analysis and Mathematical Morphology*. Academic Press, London.

Winkler, G. (1995): *Image Analysis, Random Fields and Dynamic Monte Carlo Methods*. Springer, Berlin.

Woolrich, M.W., Behrens, T.E.J., Beckmann, C.F., and Smith, S.M. (2005): Mixture models with adaptive spatial regularization for segmentation with an application to fMRI data. *IEEE Transactions on Medical Imaging* **24** 1–11.

Paper

D

Thordis L. Thorarinsdottir and
Hans Stødkilde-Jørgensen (2006).
**Functional imaging of pelvic floor
muscle control**.
To appear as Thiele Research Report,
Department of Mathematical Sciences,
University of Aarhus.

Functional imaging of pelvic floor muscle control

Thordis L. Thorarinsdottir and Hans Stødkilde-Jørgensen
University of Aarhus

Abstract

Stress urinary incontinence (SUI) is defined as an involuntary loss of urine during exertion, or on sneezing or coughing. It is the most common form of incontinence in women and is often a consequence of weakness of the pelvic floor. Treatment of SUI includes pelvic floor muscle training, where contraction exercises are performed in order to strengthen the pelvic floor. Using functional magnetic resonance imaging (fMRI), we compared the brain activation in healthy women, in women suffering from SUI before any kind of treatment, and in women suffering from SUI after months of regular pelvic floor muscle training during repetitive pelvic floor muscle contraction. In the group of healthy women, we found activation in premotor cortex, parietal lobe, superior temporal cortex, and insula. The activation in patients with SUI before treatment was somewhat less focused, no significant activation was found in the insula while additional activation was found in primary and supplementray motor cortex, post-central gyrus, and lentiform nucleus. Statistical comparison of the activation in the two groups revealed that only the activation in lentiform nucleus is significantly different between the groups. Preliminary analysis indicates that the activation in patients with SUI decreases with regular pelvic floor muscle training and that the activation is more focused than in the group of healthy women. More data is, however, needed in order to confirm this result.

1 Introduction

Stress urinary incontinence (SUI) is the most common form of incontinence in women. It is defined as incontinence caused by coughing, laughing, sneezing, exercising or other movements that increase intra-abdominal pressure and thus increase pressure on the bladder. SUI in women is often caused by physical changes resulting from pregnancy and childbirth. The urethra is supported by fascia of the pelvic floor. If the fascia support is weakened, as can be the case

during pregnancy and childbirth, the urethra can move downwards at times of increased abdominal pressure, resulting in stress incontinence. The most commonly recommended physical therapy treatment for women who suffer from SUI are contraction exercises of the pelvic floor muscle, see Freemann (2004). This may also be combined with electrical stimulation or biofeedback.

Several reports concerning brain activation and different aspects of micturition control have been published in the last decade. In a PET study on adult healthy females, Blok *et al.* (1997) investigated brain activation during repetitive pelvic floor contraction, sustained pelvic floor contraction, and sustained abdominal straining. The authors found activation in the superomedial precentral gyrus, the most medial portion of the motor cortex, during repetitive pelvic floor straining. Additional activity was also found in the cerebellum, supplementary motor cortex, and thalamus. In a more recent work, Zhang *et al.* (2005) used fMRI to investigate brain activation during repeated pelvic floor muscle contraction in healthy males during empty-bladder condition and full-bladder condition. By subtracting the brain activation during the two conditions, the authors were interested in observing the brain activity during voluntary control of voiding. They reported activation mainly in the medial premotor cortex, basal ganglia, and cerebellum. Seseke *et al.* (2006) used functional imaging to measure the brain activation induced by relaxing or contracting the pelvic floor muscle in an event-related manner in healthy adult women with full bladder. Relaxation and contraction of pelvic floor muscles induced strong and similar activations patterns including frontal cortex, sensory motor cortex, cerebellum and basal ganglia.

Changes in the brain activation due to pelvic floor muscle training in women suffering from SUI has been investigated by Di Gangi Herms *et al.* (2006). The authors investigated the neuroplastic changes induced by 12 weeks of pelvic floor muscle training with EMG-biofeedback using functional imaging. After the training, a more focused brain activation during repetitive pelvic floor muscle contraction exercises was reported. Reduction in activation was found in the supplementary motor area, insula, anterior singular cortex, superior medial frontal gyrus, middle frontal gyrus, and putamen. Further, a statistical evaluation of the number of activated voxels between pre- and post-measurements revealed fewer activated voxels after the training period.

The aim of this study is to investigate the brain activation during repetitive activation of the pelvic floor muscle, both in healthy adult women and in women suffering from SUI. There are two different aspects to be investigated here. Firstly, it is of interest to compare the brain activation in healthy adult women and in stress incontinent women before physical therapy or other form of treatment. The hypothesis here is that it it easier for the healthy women to perform the repetitive contraction of the pelvic floor muscle than for the women suffering from SUI. The second aim of the study is to compare

the brain activation during repetitive pelvic floor contraction before and after physical therapy treatment for women suffering from SUI. During the physical therapy treatment, the women perform regular pelvic floor muscle training under professional supervision which should enable them to develop a routine for performing this kind of exercises. It is, however, not known how these differences between the groups affect the brain activation.

2 Materials and methods

2.1 Subjects

Thirteen female subjects (mean age 53 years $\pm$ 9 (SD), range 32-65 years) with a history of SUI were included in the study. None of the subjects had undergone pelvic surgery, was taking any form for medication for incontinence or other bowel or bladder problems, or gone through physiotherapy for incontinence. All subjects were without history of neurological or psychiatric illness, were right handed, and were included in the study after written informed consent.

Each subject participated in a fMRI recording as she entered the study. She then enrolled in a physical therapy treatment that lasted five to six months. During the treatment, the subjects performed regular pelvic floor muscle training under the supervision of a professional physical therapist. At the end of the physical therapy treatment, the subjects participated in another fMRI recording. We will in the following refer to this group of subjects as group one.

Further, eleven female health care professionals (mean age 36 years $\pm$ 7 (SD), range 27-51 years) with no history of urological symptoms or prolapse participated in the study. All subjects were without history of neurological or psychiatric illness, were right handed, and were included in the study after written informed consent. In the following, we refer to this group of subjects as group two.

2.2 FMRI

All participants were given precise instructions regarding the experimental procedure prior to the fMRI recording. All individuals were asked to void before entering the scanner. Subjects were explicitly asked to concentrate on pelvic floor contraction and not to move other body parts.

Each session consisted of three task periods, each lasting 30 seconds, with 30 seconds of rest after each task period. During task periods, the subjects were asked to contract the pelvic floor muscles repeatedly in a rhythmic manner for one and a half second with one and a half second of rest between the

contractions. The subjects were informed of the switch between a task period and a resting period with a tap on the leg. After the fMRI recording, the subjects were asked whether they had had problems performing the task. All subjects reported that there had been no difficulties in performing the task. The data was preliminary analysed during the acquisition using the built-in software of the scanner. Sessions showing movement artifacts unrelated to the pelvic floor muscle were excluded from the later analysis. After this exclusion procedure, the whole dataset consisted of one to three sessions of data from each subject from each fMRI recording. From group one, there are thirteen fMRI recordings made before physical therapy treatment with two repetitions in each recording. Seven of the subjects have also been scanned after the treatment, giving five recording with two repetitions in each, one recording with three repetitions, and one recording with one repetition only. Of the data from subjects in group two, there are seven fMRI recordings with two repetitions, one recording with three repetitions, and three recordings with one repetition.

The MR images were acquired at 1.5 T (GE Sigma Twin Gradient, Aarhus, Denmark) using quadrature field head coil. Initially, an anatomical T1-weighted MRI dataset covering the whole brain was acquired (min. full, TR = 750ms, FOV = 24×24cm, NEX = 1.5, size of acquisition matrix = 256×192 voxels). 21 to 32 slices of 3mm thickness with 1mm gap between the slices were acquired. Functional imaging was performed using a T2*-sensitive gradient echo EPI technique (nr. shots = 1, TE = 50.2ms, TR = 3000ms, FOV = 24×24cm, flip angle = 90°, size of acquisition matrix = 64×64 voxels). As before, 21 to 32 slices of 3mm thickness with 1mm gap between the slices, covering the whole brain, were acquired.

2.3 Data analysis

All data pre-processing and data analysis were performed using SPM5 (available at http://www.fil.ion.ucl.ac.uk/spm/software/spm5/). Before spatial preprocessing, the data was converted from DICOM format to NIFTI format.

The results from the statistical analysis are shown either using glass brain views or mapped on the canonical T1-weighted single-subject anatomical image that is provided with SPM5. In order to obtain the anatomical locations of activity, the MNI space coordinates given by SPM5 are mapped to Talairach space coordinates using the algorithm by Brett (2002). The Talairach Daemon Client, see Lancaster *et al.* (2000), was then used to associate the Talairach coordinates of the peaks of activation to the nearest grey matter location in the brain.

Spatial pre-processing

The data was motion-corrected by realigning the time series of images using a 6 parameter (rigid body) spatial transformation. The images were subsequently resliced and unwarped with respect to out-of-plane rotations (i.e. pitch and roll). The data was normalised to MNI space using the EPI template provided with SPM5. In the final step of the spatial pre-processing, the normalised data was smoothed with a Gaussian kernel with full width at half maximum equal to 8 mm. The scans from one subject from group one were discarded at this stage. This subject had only been scanned before treatment.

Analysis of individual activation

The data from those subjects in group one where we have both pre- and post-measurements was analysed on individual basis. Here, we used two repetitions from each of the two fMRI recordings from five subjects (data from one subject was discarded as it showed high artifact-related activity and data from another subject was discarded as it contained only one repetition from the second fMRI recording). Each session was modelled separately with a general linear model using the canonical haemodynamic response function as a basis function. The data was further filtered with a high-pass filter with cutoff at 128 seconds and serial correlations in the time series were accounted for using an autoregressive AR(1) model. Inference was performed using a one-sided t-test with null hypothesis of no activation during task periods and an alternative hypothesis of higher activation during task periods than during rest. The statistical threshold was set at $p = 0.05$ and multiple comparison correction was done using family-wise error correction, see Nichols and Hayasaka (2003) The same analysis was performed on two repetitions of data from each of eight subjects from group two.

Group comparison using random effects analysis

The data from group two was compared to the pre-measurements from group one using random effects analysis. The post-measurements from group one were not included in this comparison due to insufficient amount of data in that category. With data from only seven subjects, the outcome of a random effects analysis will presumably be inaccurate. The data for each group was analysed with a general linear model where the activity in each session was modelled using the canonical haemodynamic response function with its temporal and dispersion derivatives. The time derivative allows the peak response to vary by plus minus a second and the dispersion derivative allows the width of the response to vary by a similar amount. Filtering and correction for serial correlations was performed as before. Statistical parametric maps were

computed for each subject using one-sided t-tests with null hypothesis of no accumulated effect of the basis function in question over all sessions from that subject and an alternative hypothesis of positive effect of the same basis function over all sessions from that subject. The contrast images from these tests were then entered in a second level analysis. The second level analysis was a one-way ANOVA analysis with one factor consisting of three levels (the three basis functions) where the different levels of the factor were assumed to be correlated. Here, we performed an one-sided t-test with null hypothesis of no effects of the haemodynamic response function and an alternative hypothesis of positive effect of the same function. The statistical threshold was set at $p = 0.05$ and family-wise error correction used.

Further, the data from the two groups was compared using a two-way ANOVA model for the statistical parametric maps from each subject. This model had two factors, one with two independent levels describing the groups of subjects and another with three correlated levels describing the three basis functions. The tests of interest under this model are the t-tests for different effects of the haemodynamic response function on the two groups. That is, the t-test for equal effects with an alternative hypothesis of more effect in group one and the t-test for equal effects with an alternative hypothesis of more effect in group two. Both tests were performed with the statistical threshold set at $p = 0.05$ and family-wise error correction, as well as with the statistical threshold at set $p = 0.001$ and no multiple comparison correction.

Group comparison using conjunction analysis

In a third step in the statistical analysis, conjunction analysis was performed on each of the three categories of data: pre-measurements from subjects in group one, post-measurements from subjects in group one, and measurements from subjects in group two. From group one, we have five subjects with two sessions of data from each measurements. We have thus, for similarity, only used five of the eight datasets from group two. These were chosen at random. The ten sessions from each category were analysed together in one general linear model with the canonical haemodynamic response function to model the activation. Further, filtering and modelling of serial correlations were performed as described above. Inference was then performed using a minimum statistic test for conjunction analysis, see Friston *et al.* (1999). This test compares the minimum t-statistic to the null distribution of a minimum t-statistic. The null hypothesis here is that there is no activation in any of the sessions during on-periods. The alternative hypothesis is thus that there is activation in at least one of the sessions during on-periods. As before, the statistical threshold was set at $p = 0.05$ and multiple comparison correction was done using family-wise error correction.

3 Results

3.1 Individual activation

The individual brain activation during repetitive pelvic floor contraction for the healthy subjects is shown in Figure 1. Figure 2 shows the type of activation revealed in both pre- and post-measurements for five subjects suffering from SUI. We see that the activation in the data is very heterogeneous between subjects while rather similar between repetitions within the same fMRI recording.
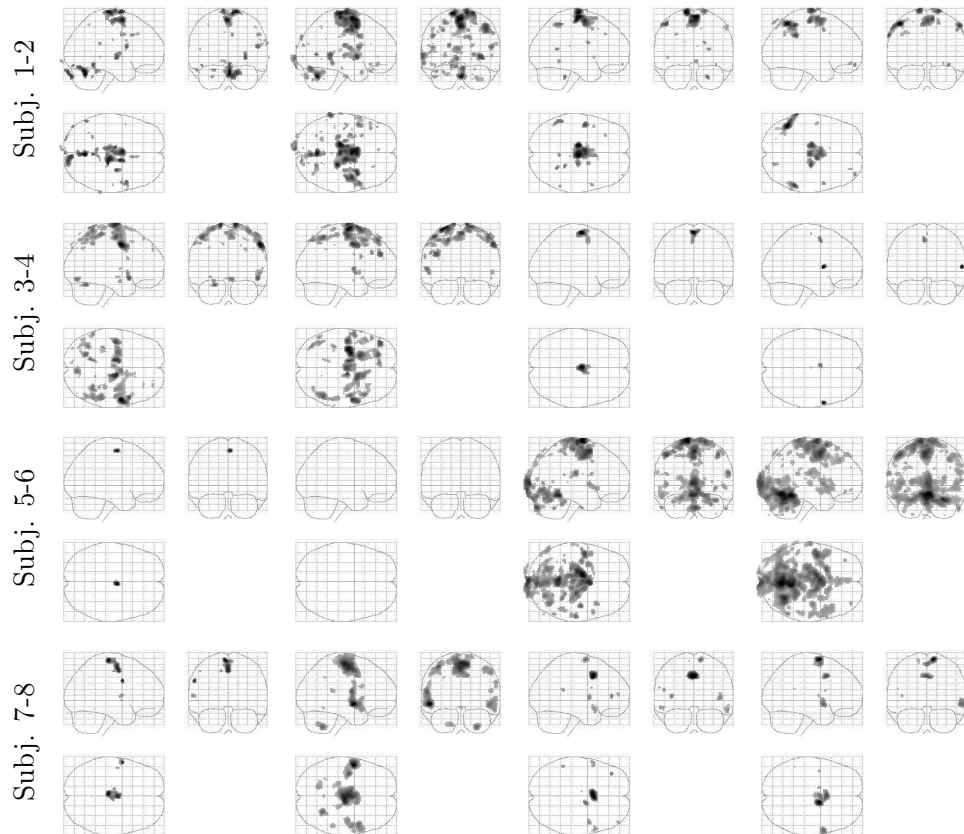

Figure 1: Glass brain views showing the individual results for the eight subjects from group two. The glass brains show significant activation during task periods compared to baseline with statistical threshold $p = 0.05$ and family-wise error correction. From left to right and top to bottom: results for session one for subject one, session two for subject one, session one for subject two, session two for subject two and so on.
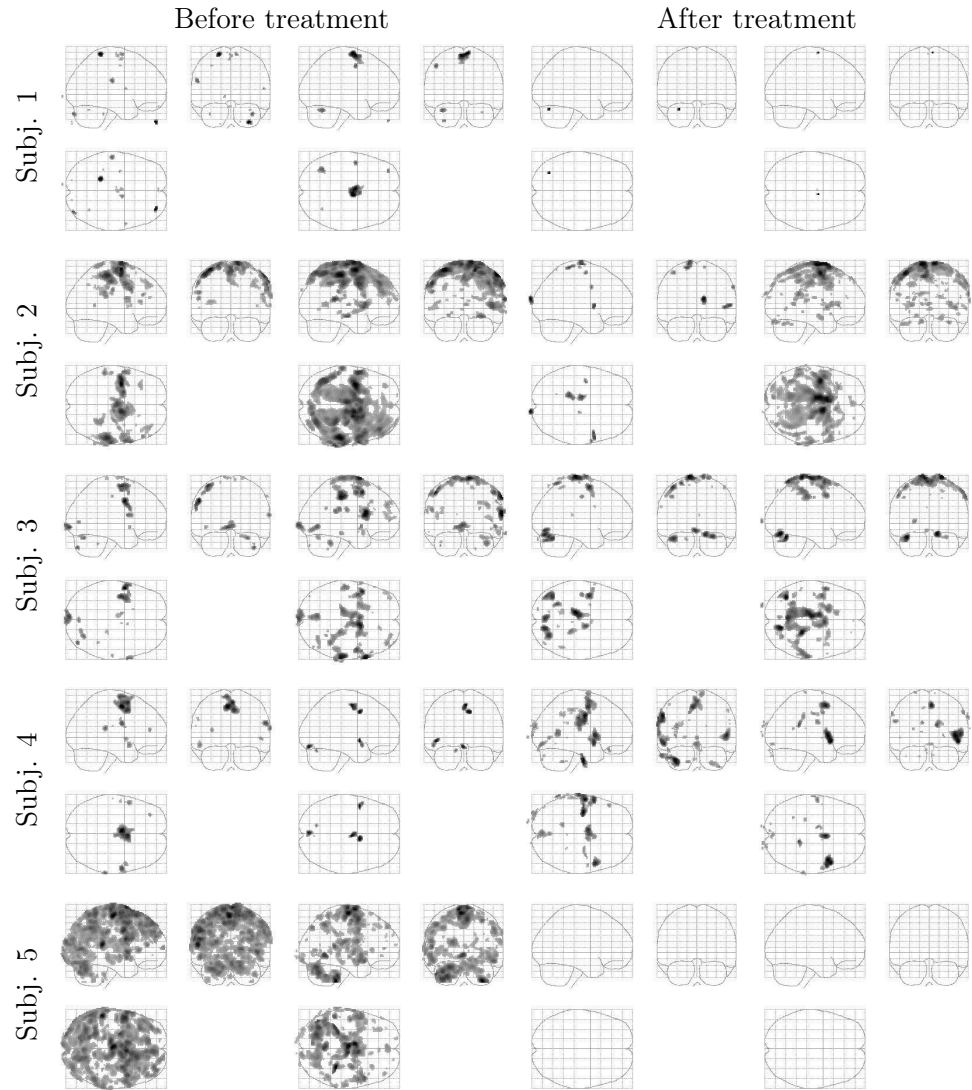
Figure 2: Glass brain views showing the individual results for subjects from group one. The glass brains show significant activation in on-periods compared to baseline with statistical threshold $p = 0.05$ and family-wise error correction. From top to bottom: results for subject one to subject five. From left to right: results for session one before treatment, session two before treatment, session one after treatment, and session two after treatment for each subject.

The dispersion of the numbers of activated voxels in the whole brain for each of the three categories of data is embodied in Figure 3. The mean number of activated voxels for pre-measurements in group one is 5585 voxels, the mean

number of activated voxels for post-measurements in group one is 1313 voxels, and the mean number of activated voxels in data from group two is 2706 voxels.
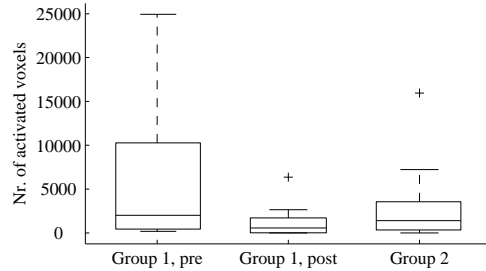

Figure 3: The dispersion of the number of activated voxels in the whole brain in the images shown in Figure 2 and Figure 1. Each box has lines at the lower quartile, the median, and the upper quartile values. Outliers are denoted with a plus (+). Left: Results for the 10 pre-measurements from group one. Middle: Results for the 10 post-measurements from group one. Right: Results for the 16 measurements from group two.

3.2   Random effects analysis

Random effects analysis of the data from subjects suffering from SUI reveals task-related activation in the motor areas, the precentral gyrus, and the parietal lobe in both left and right cerebrum. Further activation is also detected in the right temporal lobe, as well as in the left and right lentiform nucleus. For healthy subjects, same type of an analysis reveals significant task-related activation in left motor areas, left precentral gyrus, right parietal lobe, and the right insula. Glass brain views of the task-related activation for the two groups is shown in Figure 4, while Figure 5 shows the activation projected on coronal slices of a T1-weighted anatomical image. These images indicate some difference in the activation between the two groups. Further statistical comparison reveals, however, that most of the difference in the activation is not statistically significant. This is demonstrated in Figure 6. Testing for difference in the activation between the two groups at statistical threshold of $p = 0.05$ and using family-wise error correction reveals no voxels with significant difference. We have therefore used uncorrected p-values with threshold at $p = 0.001$ in the images shown in Figure 6. At this level, group two shows significantly higher activation in the right lentiform nucleus than group one. No voxels showing higher activation in group one than in group two were detected. The Talairach coordinates, anatomical location, Brodmann area labelling, T values, and cluster size of the activation for the two groups is given in Table 1.
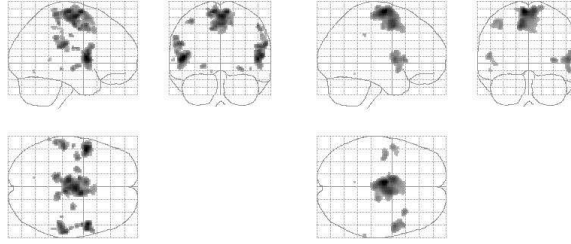
Figure 4: Glass brain views showing activation during task periods in the group data from the random effect analysis. The statistical threshold was set at $p = 0.05$ and family-wise error correction was used. Left: positive effects of the haemodynamic response function in pre-measurements from group one. Right: positive effects of the haemodynamic response function in measurements from group two.

Table 1: Anatomical location of activation in pre-measurements of subjects in group one and measurements of subjects in group two as shown in Figure 4. Only clusters of size larger than four voxels are shown. Location of the peak of activation is indicated in millimetres in coordinates x, y, and z in Talairach space. The Brodmann area labelling of the anatomical locations is given in parenthesis.

| Brain lobe	Anatomical location	Talairach coord.	T value	Cluster size
Pre-measurements in group one				
right frontal lobe	middle frontal gyrus (BA6)	2 -7 57	8.46	1646
left frontal lobe	middle frontal gyrus (BA6)	-38 -8 56	7.09	45
right frontal lobe	precentral gyrus (BA6)	50 0 46	7.24	45
right frontal lobe	precentral gyrus (BA4)	55 -16 36	6.50	7
left frontal lobe	precentral gyrus (BA44)	-48 4 7	8.85	386
right parietal lobe	postcentral gyrus (BA43)	51 -7 19	6.72	11
left parietal lobe	postcentral gyrus (BA43)	-53 -13 19	6.55	9
right parietal lobe	inferior parietal lobule (BA40)	59 -22 25	7.77	180
left parietal lobe	inferior parietal lobule (BA40)	-51 -24 25	7.61	187
right temporal lobe	superior temporal gyrus (BA22)	50 6 5	8.48	281
right sub-lobar	lentiform nucleus, globus pallidus	26 -14 -4	6.79	26
left sub-lobar	lentiform nucleus, globus pallidus	-24 -8 -3	6.69	31
Measurements in group two				
left frontal lobe	superior frontal gyrus (BA6)	-6 -6 65	9.46	2005
left frontal lobe	precentral gyrus (BA6)	-42 -5 52	6.83	103
left frontal lobe	precentral gyrus (BA44)	-51 2 9	6.97	73
right parietal lobe	inferior parietal lobule (BA40)	63 -33 37	6.25	5
right temporal lobe	superior temporal gyrus (BA22)	51 4 5	7.72	294
right sub-lobar	insula	34 16 3	7.16	34
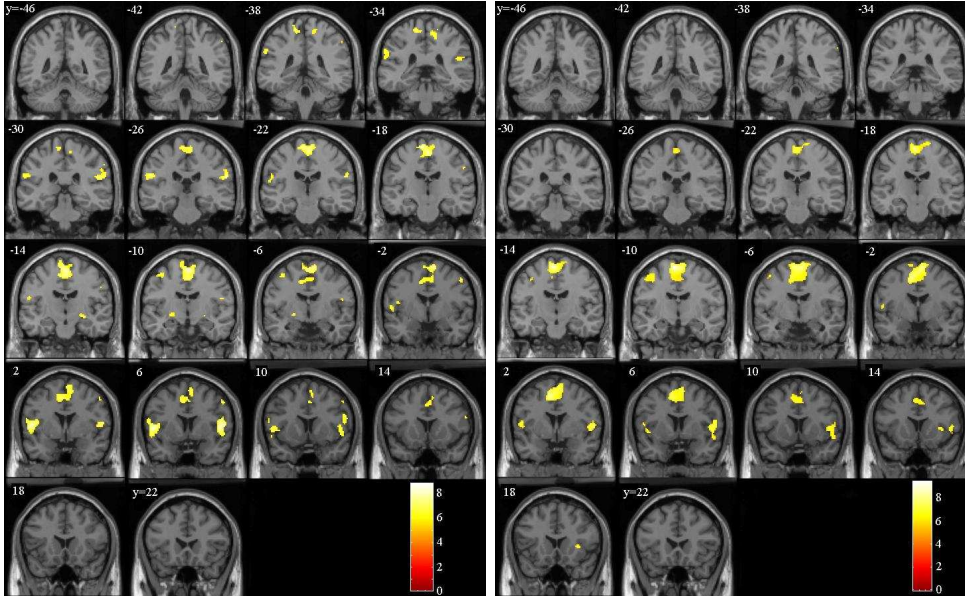
Figure 5: Positive effect of the haemodynamic response function during task periods as revealed by random effects analysis in pre-measurements in group one (left) and in group two (right). Activations are projected on coronal sections through the brain from posterior to anterior, starting at $y = -46$mm and ending at $y = 22$mm in MNI space, with increment of 4mm between sections. The image used is the canonical Tl-weighted single-subject anatomical image provided with SPM5. The activations shown are those with statistical threshold $p < 0.05$ under family-wise error correction. The T-value of the activity is given in the adjacent colour scale.
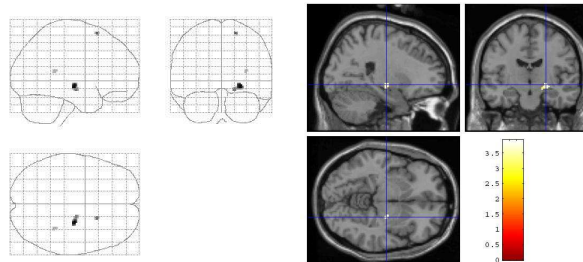

Figure 6: Areas that are more active during task periods in pre-measurements from group one than during task periods in measurements from group two. Left: Glass brain view showing the results for statistical threshold at $p = 0.001$ without multiple comparison correction. Right: The same result mapped on the canonical T1-weighted single-subject anatomical image provided with SPM5. The blue cursor indicates the location of the global maximum. It is located at $(24, -14, -4)$ in Talairach coordinates which is in the right lentiform nucleus. The cluster size is 15 voxels.

11

3.3   Conjunction analysis

The group results from the conjunction analysis are shown in Figure 7. As for the random effects analysis, the activation is similar for group one before treatment and for group two, with slightly less activation in the healthy control subjects. The results for the post-measurements in group one show, on the other hand, much less activation than in the two other categories. Here, we obtain significant activation in the left superior frontal gyrus, the right superior temporal gyrus, the left inferior parietal lobe, the left fusiform gyrus, and the claustrum. The Talairach coordinates of the peaks of activation, anatomical locations, Brodmann area labelling, T values, and cluster size of the activation is given in Table 2. Comparing the results in Table 2 to the results in Table 1, we see that there is activation at the first three locations mentioned above, Brodmann areas 6, 22, and 40, for all categories of data. The random effects analysis, however, does not reveal activation in the left fusiform gyrus, Brodmann area 19, or the left claustrum. Further analysis of the activation shown in Figure 7 (not stated explicitly here) though reveals that, under conjunction analysis, all three categories of data show significant activation in the left claustrum and significant activation in the left fusiform gyrus can also be found in the data from group two.
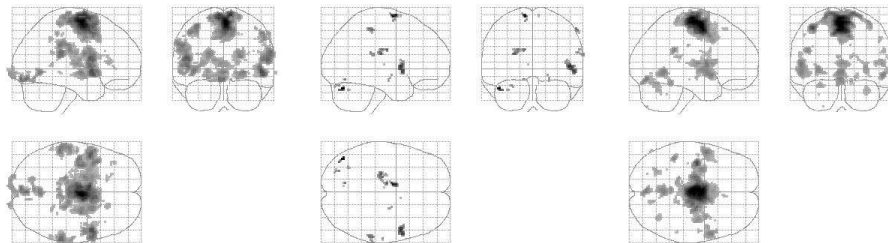

Figure 7: Glass brain views showing areas where there is significant activation in at least one session from one subject during on-periods as given by conjunction analysis. We have set the statistical threshold to $p = 0.05$ and used family-wise error correction. Left: Activation in pre-measurements from five subjects from group one. Middle: Activation in post-measurements from five subjects from group one. Right: Activation in data from five subjects from group two. The five subjects were chosen at random from the group of eight subjects and their individual activations are the ten first images shown in Figure 1.

Conjunction analysis reveals activation that is present in at least one subject from the group by comparing the minimum t-statistic to a null distribution of minimum t-statistics. An additional session with very low activation will thus influence the total result much more than an additional session with high activation. An inspection of the individual results shown in Figure 2 shows that

Table 2: Activation sites during post-measurements of subjects in group two as revealed by conjunction analysis with statistical threshold set at $p = 0.05$ and family wise error correction. Only clusters of size larger than four voxels are shown. Location of the peak of activation is indicated in millimetres in coordinates x, y, and z in Talairach space. The Brodmann area labelling of the anatomical locations is given in parenthesis.

Brain lobe	Anatomical location	Talairach coord.	T value	Cluster size
left frontal lobe	superior frontal gyrus (BA6)	-10 -1 65	1.31	19
right parietal lobe	inferior parietal lobule (BA40)	59 -29 49	1.00	17
right temporal lobe	superior temporal gyrus (BA22)	50 6 3	1.22	75
left occipital lobe	fusiform gyrus (BA19)	-44 -71 -18	1.39	8
left sub-lobar	claustrum	-24 -18 19	1.10	45

there is very low activation in few of the sessions, in fact there are no significant voxels at all in two of the sessions for the threshold used. It is therefore not surprising that we, for incontinent women after treatment, obtain only fragments of the amount of activation obtained in the scans before training. As an example of this feature of the conjunction analysis, we have repeated the test shown in Figure 7, now without Subject 5 from Figure 2. Among the five subjects, this subject shows the highest activation before physical therapy treatment and the lowest activation after the treatment. The results are shown in Figure 8. We see that the activation image for the post-measurements now shows much higher activation than the corresponding image in Figure 7 while the difference between the pre-measurement activation images is not that substantial.
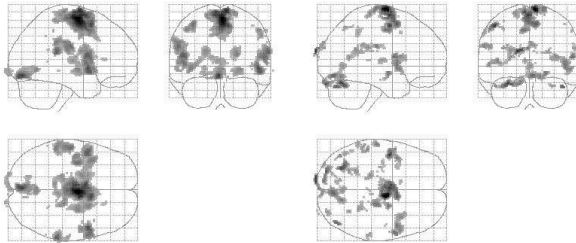

Figure 8: Glass brain views showing areas with positive activation during on-periods in at least one session from one subject as given by conjunction analysis. The statistical threshold is set at $p = 0.05$ and family-wise error correction is used. Left: Activation in pre-measurements from four subjects from group one. Right: Activation in post-measurements from four subjects from group one. The subject discarded in this test is Subject 5 in Figure 2.

13

4 Discussion

The aim of this study is two-fold. Firstly, we are interested in comparing the brain activation during repetitive pelvic floor contraction in women suffering from stress urinary incontinence and in healthy adult women. The second factor of interest are possible changes in the brain activity during repetitive pelvic floor contraction induced by several months of intense physical therapy treatment for women suffering from stress urinary incontinence.

4.1 Effects of physical therapy treatment

We have used conjunction analysis to investigate the effects of physical therapy treatment, as we lack more data from women suffering from SUI that have finished the physical therapy treatment in order to be able to perform random effects analysis. Figure 7 and Figure 8 show that the activation during repetitive pelvic floor contraction seems to become more focused for women suffering from SUI after months of regular training with contraction exercises. An inspection of the results shown in Figure 2 also reveals that, for each subject, the activation after treatment is usually lower than before treatment. From the data that we have available, there are thus strong indications that the brain activation during repetitive pelvic floor contraction in stress incontinent women decreases with regular training of the pelvic floor muscle, which gives the women certain routine in performing the exercises. This is coherent with the results in Di Gangi Herms *et al.* (2006) where the authors report more focused activation during pelvic floor muscle contraction with EMG-biofeedback in women suffering from SUI after 12 weeks of training. There is further indication that the activation for stress incontinent women after regular training is more focused than the activation for healthy women during task periods, cf. Figure 7 (right) vs. Figure 7 (middle) and Figure 8 (right). One should, however, be careful in concluding that the difference is as severe as indicated by the results in Figure 7. It is here important to extend the study by including more subjects so that we can get sound results for this part of the analysis.

4.2 Effects of SUI

Concerning the other aim of the study, we see in Figure 5 that women with stress incontinence show more widespread brain activation during repetitive pelvic floor contraction than healthy women. This difference reveals itself in that while women with stress incontinence usually have mirrored activation in right and left cerebrum, healthy women often show significant activation in only one of the two. This is, for instance, the case for the frontal gyrus,

the precentral gyrus, and the inferior parietal lobe. Further, women with stress incontinence have activations in the postcentral gyrus and the lentiform nucleus, not present in the data from healthy women. The healthy women, on the other hand, show significant activation in the right insula. Under statistical comparison, however, only the difference in activation in the lentifrom nucleus is significant. This suggests that one can not tell from brain imaging alone whether a subject suffers from SUI.

4.3 Activated areas

We will now discuss in more detail each of the areas reported in Table 2. The results from the conjunction analysis will not be discussed in detail, as an extended analysis is planned when more data will be available. When we refer to results from group one in the following, we thus mean the results obtained from scans acquired before physical therapy treatment.

Motor areas

The primary motor cortex, Brodmann area 4, is located along the precentral gyrus in the frontal lobe. It is important for the generation of neural impulses that control the exertion of movement. The secondary motor areas include the premotor cortices and the supplementary motor area, which together form Brodmann area 6. The latter is regarded as the main motor planning area which is involved in complex movements while the premotor cortices are important for the sensory guidance of movements (Seseke *et al.* 2006). Blok *et al.* (1997) reported activation in the primary motor cortex during repetitive pelvic floor contraction in healthy women when compared with rest while Zhang *et al.* (2005) found activation in supplementary motor area in their investigation of voluntary voiding control in men but no activation in the primary motor cortex. Seseke *et al.* (2006), on the other hand, observed activation in both primary motor cortex and supplementary motor area during relaxation and contraction of the pelvic floor muscle in healthy women with full bladder. The activation in primary motor cortex was stronger during contraction while activation in the supplementary motor area was stronger during relaxation. In their investigation of SUI, Di Gangi Herms *et al.* (2006) found activation in all three motor areas in measurements of pelvic floor contraction before treatment but only in the primary motor cortex after 12 weeks of training. Our results are similar, in that we found activation in all three areas for group one. For healthy subjects, our results are similar to the results in Zhang *et al.* (2005) as we found activation in premotor and supplementary motor cortex during repetitive pelvic floor contraction but no significant activation in primary motor cortex.

Frontal areas

The frontal lobes are considered to be emotional control centre. They are involved in motor function, problem solving, spontaneity, memory, language, initiation, judgement, impulse control, and social and sexual behaviour (Seseke *et al.* 2006). The activation reported in connection with micturition in the frontal areas of the brain is quite heterogeneous. Blok *et al.* (1997) reported activation in right superior and medial frontal cortex, Brodmann area 8 and 9, during repetitive pelvic floor straining minus rest in healthy women. Seseke *et al.* (2006) found higher activity during contraction than during relaxation bilaterally in the inferior frontal gyrus for healthy women with full bladder. Further, Di Gangi Herms *et al.* (2006) observed activation in the middle frontal gyrus, Brodmann area 46, when subtracting activation after training from activation observed before training in women with SUI. We observed activation in the right precentral gyrus, Brodmann area 44, for both groups of subjects.

Parietal areas

The parietal lobe plays a role in integrating sensory information and takes part in visuo-motor integration. Seseke *et al.* (2006) observed activation in the inferior parietal lobe which they suspect might be related to the visual commands in their paradigm rather than micturition process itself. Others have though also reported parietal activation in micturition related experiments, Athwal *et al.* (2001) found bilateral activation in parietal cortex during bladder filling while in Zhang *et al.* (2005), the right side seems more dominant. Our results include bilateral activation in the parietal lobe for women with SUI and activation in the right parietal lobe for healthy women. Note that the subjects in our experiment were notified of the switch between task periods and rest with a tap on the leg, so that no visual commands are used.

Temporal lobe

The temporal lobe is usually put in connection with high-level auditory processing including speech. We observed activation in the right superior temporal gyrus during task periods for both group one and group two. Similar results are reported in Blok *et al.* (1997) and Di Gangi Herms *et al.* (2006). These results include though only the data acquired after training in Di Gangi Herms *et al.* (2006).

Basal ganglia

The basal ganglia are a group of nuclei usually involved with regulation of cortically initiated motor activity. There is further evidence that these areas

might also play a role in cognition and emotion processes, see Seseke *et al.* (2006). We found significant bilateral activation in the globus pallidus is pre-measurements from group two. Nour *et al.* (2000) also found activation in the same area during micturition in men. Several publications have reported related activation in the putamen, another part of the basal ganglia. Zhang *et al.* (2005) found bilateral activation during pelvic floor muscle contraction in full bladder but not in empty bladder condition when scanning male subjects and Seseke *et al.* (2006) confirmed these findings with reports of activation in putamen both during relaxation and contraction of the pelvic floor muscle in healthy women with full bladder. Furthermore, Di Gangi Herms *et al.* (2006) reported activation in the putamen when subtracting pre-measurements from post-measurements in their investigation of pelvic floor muscle training with biofeedback in women with SUI.

Insula

The insula is a part of the para-limbic system and is involved in viscero-motor control and in viscero-sensory functions (Kavia *et al.* 2005). We observed activation in the right insula during repetitive pelvic floor contraction compared to rest for healthy women only. In Seseke *et al.* (2006), activation in the insula is reported for relaxation of the pelvic floor with full bladder. Further, Di Gangi Herms *et al.* (2006) found activation in the right insula for both pre- and post-measurements. Activation in the insula can be related to activation in the temporal lobe, Brodmann area 22, as discussed in Di Gangi Herms *et al.* (2006).

Acknowledgements

Bibliography

Athwal, B.S, Berkley, K.J., Hussain, I., Brennan, A., Craggs, M., Sakakibara, R., Frackowiak, R.S., Fowler, C.J. (2001): Brain responses to changes in bladder volume and urge to void in healthy men. *Brain* **124** 369-377.

Bharat, R., Kavia, C., Dasgupta, R., and Fowler, C.J. (2005): Functional imaging and the central control of the bladder. *The Journal of Comparative Neurology* **493** 27-32.

Blok, B.F.M., Sturms, L.M., and Holstege, G. (1997): A PET study on cortical and subcortical control of pelvic floor musculature in women. *The Journal of Comparative Neurology* **389** 535-544.

Brett, M. (2002): The MNI brain and the Talairach atlas. *http://www.mrc-cbu.cam.ac.uk/Imaging/Common/mnispace.shtml*

Di Gangi Herms, A.M.R., Veit, R., Reisenauer, C., Herms, A., Grodd, W., Enck, P., Stenzl, A., and Birbaumer, N. (2006): Functional imaging of stress urinary incontinence. *NeuroImage* **29** 267-275.

Freemann, R.M. (2004): The role of pelvic floor muscle training in urinary incontinence. *BJOG: an International Journal of Obstetrics and Gynaecology* **111** 37-40.

Friston, K., Holmes, A., Price, C., Büchel, C., and Worsley, K. (1999): Multi-subject fMRI studies and conjunction analysis. *NeuroImage* **10** 385-396.

Kavia, R.B.C., Dasgupta, R., and Fowler, C.J. (2005): Functional imaging and the central control of the bladder. *The Journal of Comparative Neurology* **493** 27-32.

Lancaster, J.L., Woldorff, M.G., Parson, L.M., Liotti, M., Freitas, C.S., Rainey, L., Kochunov, P.V., Nickerson, D., Mikiten, S.A., and Fox, P.T. (2000): Automated Talairach Atlas labels for functional brain mapping. *Human Brain Mapping* **10** 120-131.

Nichols, T. and Hayasaka, S. (2003): Controlling the familywise error rate in functional neuroimaging: a comparative review. *Statistical Methods in Medical Research* **12** 419-446.

Nour, S., Svarer, C., Kristensen, J., Paulsen, O., and Law, I. (2000): Cerebral activation during micturition in normal men. *Brain* **123** 781-789.

Seseke, S., Baudewig, J., Kallenberg, K, Ringert, R.-H., Seseke, F., and Dechent, P. (2006): Voluntary pelvic floor muscle control - An fMRI study. *NeuroImage In Press*

18

Zhang, H., Reitz, A., Kollias, S., Summers, P., Curt, A., and Schurch, B. (2005): An fMRI study of the role of suprapontine brain structures in the voluntary voiding control induced by pelvic floor contraction. *NeuroImage* **24** 174-180.